

# Graphene quantum dots for biological applications

Ananthanarayanan, Arundithi

2016

Ananthanarayanan, A. (2016). Graphene quantum dots for biological applications. Doctoral thesis, Nanyang Technological University, Singapore.

<https://hdl.handle.net/10356/69428>

<https://doi.org/10.32657/10356/69428>

# **GRAPHENE QUANTUM DOTS FOR BIOLOGICAL APPLICATIONS**

**Arundithi Ananthanarayanan**

School of Chemical and Biomedical Engineering

A thesis submitted to the Nanyang Technological University

in partial fulfilment of the requirement for the degree of

Doctor of Philosophy

**2016**

## **Acknowledgements**

In this section, I would like to take the opportunity to express my gratitude and appreciation to the people without which this dissertation would not have been possible.

First and foremost, I would like to thank my supervisor Professor Chen Peng for giving me the opportunity to pursue my PhD study under his tutelage. His constant encouragement, guidance and support have made this journey an invaluable experience. I am greatly indebted to him for giving the independence to choose my projects and execute them with constant support.

The members of Prof. Chen Peng's group who have been instrumental in various aspects of my research. I would like to thank Dr. Zheng Xinting, Dr. Parimal Routh, Ms. Priyanka Prasad, Dr. Mahasin Alam, Dr. Wang Xuewan, Dr. Than Aung, Ms. Shu Jing, Dr. Wang Yue, Dr. Chen Yun and many other people who have offered their wonderful advice and support over the last 4 years.

I would like to thank all my collaborators for their support and help in various aspects of my project: Dr. Wang Yue and Prof. Sun Handong from School of Physical and Mathematical Sciences, NTU. Asst. Prof. Xu Chenjie and Dr. Liu Yi from School of Chemical and Biomedical Engineering, NTU.

To my friends, who have been constant pillar of strength and support throughout this journey.

Finally, I would like to thank my family for their constant encouragement, guidance and love.

# Table of Contents

|  |    |
|--|----|
| Chapter 1 Background and Specific Aims .....   | 1  |
| 1.1 Background .....   | 1  |
| 1.2 Aims and Outline .....   | 3  |
| Chapter 2 Literature Review .....  | 6  |
| 2.1 Properties .....   | 6  |
| 2.1.1 <i>Structure</i> .....   | 6  |
| 2.1.2 <i>Optical properties</i> .....  | 7  |
| 2.2 Synthetic Methods .....  | 12 |
| 2.3 Changing PL properties by chemical modification .....  | 17 |
| 2.3.1 <i>Heteroatom doping</i> .....   | 17 |
| 2.3.2 <i>Controlling Surface Oxidation</i> .....   | 19 |
| 2.3.3 <i>Polymer Passivation</i> .....   | 20 |
| 2.3.4 <i>Surface Modification with Small Molecules</i> .....   | 20 |
| 2.4 Biological Applications .....  | 21 |
| 2.4.1 <i>Cellular Imaging</i> .....  | 21 |
| 2.4.2 <i>Real-time cell tracking</i> .....   | 23 |
| 2.4.3 <i>In-vivo imaging</i> .....   | 24 |
| 2.4.4 <i>Biosensing</i> .....  | 25 |
| 2.4.5 <i>Drug delivery</i> .....   | 31 |
| 2.4.6 <i>Anticancer Agents</i> .....   | 33 |
| 2.4.7 <i>Antibacterial activity</i> .....  | 35 |
| Chapter 3 Facile Synthesis of Graphene Quantum Dots from 3D graphene<br>for Fe <sup>3+</sup> Ion Sensing ..... | 37 |
| 3.1 Materials and Methods .....  | 38 |
| 3.1.1 <i>Materials</i> .....   | 38 |
| 3.1.2 <i>3D graphene synthesis</i> .....   | 38 |
| 3.1.3 <i>GQD Synthesis</i> .....   | 38 |
| 3.2 Results and Discussion .....   | 40 |
| 3.2.1 <i>Synthesis mechanism</i> .....   | 40 |
| 3.2.2 <i>Chemical characterization</i> .....   | 42 |
| 3.2.3 <i>Morphological Characterization</i> .....  | 43 |
| 3.2.4 <i>Optical Characterization</i> .....  | 44 |
| 3.2.5 <i>Optical detection of ferric ions</i> .....  | 45 |

|   |    |
|---|----|
| 3.2.6 <i>Properties of Fe<sup>3+</sup> induced aggregates</i> .....   | 47 |
| 3.3 Conclusions .....   | 49 |
| Chapter 4 Nitrogen and Phosphorus co-doped Graphene Quantum Dots:<br>Synthesis from Adenosine triphosphate, Optical Properties, and Cellular<br>Imaging ..... | 51 |
| 4.1 Materials and Methods.....  | 52 |
| 4.1.1 <i>Synthesis of ATP-GQDs</i> .....  | 52 |
| 4.1.3 <i>Transferrin conjugation</i> .....  | 53 |
| 4.1.4 <i>Characterizations</i> .....  | 53 |
| 4.1.5 <i>Cell Imaging</i> .....   | 54 |
| 4.2 Results and Discussion .....  | 54 |
| 4.2.1 <i>Properties of carbonized ATP</i> .....   | 54 |
| 4.2.2 <i>Morphological characterization of GQDs</i> .....   | 56 |
| 4.2.3 <i>Chemical characterization of GQDs</i> .....  | 57 |
| 4.2.4 <i>Optical characterization of GQDs</i> .....   | 59 |
| 4.2.6 <i>PL lifetime and photostability of GQDs</i> .....   | 62 |
| 4.2.7 <i>Transferrin conjugated GQDs for in-vitro cell imaging</i> .....  | 63 |
| 4.3 Conclusions .....   | 65 |
| Chapter 5 Graphene Quantum Dots as Robust Carriers for Hydrophobic<br>Drugs.....  | 67 |
| 5.1 Materials and Methods.....  | 68 |
| 5.1.1 <i>Synthesis of GQDs</i> .....  | 68 |
| 5.1.2 <i>Drug Loading</i> .....   | 68 |
| 5.1.3 <i>Drug Release</i> .....   | 69 |
| 5.1.4 <i>Cell culture and cytotoxicity assay</i> .....  | 69 |
| 5.1.5 <i>Characterizations</i> .....  | 70 |
| 5.2 Results and Discussion .....  | 70 |
| 5.2.1 <i>Morphological Characterization</i> .....   | 70 |
| 5.2.2 <i>Optical Characterization</i> .....   | 71 |
| 5.2.3 <i>Chemical Characterization</i> .....  | 73 |
| 5.2.4 <i>Drug Loading and Release</i> .....   | 74 |
| 5.3 Conclusion.....   | 76 |
| Chapter 6 Factors Influencing GQD Fluorescence: A Theoretical Study .....   | 78 |
| 6.1 Computational Methods.....  | 79 |
| 6.2 Results and Discussion .....  | 79 |
| 6.2.1 <i>Effect of size</i> .....   | 79 |

|   |    |
|---|----|
| 6.2.2 <i>Effect of edge configuration</i> .....                 | 81 |
| 6.2.3 <i>Effect of oxygenated functional groups</i> .....       | 82 |
| 6.2.4 <i>Effect of vacancy defects</i> .....                    | 83 |
| 6.2.5 <i>Effect of hybridization state in larger GQDs</i> ..... | 83 |
| 6.3 Conclusion.....   | 88 |
| Chapter 7 Conclusions and Future Perspectives .....             | 89 |
| 7.1 Conclusions .....   | 89 |
| 7.2 Future Directions.....                                      | 90 |
| Appendix I- List of Publications .....                          | 92 |
| Appendix II- List of Figures .....                              | 93 |
| References .....  | 97 |

## Summary

Graphene quantum dots (GQDs) have emerged as a new class of fluorescent materials that show clear advantages over their currently existing counterparts. Their unique properties of small size, biocompatibility, photostability and large surface area make them suitable candidates for a plethora of applications. Currently the field of graphene quantum dots is in nascent stages and is filled with challenges and opportunities. This thesis attempts to contribute to the growing field of graphene quantum dots by developing new synthesis strategies and by conducting systematic studies to understand the mechanism involved in GQD fluorescence for fundamental sensing and biological applications.

Firstly, we demonstrate a novel, versatile and high throughput synthesis approach for blue-luminescent GQDs from 3D freestanding graphene. The use of 3D graphene electrode is suitable for lowering reaction time and producing high quality GQDs. The simultaneous functionalization of GQDs during synthesis renders them sensitive to ferric ions in solution. The as-synthesized GQDs are used as fluorescence turn-off sensor for ferric ions with a lower theoretical detection limit of 7.22  $\mu\text{M}$ .

Secondly, heteroatom doping in graphene and GQDs has known to introduce new and enhanced properties. In this regard, we demonstrate a two-step synthesis protocol for nitrogen and phosphorous co-doped GQDs. The GQDs show a high quantum yield of 28% and a high two-photon absorption cross-section of 20000 GM. To further explore the possibility of these GQDs as bioimaging agents, we have conjugated transferrin, an iron binding protein for targeted uptake by cancer cells in-vitro. We observe that GQDs can be used as robust fluorophores for cell labeling and also tracking single exocytotic and endocytotic events in cells.

Thirdly, we demonstrate a new mechanical synthesis strategy for the production of GQDs using ball-milling and use the as prepared GQDs as drug carriers. We have explored the use of GQDs as drug delivery vehicle for the highly hydrophobic drug  $\beta$ -lapachone. The

GQD-drug conjugates exhibit a pH dependent release behavior. They also exhibit enhanced cytotoxicity as compared to free drug in two different cancer cell lines in-vitro. Lastly, we identified that the poor understanding of photoluminescence mechanisms hinders the widespread use of GQDs. In this regard, we have carried out systematic theoretical investigations on the various factors influencing GQD fluorescence with the use of density-functional theory (DFT) and time-dependent DFT calculations. Our findings indicate that fluorescence of a GQD is greatly influenced by its size, edge configuration, shape and attached chemical functionalities. In addition, it is also observed that fluorescence properties of large GQDs consisting of heterogeneously hybridized carbon network is dependant largely on small  $sp^2$  clusters isolated by  $sp^3$  carbons.



# Chapter 1 Background and Specific Aims

## 1.1 Background

Fluorescence, particularly photoluminescence is a physical phenomenon in which a molecule/ material absorbs photons of shorter wavelength and emits photons of longer wavelength. Materials that possess this property are commonly known as fluorophores. Fluorophores have been an integral part of research for many decades as they find application in bioimaging, sensing, immunofluorescence, protein studies, and dye sensitized solar cells etc.

Currently, the commonly used fluorophores are fluorescent dyes, fluorescent proteins and inorganic semiconductor quantum dots. Fluorescent dyes and proteins mainly find widespread applications as fundamental tools in biochemistry, cell biology and fluorescent sensing. However they suffer from many drawbacks that limit their applications. For instance, fluorescent dyes undergo bleaching of fluorescence upon repeated light excitation. They also have a narrow excitation wavelength range, making them difficult to use for long term imaging experiments. Fluorescent proteins are genetically expressed along with the protein of interest. They are mostly confined to in-vitro fluorescent imaging/ sensing applications and require tedious procedures for synthesis and purifications.

The quest to overcome the inherent disadvantages of fluorescent proteins and dyes led to the development and use of semiconductor quantum dots. Inorganic compounds such as sulfides and selenides of groups II-VI or III-V elements in the periodic table are commonly explored as quantum dots. With a particle size smaller than the bohr's radius, they exhibit quantum confinement effects resulting in the distinct optical and electronic properties.

Although traditionally explored for applications in microelectronics and optoelectronics, the past years have seen a rapid rise in the use of semiconductor quantum dots (QDs) in

biological, biomedical and sensing applications. The key developments that have allowed these applications are the advances in the synthesis of highly luminescent QDs with high yields, complex surface chemistry, water solubility, biocompatibility and multicolour emission. The applications have also expanded to molecular and cellular imaging, nanoparticle drugs conjugates for targeted therapy, disease screening, detection and diagnosis.<sup>1</sup>

QDs show distinct advantages over fluorescent dyes and proteins. They are highly resistant to photo bleaching, have a range of excitation wavelength, tunable emission (change in QD size changes emission wavelength) and can be tailored to be hydrophobic/hydrophilic. However, as they became increasingly used in biological applications, several concerns were recognized.

Firstly, QDs were usually composed of elements such as cadmium, which pose environment concerns and biocompatibility issues. Secondly, most QDs are bulky in nature with a surface passivation layer or with a core-shell structure. This leads to steric effects upon protein conjugation and makes them impractical for use in cell studies. Thirdly, the surface defects in QDs cause “blinking” wherein there is an intermittent loss of fluorescence signal. This makes them less preferable for long duration and live cell imaging experiments.

The need to develop alternate fluorophores that can supersede fluorescent dyes and QDs has made researchers search for alternate fluorophores that can circumvent their disadvantages. Ideally a fluorophore should be bright, small sized, photostable and should have ease of chemical modification/bioconjugation.

A relatively easy solution focused towards the development of alternative materials that are semiconducting in nature and possess the conjugated/carbonaceous framework of fluorescent dyes. This can be achieved from materials such as conjugated polymers, amorphous carbon and graphene.

Graphene, a single atom thick 2-dimensional array of  $sp^2$  hybridized carbon atoms has been an important material of interest. The absence of a band gap in graphene is the most notable property, making graphene a zero-band gap semiconductor or a semi metal, enabling its use in numerous electronic devices.<sup>2</sup>

Pristine graphene is often limited in applications due to zero band gap, aggregation and poor dispersion in common solvents. Modifying the dimensions and chemistry of graphene by functionalization has become a common practice for tuning the band gap of graphene.

Recently, zero-dimensional form of water dispersible graphene known as graphene quantum dots (GQDs) has been reported.<sup>3</sup> GQDs show interesting optical and electronic properties due to quantum confinement and are receiving much attention in the fields of sensing, bioimaging, energy and photocatalysis.<sup>4-6</sup> Furthermore, the organic framework, high photostability, and non-toxic nature of GQDs make them suitable alternatives for conventional fluorescent materials.

Currently the field of GQDs is still at early stages and is filled with abundant opportunities. This thesis aims to contribute to the growing field of GQDs by developing various synthesis strategies for GQDs that find application in sensing, biology and biomedicine and by studying the mechanisms of fluorescence in detail.

## **1.2 Aims and Outline**

On account of the immense promise offered by GQDs to emerge as new class of environment friendly and biocompatible fluorophores, the design and synthesis of GQDs **are** of utmost importance to derive their full application potential. There has been ongoing research to harvest the potential of GQDs but it is riddled with challenges. Keeping in mind the current challenges GQD research this thesis is aimed at developing new synthesis strategies for GQD synthesis and their application in fields such as

fluorescent sensing, bio-imaging and drug delivery. The thesis also focuses extensively on the study of fluorescent properties of GQDs.

The specific objectives of this dissertation are:

1. To develop various low cost, high throughput and rapid synthesis strategies for GQDs using various precursor materials. Synthesis strategies will be developed to yield high quality GQDs for specific applications.
2. Synthesis of GQDs towards applications in fluorescent sensing. Simultaneous functionalization of GQDs with heteroatoms during synthesis will be conducted to render specificity towards analytes such as metal ions.
3. Improving the fluorescence properties of GQDs. Several strategies for improving fluorescence quantum yield (QY) and tuning emission wavelength of GQDs will be investigated. The GQDs will also be surface modified with functional groups for conjugation to biomolecules for targeted imaging.
4. Explore the use of GQDs as drug carriers. The extensive  $\pi$  conjugated structure of GQDs offers a platform for loading drugs with  $\pi$ -conjugated structures. GQDs will be investigated as drug carriers for hydrophobic drugs using simple  $\pi$ - $\pi$  stacking and the loading and release behavior will be studied.
5. To investigate the elusive mechanisms behind GQD fluorescence. Theoretical studies will be conducted on various GQD models to understand mechanism of fluorescence.

Chapter 1 of this thesis highlights the current need for alternate fluorophores in biology/ biomedicine. The reason behind the exploration of GQDs as alternate fluorophores is established. Chapter 2 summarizes the current developments in the field of GQDs. The properties of GQDs along with various synthesis strategies and applications in biology and environment are discussed in detail. In Chapter 3 a new synthesis strategy for high yield production of GQDs for application in fluorescent sensing of metal ions is

discussed. It includes synthesis and characterization results for GQDs and development of fluorescence turn-off based sensing platform for ferric ions in solution. Chapter 4 aims to improve and modify GQD fluorescence properties for use as fluorescent probes in cell labeling. It discusses a new strategy for co-doping GQDs with nitrogen and phosphorous using a single precursor molecule. The influence of doping on fluorescence properties is investigated and a proof-of-concept demonstration of GQDs for cell-labelling is conducted.

Chapter 5 explores the application of GQD as drug carriers for hydrophobic drugs. GQDs are assessed for loading and release of the, drug  $\beta$ -lapachone at various pH and optimized for drug loading and release. The anticancer efficacy of the GQD-drug conjugates on various cell lines are studied. In Chapter 6, a detailed theoretical investigation of factors affecting GQD fluorescence is presented. The chapter discusses the influence of edge, size, surface functionalization and hybridization on GQD fluorescence.

Chapter 7 summarizes the conclusions of the various other chapters that contributed to this thesis. It also provides an outlook on the future on GQDs including improvement in synthesis techniques, applications in biomedicine as well as other novel applications.

## Chapter 2 Literature Review

Graphene quantum dots are typically few atom thick nanometer sized graphene sheets with a size typically less than 30nm in diameter. They are usually decorated with oxygen functionalities at the edges, which make them hydrophobic in nature. Their small size, organic framework and crystal structure makes GQDs suitable for applications in variety of fields such as sensing, bioimaging, energy and photo catalysis.<sup>4-7</sup>

The properties, synthesis procedures and applications of GQDs will be discussed in the following sections.

### 2.1 Properties

#### 2.1.1 Structure

GQDs, resemble the crystalline structure of single to a-few layered graphene GQDs are typically a few nanometers although the largest size reported is ~60 nm.<sup>8</sup> The shape of most synthesized GQDs is circular or elliptical (Figure 2.1), although triangular, quadrate and hexagonal GQDs have also been reported.<sup>9</sup>

The crystalline structure of GQDs has been investigated by HRTEM imaging and X-ray diffraction. From HR-TEM measurements, a graphitic in-plane lattice spacing of 0.18 – 0.24 nm (corresponding to different diffraction planes) is widely reported.<sup>10</sup> From XRD measurement, a graphitic inter-layer spacing of 0.334 nm or higher has been revealed. Depending on the synthetic routes, various defects, heteroatoms, and functional groups are introduced, which, may significantly alter the structural and physicochemical properties.

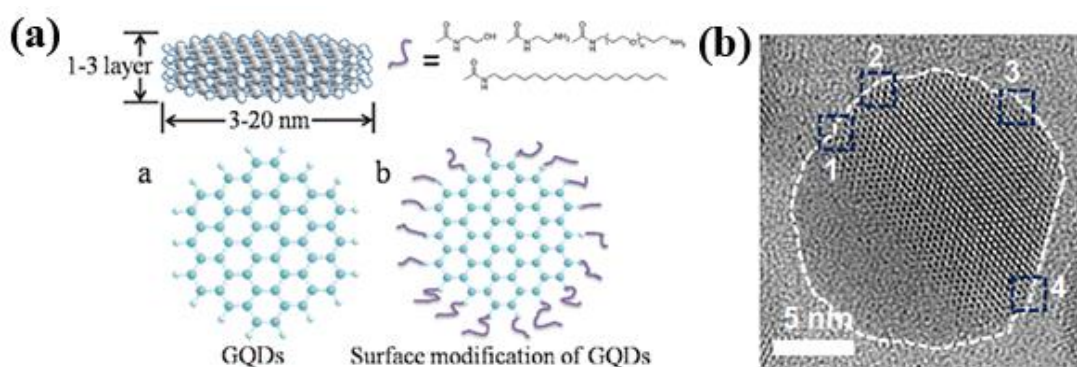


**Figure 2.1** Structural depiction of (a) GQDs. Adapted with permission.<sup>7</sup> Copyright 2010, Wiley-VCH.

HRTEM images of (b) GQDs showing combination of zigzag and armchair edges Reprinted with permission<sup>11</sup>, copyright 2012, American Chemical Society.

### 2.1.2 Optical properties

**Absorption:** GQDs usually show a prominent absorption peak at about 230 nm, and a long tail extending into the visible range (Figure 2.2a).<sup>10</sup> The strong UV absorption is attributed to the  $\pi$ - $\pi^*$  transitions of the C=C bonds present in the graphene lattice of GQDs. Functional groups may alter the absorption features.

**Photoluminescence (PL):** The PL properties of GQDs are the key to many applications. Most GQDs show fluorescence in the blue to yellow region of the visible spectrum with a unique characteristic of excitation dependent emission. The emission wavelength of GQDs is red shifted upon increasing the excitation wavelength (Figure 2.2b). The PL of GQDs is highly photostable and non-blinking, making them advantageous over inorganic QDs. GQDs prepared solvothermally from graphene oxide show insignificant photobleaching under illumination of low power UV lamp or mercury lamp. Decrease in PL intensity is only observed when 1000W high pressure mercury lamp is used.<sup>12</sup> Under confocal laser illumination, the GQD fluorescence intensity remains strong (53% remaining) after 18 min, whereas the FITC fluorescence is completely quenched after only 2 min under the same irradiation.<sup>13</sup>

The mechanisms underlying the tunable PL properties of GQDs are not completely understood, largely because of the inconsistent experimental observations caused by the large heterogeneity of individual particles from the same synthesis as well as distinct and not precisely defined properties of GQDs obtained from different processes. For example, the supposed size-dependent emission of GQDs (i.e., smaller diameter GQDs shall emit shorter wavelength due to bandgap opening by quantum confinement) has not been unambiguously demonstrated by experiments.<sup>11</sup> Experimental determination relies on controllable synthesis of well-defined GQDs, which is currently lacking.

*Upconversion Luminescence:* Non-linear emission has been reported in many kinds of GQDs. Liu *et al.* reported strong two-photon induced fluorescence from N-doped GQDs.<sup>14</sup> The two-photon absorption cross-section reaches 48000 GM, which is two orders of magnitude larger than that of conventional organic dyes and is comparable to semi-QDs (Figure 2.2c). The 800 nm excitation used for this N-doped GQD can achieve a large tissue penetration depth of 1800  $\mu\text{m}$ , promising for *in vivo* imaging. Up-conversion PL has been observed from some GQDs and is attributed to multi-photon active process.<sup>15, 16</sup> However, Shen *et al.* suggested that the multi-photon process is insufficient to explain the up-conversion of GQDs, because of the existence of a constant energy difference between the emission and excitation corresponding to the energy difference between the  $\pi$  and  $\sigma$  orbitals.<sup>17</sup> Using an energy level structural model, an anti-stokes transition mechanism is proposed. Briefly, a low energy photon excites  $\pi$  electron (at intermediate energy level) to LUMO, whereby subsequent relaxation into  $\sigma$  orbital (HOMO) results in the emission of a shorter wavelength photon.

Wen *et al.* recently argued that the observed multi-photon excitation properties in some GQDs may be artificial and could originate from the normal fluorescence excited by the



leaking component from the second diffraction in the monochromator of the fluorescence spectrophotometer.<sup>18</sup>

*Electrochemiluminescence (ECL):* ECL behaviors of GQDs have only been identified recently. Li *et al.* were the first to report that green luminescent GQDs (2-7 nm, single layered or bi-layered) showed an ECL emission 9 times higher than background signal at -1.45 V with K<sub>2</sub>S<sub>2</sub>O<sub>8</sub> as coreactant.<sup>19</sup> The onset potential was found to be -0.9 V. Lu *et al.* synthesized blue-luminescent single-layer GQDs (~ 4 nm), which showed a strong ECL at -1.52V using K<sub>2</sub>S<sub>2</sub>O<sub>8</sub> as coreactant. The signal was about 19.2 times more than the background signal.<sup>20</sup> The ECL signal was very stable with a relative standard deviation of 1.63%, upon continuous cyclic scanning for 10 minutes. In contrast, the onset potential for the GQDs hydrothermally synthesized from GO is as low as 0.4 V.<sup>21</sup> It is assumed that GQDs exhibit stable ECL properties with an onset potential closer the 0V possibly due to the accelerated electron transport by high content of sp<sup>2</sup> carbon. The mechanism of ECL for GQDs have been speculated to be oxido-reductive where during potential cycling, the reduced state of GQD (R<sup>·-</sup>) or a co-reactant species such as K<sub>2</sub>S<sub>2</sub>O<sub>8</sub> (S<sub>2</sub>O<sub>8</sub><sup>·2-</sup>) is formed at negative potentials and oxidized state of GQDs (R<sup>·+</sup>) is formed at positive potentials (Figure 2.2d).<sup>21, 22</sup> Electron transfer annihilation between the reduced and oxidized species results in the formation of an excited state (R\*) which, in turn, produces an ECL signal upon relaxation to ground state.

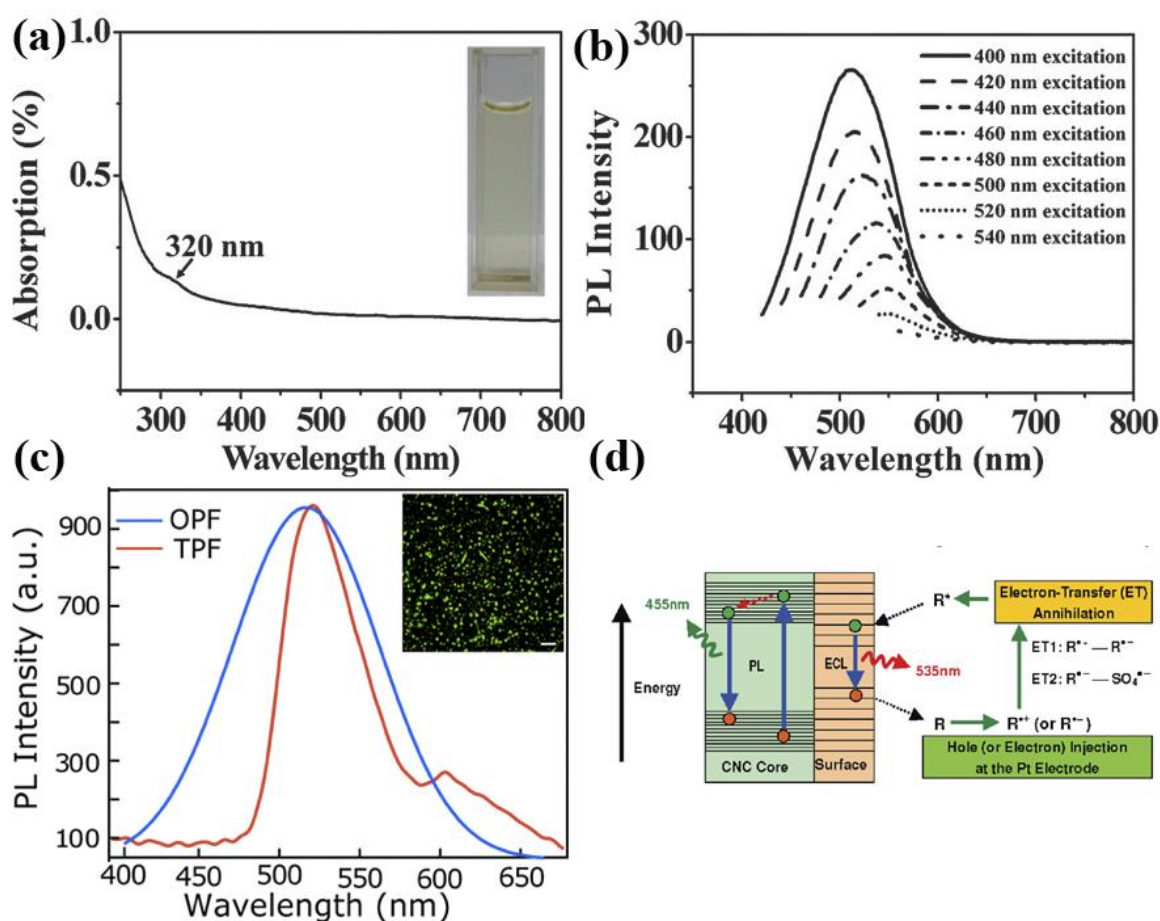


**Figure 2.2** (a) UV-vis absorption (ABS) spectra of the GQDs aqueous solution. (b) The excitation-dependent PL behavior of GQDs, when the GQDs were excited at wavelengths from 400 to 540 nm. Adapted with permission.<sup>12</sup> Copyright 2011, The Royal Society of Chemistry. (c) Two-photon-induced fluorescence spectrum of N-GQDs under 800 nm femtosecond laser excitation. Inset: Two-photon fluorescence image of dry N-GQDs (scale bar: 10  $\mu\text{m}$ ) Reproduced with permission.<sup>14</sup> Copyright 2013, American Chemical Society. (d) Schematic illustration of the ECL and PL mechanisms in GQDs.  $\text{R}^{\bullet+}$ ,  $\text{R}^{\bullet-}$ , and  $\text{R}^*$  represent negatively charged, positively charged, and excited-state GQDs, respectively. Reproduced with permission.<sup>22</sup> Copyright 2009, American Chemical Society.

### 2.1.3 Electrochemical properties

The electrochemical characteristics of GQDs are a complex interplay between carbon core, functional groups, and doped heteroatoms.<sup>23</sup> Efficient electron transfer of GQDs is benefited from its large specific surface area and abundant edge sites. Due to the small size of GQDs, single-electron can be trapped in the quantum well formed between a GQD

and surface coating.<sup>24</sup> Most GQDs have oxygenated functional groups that give them catalytic activity similar to graphene oxide (GO).<sup>25, 26</sup> Heteroatom doping (mainly N-doping) can also endow GQDs with catalytic properties towards oxygen reduction.<sup>27, 28</sup>

#### **2.1.4 Biocompatibility**

GQDs being carbonaceous materials are expected to be environmentally and biologically safe. However, a comprehensive investigation should be performed to evaluate their *in-vitro* and *in-vivo* toxicities before using them in biomedical applications. Till date, the toxicity studies conducted by various groups suggest low toxicity for GQDs.

*In-vitro* cytotoxicity of GQDs with human breast cancer cell lines T47D and MDA-MB-231 have been evaluated by Peng *et al.* The MTT assay result indicates GQDs of doses up to 50  $\mu\text{g mL}^{-1}$  does not pose significant toxicity to both cell lines.<sup>29</sup> Similarly, the cellular activity of MG-63 (human osteosarcoma) cells were not significantly affected upon the addition of 400  $\mu\text{g}$  GQDs. Besides cancer cell lines, GQDs toxicity have been evaluated in stem cells by Zhang *et al.*<sup>30</sup> Shang *et al.* carried out a more detailed investigation of the effects of GQDs on hNSCs. The results indicated that no significant change in the viability, proliferation, metabolic activity, self-renewal ability and differentiation potential of hNSCs after treatment with GQDs.<sup>31</sup>

*In-vivo* toxicology and long term biodistribution of PEG-functionalized GQDs have been studied in mice.<sup>32</sup> These GQDs did not cause appreciable toxicity to the mice at a dose of 20  $\text{mg kg}^{-1}$  over three months. The PEG-functionalized GQDs mostly accumulate in the liver and spleen and could be gradually cleared. All these evidence so far show GQDs have great potential for *in-vitro* and *in-vivo* biomedical applications, although more toxicity studies such as median lethal dose (LD50) measurements are further required.

## 2.2 Synthetic Methods

Synthesis of GQDs can follow two approaches namely, "top-down" and "bottom-up" methods.<sup>6, 7, 10</sup> The former involves cleaving or breaking down of large carbonaceous precursors *via* physical, chemical or electrochemical techniques. The latter is realized by pyrolysis or carbonization of small organic molecules or by step-wise chemical fusion of small aromatic molecules.

### 2.2.1 Top-down Approaches

*Acidic oxidation:* Strong acid treatment have been widely used to exfoliate GQDs from carbon fibers,<sup>29</sup> graphene oxide (GO),<sup>33</sup> coal,<sup>34</sup> and carbon black.<sup>35</sup> Generally a combination of strong oxidizing acids such as HNO<sub>3</sub> and H<sub>2</sub>SO<sub>4</sub> are usually used along with elevated temperatures to cleave precursors. Such methods are amenable for large-scale solution-processable production from readily available low-cost carbon sources (Figure 2.3a). Such methods unavoidably introduce negatively charged oxygenated groups onto the resultant GQDs, making them hydrophilic and defective in graphitic structure.

*Hydrothermal or solvothermal synthesis:* The hydrothermal synthesis of GQDs usually begins with the thermal reduction of graphene oxide, where the temperature in this step plays an important role in determining the structure of obtained GQDs.<sup>33</sup> The reduced graphene sheets were then oxidized using strong oxidants including concentrated inorganic acids like HNO<sub>3</sub> or H<sub>2</sub>SO<sub>4</sub>,<sup>12, 29, 33, 35-39</sup> hydrogen peroxide and ozone.<sup>40</sup> During this oxidation process, epoxy groups are introduced in a line along a carbon lattice, which would create defects by interrupting the C-C bonds (Figure 2.3b). In the final deoxidation step, which is usually achieved in alkaline medium under hydrothermal conditions,<sup>33, 36</sup>

these defect sites will facilitate the breaking up of the graphene sheets into smaller fragments, and GQDs are obtained.

Zhu *et al.* reported the first solvothermal synthesis of green luminescent GQDs with GO as starting material.<sup>12</sup> GO was first dissolved in DMF and sonicated for 30 min, and the mixture was heated for 5 h at 200 °C to obtain GQDs with average diameter of 5.3 nm and average height of 1.2 nm. These GQDs were soluble in both water and organic solvents and achieved a QY of 11.4%.

*Electrochemical exfoliation:* Electrochemical exfoliation of GQDs is usually conducted by applying potential to electrodes made of graphene precursors. The most commonly used electrode for electrochemical exfoliation is a graphite rod. Lu *et al.* (6-8 V, 240 min)<sup>41</sup> and Zhang *et al.*<sup>30</sup> reported the exfoliation of graphite rod in aqueous solutions with suitable electrolytes. The governing mechanism of this synthesis strategy is that, the OH<sup>•</sup> and O<sup>•</sup> radicals formed in the electrolyte from anodic oxidation of water plays the role of electrochemical "scissors" in its oxidative cleavage reaction, which will oxidize the carbon anode, causing the release of the C-GQDs (Figure 2.3c).<sup>42</sup>

Green luminescent GQDs have also been synthesized electrochemically in 0.1M phosphate buffer solution (PBS) with a graphene film as working electrode.<sup>43</sup> The GQDs were prepared in cyclic voltammetry mode within  $\pm 3.0$  V at a scan rate of 0.5 Vs<sup>-1</sup>.

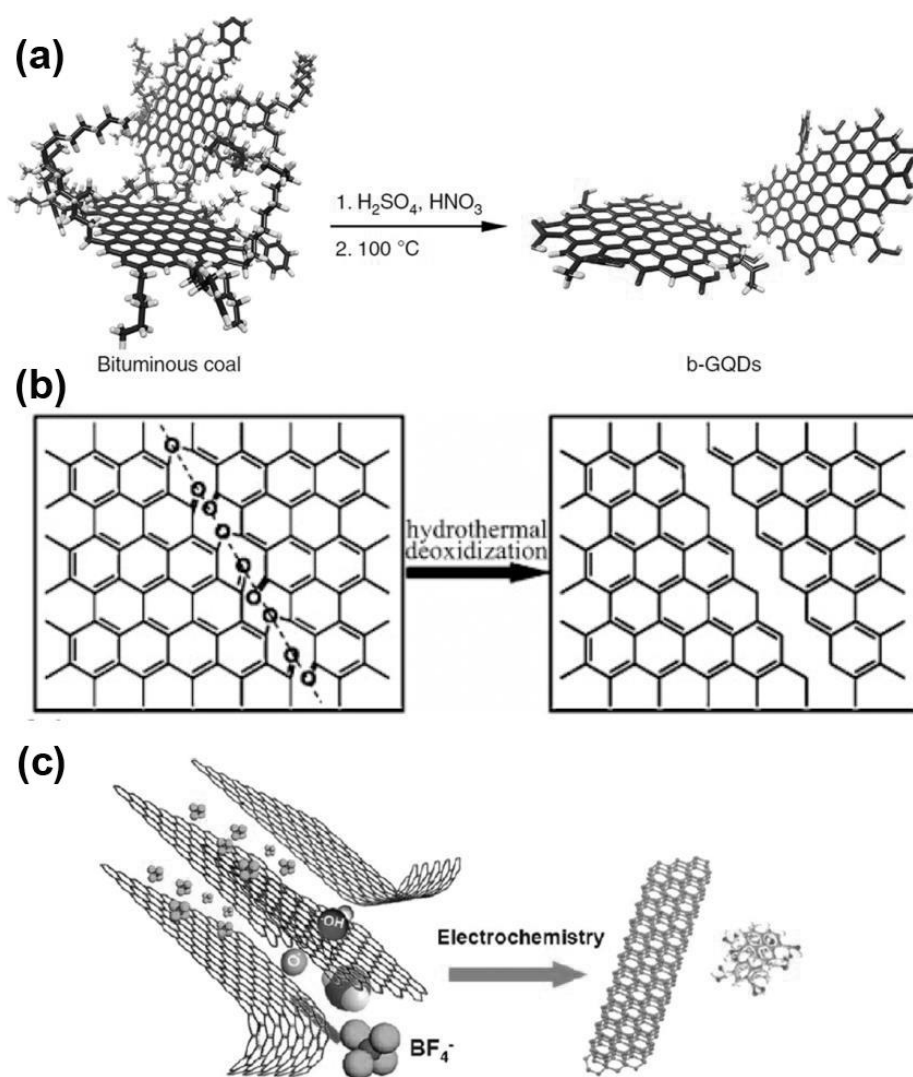


**Figure 2.3** Top-down fabrication of GQDs. Schematic illustration of (a) GQDs synthesis by acidic oxidation of coal. Reproduced with permission.<sup>34</sup> Copyright 2013, Nature Publishing Group; (b) mechanism for the hydrothermal cutting of oxidized graphene sheets into GQDs: a mixed epoxy chain composed of epoxy and carbonyl pair groups (left) is converted into a complete cut (right) under the hydrothermal treatment. Reproduced with permission.<sup>33</sup> Copyright 2010, Wiley-VCH; (c) exfoliation process showing the attack of the graphite edge planes by hydroxyl and oxygen radicals, and intercalation of  $\text{BF}_4^-$  anion. Reproduced with permission.<sup>42</sup> Copyright 2009, American Chemical Society.

*Physical routes:* Microwave irradiation can offer rapid and uniform heating for the reaction medium, and thus can dramatically shorten the reaction time and improve product yields. With the assistance of microwave irradiation, greenish-yellow luminescent single-layered or bi-layered GQDs (2-7 nm) with a QY up to 11.7% were

successfully prepared *via* microwave-assisted cleavage of graphene oxide (GO) under acid conditions.<sup>19</sup>

Ultrasonication of liquids leads to the formation and collapse of small vacuum bubbles due to the alternating low-pressure and high-pressure waves, commonly known as cavitations. These cavitations create high shear forces that can break down larger particles. In the case of GQD synthesis, larger sheets of graphene are subjected to high-energy ultrasonication. For instance, Zhuo *et al.* prepared monodispersed GQDs (3-5 nm) ultrasonically from graphene.<sup>44</sup> These high-energy synthetic strategies help to reduce the reaction time and simplify the reaction procedure.

### **2.2.2 Bottom-up approaches**

*Stepwise organic synthesis:* GQDs can also be prepared *via* wet chemical approaches by the oxidative condensation of aryl groups.<sup>38, 45-51</sup> Yan *et al.* synthesized large colloidal GQDs consisting of graphene moieties containing 168, 132, and 170 conjugated carbon atoms from small-molecule precursors, such as 3-iodo-4-bromoaniline through solution chemistry (Figure 2.4).<sup>45</sup> This approach is based on oxidative condensation reactions, whereby the oxidation of polyphenylene dendritic precursors that were synthesized through stepwise solution chemistry led to fused graphene moieties and consequently GQDs. More recently, uniform multicolor GQDs were also produced by using unsubstituted hexa-peri-hexabenzocoronene as precursor.<sup>38</sup> Generally, this method allows well-controlled synthesis of GQDs with desired size and structure.

For this method, it is very important to prevent the aggregation of the GQDs due to the inter-graphene attraction to maintain a good solubility. It has been reported that by covalently attaching 2',4',6'-trialkyl phenyl groups to the edges of the graphene moieties, stabilized GQDs could be obtained. This is due to the presence of the attached groups,

which form a 3D protecting cage and thus increase the distance between individual graphene sheets, leading to improved stability and solubility.

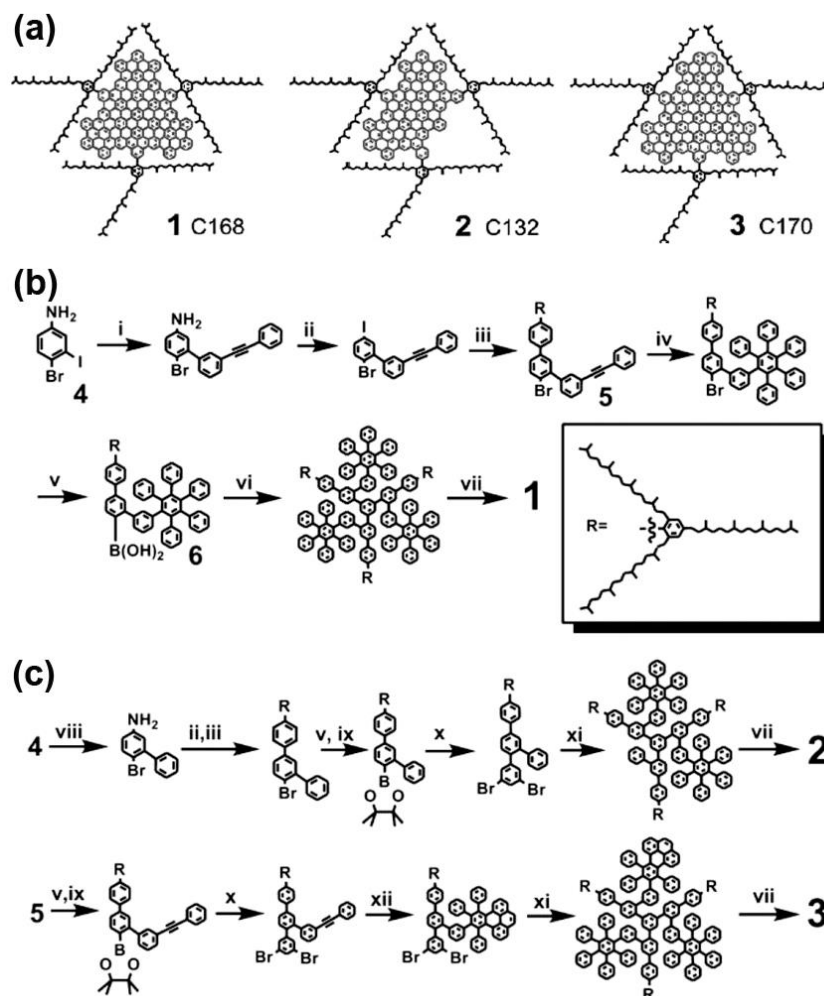


**Figure 2.4** (a-b) Bottom-up synthesis of large GQDs (1-3) from 3-iodo-4-bromoaniline (4) via stepwise organic chemistry. GQDs in (a) consisting of graphene moieties containing 168, 132, and 170 conjugated carbon atoms respectively. Reproduced with permission.<sup>45</sup> Copyright 2010, American Chemical Society.

*Cage opening of fullerene:* Lu *et al.* synthesized GQDs with various geometric structures on a ruthenium catalyst by the ruthenium-catalysed cage-opening of  $\text{C}_{60}$  molecules.<sup>9</sup> In this process, surface vacancies are induced in the single Ru crystal due to the strong interaction between  $\text{C}_{60}$  and Ru. Subsequently, the  $\text{C}_{60}$  molecules are embedded on the Ru surface. The embedded molecules undergo fragmentation at very high temperatures, producing carbon clusters that diffuse and aggregate to form GQDs. The GQD's shape can be tailored by optimizing parameters such as annealing temperature and density of



the carbon cluster. Triangular, parallelogram-shaped, trapezoid-shaped, hexagon-shaped and small hexagonal mushroom-shaped GQDs have been synthesized and the bandgap of GQDs increases with a reduction in their lateral size. This work provides a mechanistic approach to synthesize a series of atomically defined GQDs with tunable bandgap.

*Precursor pyrolysis/ carbonization:* Pyrolysis or carbonization of small organic molecules is a widely reported method for GQD synthesis. Commonly, this mechanism involves heating the small organic molecules above their melting point, leading to condensation, nucleation, and subsequent formation of larger GQDs. The precursors used are small organic molecules such as L-glutamic acid<sup>13</sup> and citric acid.<sup>52</sup> Compared to stepwise organic synthesis, thermal carbonization of carbon precursors usually produces heterogeneous GQDs.

However, these methods are simple, cost-effective, scalable, and allows natural inheritance of heteroatoms from the precursors.

## **2.3 Changing PL properties by chemical modification**

### ***2.3.1 Heteroatom doping***

Heteroatom doping of graphene has been observed to endow them with new physicochemical, optical, electromagnetic and structural properties. This phenomenon is extend to GQD, a 0D graphene material, whereby heteroatom doping can tailor the PL properties of GQDs.<sup>53</sup> In general, N-doped GQDs have been found to exhibit better PL properties than their undoped counterparts. A hydrothermal approach was developed to fabricate N-doped GQDs by cutting N-doped graphene.<sup>54</sup> This hydrothermal cutting method may allow us to tap into the large variety of heteroatom doping methods for graphene and select suitable methods to obtain a wide range of doped GQDs. The downside of the method is the low production efficiency.

Hu *et al.* have demonstrated the synthesis of N-doped GQDs with high N/C atomic ratio (17.88%) by using hydrothermal treatment of GO in the presence of ammonia. The N-doped GQDs showed the presence of both pyridine-like and pyrrolic nitrogen atoms. The as-prepared N-doped GQDs were highly blue luminescent with a QY as high as 24.6%.<sup>55</sup> Similarly, nitrogen atoms have been successfully doped in the GQD lattice by simple hydrothermal treatment of un-doped GQDs with hydrazine.<sup>56</sup> N-doping increased GQD QY from 4.8% to 23.3%.

Nitrogen atoms can also be introduced into the GQDs *in situ* by electrochemical synthesis in acetonitrile with N-containing tetrabutylammonium perchlorate (TBAP) as electrolyte. The presence of pyridinic and pyrrolic nitrogen atoms were observed from the high resolution N<sub>1s</sub> spectrum of the N-doped GQDs. As compared to their undoped green fluorescent counterparts, the synthesized N-doped GQDs emit blue PL as a result of the relatively strong electron-withdrawing ability of nitrogen atoms.<sup>28</sup>

Different from aforementioned approaches, chemical synthesis from small molecule precursors provides another way to design and control the number and sites of nitrogen atoms within the backbone of the final N-doped GQDs. For example, N-doped GQDs were prepared by a solution chemistry route by using substituted benzene derivatives as starting materials.<sup>27</sup> This remarkable method provides a platform to study the effect of heteroatom doping on the properties of GQDs both theoretically and experimentally. Unfortunately, the as-prepared N-doped GQDs tend to aggregate irreversibly.

Tang *et al.* reported a one-pot microwave-assisted method for N-GQD synthesis using glucose and ammonia as precursors.<sup>57</sup> The N-GQDs exhibited a broad range of PL peaked at 302, 542, and 915 nm when excited by 197, 475, and 808 nm light, respectively. The broad-range PL emission is attributed to the layered structure of the N-GQDs, which consists of a large conjugated system containing extensive delocalized  $\pi$  electrons.

Other elements (e.g., S<sup>50a</sup> and B<sup>58, 59</sup>) have also been doped in GQDs to change PL characteristics or gain catalytic properties. S and N co-doped GQDs can attain QY as high as 73% and 71%, respectively.<sup>4, 60</sup>

### ***2.3.2 Controlling Surface Oxidation***

Controlling the degree of surface oxidation by the addition of oxygenated functional groups is a simple but effective way to tune PL and render GQDs with chemical handles for bioconjugation.

Localized sp<sup>2</sup> clusters and structural defects can be altered by varying the concentration of oxygenated groups, thus changing PL properties. Greenish-yellow luminescent GQDs prepared by a microwave-assisted method have a QY of 11.7%. After NaBH<sub>4</sub> reduction, the GQDs are blue luminescent with a increased QY of 22.9%. The dimensions of GQDs were identical before and after reduction, suggesting that the PL blue-shift of GQDs is due to the reduction induced structural change rather than size effect.<sup>19</sup>

Utilizing gradient elution, three types of GQDs prepared by solvothermal methods with similar sizes, but increasing degree of surface oxidation were obtained. Higher amounts of surface oxidation lead to more surface defects, resulting in the red-shifting of emission from blue to green. The QYs were measured to be 4.1, 9.9 and 12.2%, respectively.<sup>16</sup> The green luminescent GQDs with QY of 5.9% were further reduced by NaBH<sub>4</sub> to obtain blue luminescent GQDs with higher QY of 12.1%. It is speculated that the carbonyl, epoxy and amido moieties were changed into hydroxyl groups in GQDs upon reduction, which suppressed non-radiative processes, enhanced integrity of  $\pi$ -conjugated system and reduced the defects.<sup>61</sup>

Besides chemical reduction, photochemical reduction of GQDs with UV lamp have been reported to result in blue-shift in emission wavelength and a concurrent 3.7 fold increase in the QY. The increase in QY may be attributed to the increase in sp<sup>2</sup> domain and the

formation of a great amount of electron-donating hydroxyl groups during the photochemical reduction.<sup>62</sup>

### **2.3.3 Polymer Passivation**

The QY of GQDs is known to improve by polymer passivation. Shen *et al.* synthesized bare GQDs and GQDs passivated with PEG and found that QY of the latter was doubled.<sup>63</sup> Polyethylene glycol has been commonly reported as a surface passivation agent for GQDs.<sup>64,17,37,65</sup>

### **2.3.4 Surface Modification with Small Molecules**

Surface functionalization of GQDs has been explored to fine-tune their PL properties. The redox potentials, which dictate charge transfer processes in GQDs, can be controlled by chemical modifications with electron donating or electron withdrawing functional groups. The electron-donating groups generally increase the HOMO levels, and electron-withdrawing groups lower the LUMO levels. As an example, attaching electron-withdrawing functionalities such as carboxylic groups to the peripheries of GQDs suppresses their HOMO and LUMO levels simultaneously, thus changing their redox potentials.<sup>66</sup> Surface and edge functionalization of GQDs were approached by varying the surface density of carboxylic and carbonyl groups, and sometimes by substituting them with other chemical groups such as amino groups.<sup>3</sup>

Blue luminescent GQDs were prepared from green luminescent GQDs *via* chemical modification with alkylamine.<sup>61</sup> During chemical modification, the originally existing carboxyl and epoxy groups are replaced with -CONHR and -CNHR. Since the carboxy and epoxy groups in GQDs induce non-radiative recombination of localized electron-hole pairs resulting in a lower QY of 5.9%, the alkylamine mediated modification resulted in GQDs with QY of 6.5%. Tetsuka *et al.* employed an ammonia-mediated bond scission

reaction to modify the edges of GQDs with amino groups and successfully obtained GQDs with a high QY of 40%. Moreover, the emission wavelength could be properly tuned by controlling the degree of amine functionalization, which is in turn dependent on the initial concentration of ammonia and the reaction temperature. The resonance between the molecular orbital in the -NH<sub>2</sub> group and the delocalized  $\pi$  orbital accounts for both the PL tunability and the high QY.<sup>67</sup>

Hydrazine treatment of the electrochemically synthesized GQDs led to the formation of hydrazide groups on the GQDs *via* the reaction of hydrazine with the peripheral carboxyl groups at the edge. The GQDs emitted strong yellow PL due to a high concentration of modified hydrazide groups.<sup>30</sup> Only weak blue PL was observed if NaBH<sub>4</sub> was used instead keeping other conditions the same.

## **2.4 Biological Applications**

### ***2.4.1 Cellular Imaging***

GQDs are widely used as cell imaging agents due to their small size and high biocompatibility. Strongly green fluorescent single-layered or bi-layered GQDs prepared solvothermally from graphene oxide were demonstrated to be excellent bioimaging agents.<sup>12</sup> Confocal fluorescence microscopy images showed bright green fluorescence inside the cytoplasm of human osteosarcoma MG-63 and mouse osteoblast MC3T3 cells, indicating the translocation of GQDs through the cell membrane. Similarly, water-soluble and well-crystallized green GQDs fabricated by hydrothermal cutting of graphene sheets were also successfully applied for cellular imaging.<sup>36</sup> HeLa cells incubated with these GQDs displayed enhanced fluorescence around the nucleus. It is worthy to note that GQD-labeled cells exhibit no obvious reduction in PL intensity after 10 min continuous excitation, suggesting their potential for long-term dynamic tracking experiments. Green GQDs obtained from the acid treatment of carbon fibers have been used to successfully stain the cytoplasm of T47D cells with the nucleus co-stained using blue DAPI after 4 h

incubation.<sup>29</sup> Cellular bioimaging using GQDs was also successful in murine alveolar macrophage (MH-S) cells<sup>13</sup> and human hepatic cancer cells (Huh7).<sup>68</sup> So far, most cellular imaging studies that utilize GQDs merely showed their uptake into cellular cytoplasm after a short incubation period. The exact subcellular compartment that the GQDs localized in has not been determined. It is also not clear whether different types of GQDs synthesized *via* various routes exhibit the same cellular uptake and intracellular distribution. A detailed fluorescence co-localization study is necessary to pinpoint the subcellular localization of internalized GQDs. In addition, the uptake mechanism of GQDs should also be investigated in depth.

The currently available cell imaging results indicate that most GQDs are only internalized into the cytoplasm, but there are also a few exceptions. Single-layer green GQDs (~ 15 nm) prepared by chemical oxidation of carbon black (QY = 4.04%) were able to label both the cytoplasm and nucleus of MCF7 breast cancer cells.<sup>35</sup> The GQDs were not functionalized with any specific nuclear targeting groups.

The charge, functionalization or oxidation state of the GQDs is speculated to exert significant effects on their cellular penetration capability. As an example, photochemically reduced GQDs (pGQDs) labeled A549 cells were internalized more effectively than chemically reduced GQDs (cGQDs), possibly because the less negative overall charge of pGQDs resulting from the reduced amount of carboxyl groups as compared to cGQDs.<sup>62</sup> It will be interesting to carry out more studies in this respect so that GQDs can be tailored made to improve their cellular uptake efficiency as well as to control their intracellular distribution.

Besides commonly used cell lines, GQDs have been applied in direct labeling of stem cells, which is considered as a challenging task due to the stem cell's sensitivity to nanomaterial toxicity.<sup>31, 69</sup> Highly fluorescent yellow single-layer GQDs with phthalhydrazide-like groups and hydrazide groups at the edges were successfully

internalized by three kinds of stem cells including neurospheres cells (NSCs), pancreas progenitor cells (PPCs) and cardiac progenitor cells (CPCs) after 24 h incubation at 37°C. The confocal section images further confirmed the efficient uptake of GQDs into the cytoplasm of these stem cells rather than being merely adsorbed on the outer cell membrane.<sup>30</sup> Studies by Shang *et al.* have revealed that the uptake of GQDs into human neural stem cells *via* endocytosis in a concentration- and time- dependent manner.<sup>31</sup> Apart from these reports that focused on the normal linear fluorescence of GQDs for imaging, there are also few reports on the cell imaging on GQDs using their non-linear fluorescence properties. The ability of monolayer N-GQDs for two-photon imaging was investigated using human cervical carcinoma (HeLa) cells under 800 nm excitation.<sup>14</sup> The fluorescence images clearly revealed the distribution of N-GQDs around each nucleus and z-axis imaging further confirmed the successful uptake of N-GQDs into cytoplasm rather than adsorbed on the cell surfaces.

#### ***2.4.2 Real-time cell tracking***

Real-time tracking of dynamic cellular processes requires excellent fluorescent tags that are bright, photo-stable, easily conjugated with biomolecules, biocompatible and with molecular size to minimize physical hindrance. Insulin-conjugated GQDs have been synthesized and used for real-time tracking of the dynamics of insulin receptors in 3T3-L1 adipocytes using total internal reflection microscopy (TIRFM) as presented in Figure 2.5.<sup>70</sup> The as-synthesized single-layer GQDs with an average diameter of 2.2 nm are comparable to a protein of a few kDa in size. As such, the GQD tags do not significantly increase the overall weight of GQD-protein conjugates and they do not pair with multiple biomolecules. The abundant carboxyl groups on the edges of the GQDs allow them to be easily conjugated with a variety of proteins *via* a general EDC/NHS conjugation strategy. Currently, the trafficking dynamics of insulin receptors remains poorly studied partly due

to the lack of effective labeling methods for live-cell imaging. The real-time tracking experiments utilizing GQD-insulin conjugates revealed, for the first time, that the internalization and recycling of insulin receptors in adipocytes were enhanced by apelin but inhibited by tumor necrosis factor  $\alpha$  (TNF $\alpha$ ), providing evidence for the molecular mechanisms underlying the regulation of these cytokines on insulin sensitivity. The use of monodispersed, single-layer and small-sized GQDs with satisfactorily high QY is the key for successful application in real-time tracking of dynamic molecular events.

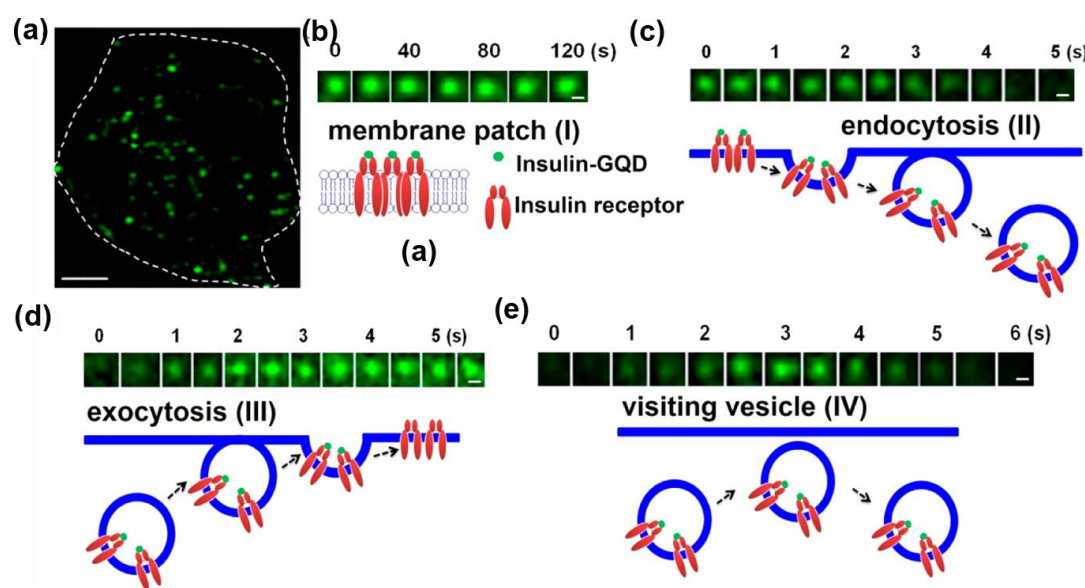


**Figure 2.5** (a-e) Application of insulin-GQD conjugates for real-time tracking of insulin receptors in adipocytes. (a) Total internal reflection fluorescence microscopy (TIRFM) image of a 3T3-L1 adipocyte after 1 h incubation with insulin conjugated GQDs. Scale bar = 5  $\mu\text{m}$ . (b) Membrane patch consisting of insulin conjugated GQD/insulin receptor clusters. (c) Endocytosis of fluorescent membrane into a vesicle. (d) Exocytosis of a vesicle containing insulin conjugated GQD/insulin receptor complexes. (e) Transient approaching and retrieval of insulin conjugated GQD/insulin receptor containing vesicle. Scale bars = 0.2  $\mu\text{m}$ . Reproduced with permission<sup>70</sup>. Copyright 2013, American Chemical Society.

### 2.4.3 In-vivo imaging

N-GQDs prepared solvothermally using graphene oxide as precursor and DMF as nitrogen source, achieve a large imaging penetration depth of 1800  $\mu\text{m}$  and also show low photobleaching and photothermal effects under repeated excitation under femtosecond NIR laser.<sup>14</sup> These parameters indicate that N-GQDs are excellent two-photon probes



well-suited for long-term dynamic deep tissue imaging. In addition, polydopamine-coated GQDs (8-24 nm) were injected intravenously into nude mice and were successfully visualized to track the location of GQDs in different organs. The *in vivo* biodistribution of the GQDs changed according to the size and polydopamine coating thickness.<sup>71</sup>

#### **2.4.4 Biosensing**

The PL, electronic and electrochemical properties of GQDs have been found to be sensitive to various parameters, which render them with great potential of transforming into nanosensors. Moreover, their sizes are in the range of several nanometers, which are similar to small biomolecules, allowing them to intimately interact with biomolecules without disrupting their physiological functions.

*PL sensors:* Biological thiols like cysteine (Cys), homocysteine (Hcy) and glutathione (GSH), are involved in many syndromes such as pregnancy complications and cardiovascular disease, cancer and AIDS. A novel, rapid and label-free assay was developed to detect biothiols using GQDs as fluorescence indicators.<sup>72</sup> The electrostatic attachment of Ag<sup>+</sup> ions on the GQD surfaces caused the formation of Ag nanoparticle (AgNPs), which was quenched GQD fluorescence. The addition of biothiols led to a further decrease in fluorescence due to their reducing nature and bridging of adjoining AgNPs through Ag-S bonds. A good linear relationship between quenching ratio and the concentration of Cys over the range of 0 - 100 nM was observed with a detection limit of 6.2 nM. Meanwhile, Hcy and GSH also showed similar linear range, with detection limit of 4.5 nM and 4.1 nM, respectively. The detection limit achieved is much lower or at least comparable to previously reported fluorescence-based methods. Notably, the thiol detection in human plasma was successfully demonstrated.

Using GQDs with a boronic acid substituted bipyridinium salt (BBV), a fast and convenient label-free fluorescence assay for glucose and other monosaccharides was reported by Li *et al.*<sup>73</sup> The electrostatic attraction between GQDs and BBV led to the formation of a ground-state complex that facilitated the excited-state electron transfer from GQDs to bipyridinium, leading to fluorescence quenching. Upon glucose addition, the boronic acids were converted to tetrahedral anionic glucobornate esters, effectively neutralising the net charge of the cationic bipyridinium, diminishing the quenching efficiency and recovering the GQD fluorescence. The linear relationship between the recovered fluorescence intensity and the glucose concentration ranged from 1 mM to 60 mM, suitable for clinical measurement of blood glucose level.

Blue fluorescent glutathione-functionalized GQDs (GSH-GQDs) with a QY of 33.6% were used to measure the adenosine triphosphate (ATP) level in cell lysate and human blood serum.<sup>74</sup> The fluorescence of GSH-GQDs was first quenched in the presence of  $\text{Fe}^{3+}$ . ATP molecules were expected to complex with  $\text{Fe}^{3+}$  through Fe-O-P bond formation, resulting in fluorescence recovery. The linear relationship between  $[(F-F_0)/F_0]$  and the ATP concentration in the range of 25-250  $\mu\text{M}$ . The detection limit was estimated to be 22  $\mu\text{M}$ .

Amjadi *et al.* were the first to apply the GQD-Ce(IV) chemiluminescence system for uric acid detection which exhibited excellent analytical performance in the range of 1.0  $\mu\text{M}$  to 0.5 mM with a detection limit of 0.5  $\mu\text{M}$ .<sup>75</sup> This method also achieved good accuracy when applied to determine uric acid concentration in human plasma or urine samples.

In addition to ions and small molecules, GQD-based PL sensors have also been used to detect large biomolecules such as proteins and DNAs. A fluoro immunoassay has been developed for sensitive detection of human immunoglobulin G (IgG) by regulating luminescence resonance energy transfer (LRET) between graphene and GQDs.<sup>10</sup> When graphene was added to mouse anti-human IgG (mIgG) conjugated GQDs, graphene and

GQDs were brought into LRET proximity by the  $\pi$ - $\pi$  stacking between graphene and GQDs and the non-specific binding between mIgG and the surface of graphene, resulting in fluorescence quenching. The addition of target human IgG results in its binding to mIgG due to the specific antibody-antigen interaction, which increases the distance between mIgG-GQDs and graphene effectively hindering the LRET process and restoring the fluorescence. The PL intensity increases with increasing concentration of human IgG in the range from 0.2  $\mu\text{g mL}^{-1}$  to 12  $\mu\text{g mL}^{-1}$ , achieving a detection limit of 10ng/mL. Sensitive detection was also demonstrated in serum and cell culture media, indicating the practical use of this biosensor. This immunosensing scheme is universal and can be modified to specifically detect other antigens.

Protein kinases are enzymes that are responsible for the enzymatic phosphorylation of proteins. They play important roles in intracellular signal transduction and the regulation of cellular functions. Wang *et al.* have demonstrated a unique sensing strategy for profiling protein kinase activity based on the aggregation induced quenching of GQD fluorescence.<sup>76</sup> As illustrated in Figure 2.6b,  $\text{Zr}^{4+}$  ions mediate the coordination of multiple phosphorylated sites of phosphopeptides resulting in aggregation. When a GQD conjugated substrate peptide is phosphorylated by casein kinase II (CK2) in the presence of  $\text{Zr}^{4+}$  ions, it results in extensive aggregation and quenching of GQD PL. The PL intensity of peptide-GQD conjugates was linearly dependent on the CK2 concentration in the range from 0.1 to 1.0 unit  $\text{mL}^{-1}$  with a detection limit of 0.03 unit  $\text{mL}^{-1}$  (Figure 2.6b-c). In comparison to existing fluorescent kinase assays, this method showed many advantages such as rapidity, simplicity, low cost, high sensitivity and selectivity. This method is also general, since the peptide sequence can be designed to detect the activity of other enzymes.

Qian *et al.* devised a highly selective and sensitive fluorescence sensing approach for DNA detection based on FRET between rGQD-labeled DNA probe and GO.<sup>77</sup> ssDNA-

rGQDs probes were adsorbed onto the surfaces of GO through electrostatic interactions or  $\pi$ - $\pi$  stacking, leading to fluorescence quenching. Target DNAs can hybridize with the ssDNA-rGQDs, forming dsDNA-rGQDs, which detach from GO, resulting in fluorescence recovery. This DNA detection method has a linear range of 6.7-46.0 nM with a detection limit of 75.0 pM.

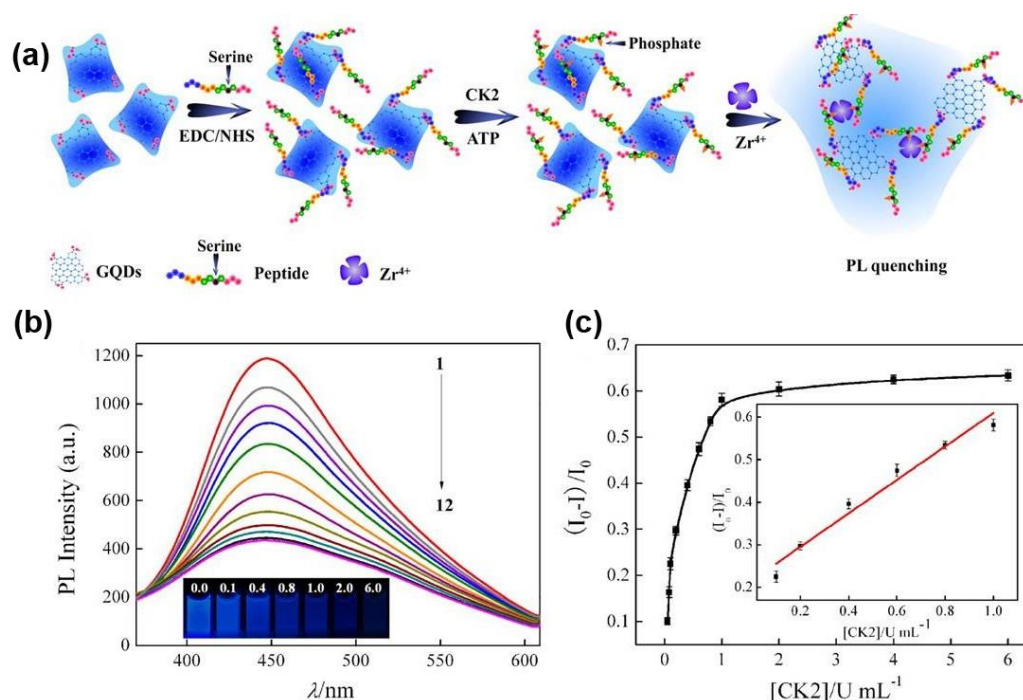


**Figure 2.6** (a) Schematic representation of the CK2 kinase assay based on the aggregation and PL quenching of phosphorylated peptide-GQD conjugates *via* Zr<sup>4+</sup> ion linkages. (b) PL quenching of peptide-GQDs treated with various amounts of CK2 followed by the addition of 0.2 mM Zr<sup>4+</sup>. The concentrations of CK2 were 0, 0.05, 0.08, 0.1, 0.2, 0.4, 0.6, 0.8, 1.0, 2.0, 4.0, and 6.0 units mL<sup>-1</sup> for curves 1 to 12, respectively. The concentration of ATP was 50  $\mu$ M. The inset shows the PL quenching of peptide-GQD solutions illuminated with a UV lamp at the homologous CK2 concentrations of (left to right) 0, 0.1, 0.4, 0.8, 1.0, 2.0, and 6.0 units mL<sup>-1</sup>. (c) Plot of the relative PL intensity  $[(I_0 - I)/I_0]$  at 445 nm *vs* CK2 concentration.  $I$  and  $I_0$  are the PL intensities in the presence and absence of CK2, respectively. Reproduced with permission.<sup>76</sup> Copyright 2013, American Chemical Society.

**Electrochemiluminescence (ECL) sensors:** ECL is a unique and sensitive analytical method. As the light emitting species are generated in situ close to electrode surface, ECL has nearly zero background and allows temporal and spatial control over the reaction. The

intense and stable ECL of GQDs has been utilized for ultrasensitive detection of ATP (as low as 1.5 pM).<sup>21</sup> ATP molecules enhance ECL signal in dose-dependent manner because they facilitate the attachment of complementary ssDNA-functionalized GQDs onto probe ssDNA functionalized electrode. A DNA sensor with a detection limit of 13 nM was devised based on a different strategy.<sup>20</sup> Specifically, ECL signal from GQDs on electrode is first quenched by probe-ssDNA conjugated gold nanoparticles (AuNPs) due to ECL resonance energy transfer; and detection is then reported by ECL recovery upon release of AuNPs by hybridization with target ssDNAs. Ratiometric ECL measurement on GQDs (one peak depends on target concentration; the other serves as stable internal reference) has been used to detect  $\text{Fe}^{3+}$  ions with good sensitivity (0.7  $\mu\text{M}$ ) and reproducibility.<sup>78</sup>

*Electrochemical Sensors:* Large active surface areas, edge-facilitated electron transfer, high catalytic activity and chemical stability of GQDs render them fundamentally applicable as electrochemical sensors. Zhao *et al.* designed an electrochemical biosensor using GQDs-modified pyrolytic graphite electrode with specific ssDNA molecules as probes.<sup>79</sup> When the probe DNA sequences were strongly bound to the electrode surface, the probe DNAs inhibited the electron transfer between the electrochemically active species  $[\text{Fe}(\text{CN})_6]^{3-/4-}$  and the electrode. However, the probe ssDNA could bind with the complementary ssDNAs or target protein thrombin, which altered the structure of probe ssDNA and in turn disturbed the adsorption of the probe on the GQDs-modified electrode, finally resulting in the recovery of the peak currents of  $[\text{Fe}(\text{CN})_6]^{3-/4-}$ . The detection limits for complementary ssDNA and thrombin were both 100 nM. With the discovery of new aptamers, this electrochemical biosensor can be extended to detect more targets, for the effective and rapid detection of specific biomolecules critical in medical diagnosis.

Besides DNA molecules, enzymes such as glucose oxidase (GOx) can be immobilized on GQD-modified electrodes to fabricate glucose sensors based on direct electrochemistry.<sup>80</sup> The small size of GQDs may be the key for easy access to the catalytic centers and thus greatly facilitating electron transfer. The heterogeneous electron transfer rate constant ( $k_s$ ) and electron transfer coefficient ( $\alpha$ ) for the redox reaction of GOx were found to be 1.12 s<sup>-1</sup> and 0.48, respectively. This biosensor achieved a detection limit of 1.73  $\mu$ M over the concentration range of 5 to 1270  $\mu$ M. The high surface coverage ( $1.8 \times 10^{-9}$  mol cm<sup>-2</sup>) confirmed an excellent enzyme loading, possibly due to the large specific surface area of GQD-modified electrode. The small Michaelis-Menten constant (0.76 mM) indicated a high affinity of biosensor to glucose, which accounted for the excellent performance of this electrochemical glucose biosensor. The performance of the biosensor can be attributed to the large surface-to-volume ratio, excellent biocompatibility of GQD, porosity of GQD-modified carbon ceramic electrode, and the abundance of hydrophilic edges as well as hydrophobic plane in GQD which enhances the enzyme absorption on the electrode surface. This biosensor was also accurate in determining glucose concentration in human plasma samples, indicating the practicality of such biosensor in clinical analysis.

Instead of simple drop-casting, Zhang *et al.* covalently modified gold electrodes with GQDs using cysteamine as cross-linkers for H<sub>2</sub>O<sub>2</sub> sensing. The cathode current of GQD-modified gold electrode showed a good linear range from 0.002 to 8 mM with a detection limit of 0.7  $\mu$ M, comparable or even better than many HRP immobilized Au electrodes.<sup>25</sup> The stability and reusability of the GQDs/Au electrode were dramatically improved compared to the drop-casted GQDs. The GQDs/Au electrode maintained a good electrocatalytic activity without significant loss of current response after more than 30 days of storage at ambient temperature. Furthermore, it still maintained 90% current response after more than 20 uses. Most notably, the as-prepared electrode was

successfully demonstrated to monitor the dynamic  $\text{H}_2\text{O}_2$  release in human breast adenocarcinoma MCF-7 cells.

*Colorimetric Sensors:* GQDs have also been found to possess intrinsic peroxidase-like catalytic activity due to their  $\text{sp}^2$  carbon clusters. GQDs were observed to react with a peroxidase substrate ABTS in the presence of  $\text{H}_2\text{O}_2$ . The absorbance change of ABTS at 416 nm was then used to monitor the reaction rate for label-free colorimetric detection of  $\text{H}_2\text{O}_2$ . This assay provides fast detection time (2 min), low detection limit (20  $\mu\text{M}$ ) and large linear range (0.1 mM to 10 mM).<sup>13</sup>

Recently, Chen *et al.* synthesized GQDs/AgNPs (6-15 nm) in situ, which was found to catalyze the reduction of  $\text{H}_2\text{O}_2$ .<sup>81</sup> The conversion of AgNPs to  $\text{Ag}^+$  leads to a sensitive decrease in the characteristic absorbance of AgNPs at 405 nm, providing a way for ultrasensitive colorimetric detection of  $\text{H}_2\text{O}_2$ .<sup>82</sup> The linear range for  $\text{H}_2\text{O}_2$  detection is from 0.1-100  $\mu\text{M}$  with a record-low detection limit of 33 nM. Glucose oxidase (GOx), which can specifically catalyze the oxidation of glucose in the presence of oxygen to form  $\text{H}_2\text{O}_2$ , was combined with GQDs/AgNPs for highly sensitive colorimetric detection of glucose. Glucose can be detected in the range of 0.5 - 400  $\mu\text{M}$ , with a detection limit of 170 nM, a 100-fold lower than the previous report.

#### **2.4.5 Drug delivery**

Graphene and graphene oxides have been shown to possess excellent drug loading capability due to their large surface area. It is widely believed that GQDs can be good drug carriers with the large surface area suitable for drug/gene loading and their small sizes that can enhance cellular uptake. As a pioneering work, PEGylated nanographene oxide (NGO-PEG) was applied by Dai *et al.* for the delivery of insoluble aromatic drug SN38.<sup>83</sup> The resultant NGO-PEG-SN38 complexes were highly soluble and were highly

potent in killing cancer cell. 50% growth inhibition was achieved with a concentration (IC<sub>50</sub>) of 6 nM for HCT-116 cells, which was 1000 fold more potent than CPT-11 (a FDA approved SN38 prodrug for clinical colon cancer treatment). They also demonstrated the efficient physisorption of doxorubicin onto anti-CD20 conjugated NGO-PEG *via*  $\pi$ - $\pi$  stacking for targeted killing of Raji B-cell lymphoma.<sup>84</sup>

As expected, GQDs passivated with PEG has been shown to possess good drug loading capacity. Using water soluble anticancer drug doxorubicin as a model drug, a loading of 2.5 mg/mg was recorded at pH 7.4, and the release was fastest with 75% accumulated release after 48 h under acidic conditions at pH 5.5.<sup>85</sup>

To improve targeting specificity, hyaluronic acid (HA) moieties were anchored to GQDs to achieve targeted delivery to CD44-overexpressed tumors.<sup>64</sup> HA-GQDs were able to load ~75% of doxorubicin initially applied, indicating them as excellent agents for loading hydrophobic drug molecules. The release of DOX was fastest within first 6 h reaching 42%, which was increased to ~ 60% within 12 h and almost complete release was achieved within 48 h at pH 5.5. In contrast, drug release at pH 7.4 was much slower with only 20% release after 48 h. This pH dependent release behavior is advantageous since tumor tissues commonly have a slightly acidic environment. In addition, the specific targeting ability of HA-GQDs was confirmed by both *in vivo* investigation using balb/c female mice and *in vitro* test with A549 cells.

Wang *et al.* showed that single-layered GQDs without any pre-modification could efficiently accelerate DOX accumulation to the nucleus and also enhance DNA cleavage activity of DOX markedly, leading to a dramatic improvement in the cytotoxicity of DOX. Most notably, the DOX/GQD conjugates increase nuclear uptake and cytotoxicity of DOX in drug-resistant MCF-7 breast cancer cells.<sup>86</sup> This encouraging result promises further applications of GQDs in drug delivery vector design.



GQDs have also been explored as fluorescent tracers in drug delivery. Jing *et al.* developed a multifunctional core-shell capsule with GQDs encapsulated as fluorescent labels.<sup>87</sup> The composite was composed of olive oil for loading of paclitaxel. A TiO<sub>2</sub> shell suppressed the initial burst release of the paclitaxel. Fe<sub>3</sub>O<sub>4</sub> and GQDs present inside the oil core were used for magnetic targeting and fluorescence imaging, respectively. In this work, GQDs encapsulated acted as fluorescent tracers for capsule targeting and markers for drug release upon breaking of the capsules, thus providing important optical information for *in situ* monitoring of drug release process. Similarly, Nigam *et al.* also used GQDs as fluorescent tags in drug delivery.<sup>88</sup> They conjugated GQDs to hyaluronic acid-functionalized human serum albumin (HSA) for simultaneous bioimaging and targeted delivery of gemcitabine to pancreatic cancer.

Single-layered GQDs were capped onto the nanopores of mesoporous silica nanoparticles (MSNs) through an acid-cleavable acetal bond and their application for simultaneous drug delivery and cell imaging was investigated by Chen *et al.*<sup>89</sup> After incubating doxorubicin loaded GQDs@MSNs with A549 (human lung carcinoma) cells, green fluorescence of GQDs were observed throughout the cytoplasm, at the same time, the red fluorescence of DOX was found in the entire cell, indicating the intracellular release of DOX triggered by the mild acidic conditions in cancer cells. The GQDs serve dual purposes in this drug release system, not only act as a capping agent to allow pH-triggered drug delivery but also act as imaging agent for tracking of the drug delivery system.

#### **2.4.6 Anticancer Agents**

Electrochemically produced GQDs have been found to generate reactive oxygen species (ROS) such as singlet oxygen under the irradiation of blue light (470 nm, 1W). The ROS generation upon irradiation may be ascribed to the presence of the defects at the surface

of GQDs, but the detailed mechanism need to be further investigated. The increased cellular ROS level caused severe oxidative stress which induced apoptosis and autophagy in human glioma U251 cells.<sup>90</sup> This result suggests that GQDs could be exploited in photodynamic therapy.

GQDs used as DNA cleavage system also prove effective for cancer treatment. Zhou *et al.* discovered that about 90% supercoiled DNA was converted into nicked DNA using GQDs and  $\text{Cu}^{2+}$ , while only about 59% cleavage occurred with the same amount of large-sized GO and  $\text{Cu}^{2+}$ .<sup>82</sup> They speculated that the higher efficiency of GQDs for DNA cleavage is because the small-sized GQDs intercalate DNA molecules better than micrometer-sized GO sheets. A systematic investigation on the mechanism of GQDs in enhancing nuclease activity of copper complex was later carried out by Zheng *et al.*<sup>91</sup> GQDs were found to promote the reduction of  $\text{Cu}^{2+}$  ions and accelerate their reactions with  $\text{O}_2$ , forming superoxide anions and copper-centered radicals. These reactive species oxidatively cleaved DNA molecules (Figure 2.7). The enhancement effect was attributed to the efficient electron-transfer between the electron-rich GQDs and the copper complexes through the effective coordination of GQDs to the copper center. These GQD-based DNA cleavage systems are speculated to have potential applications in anti-cancer therapeutics.

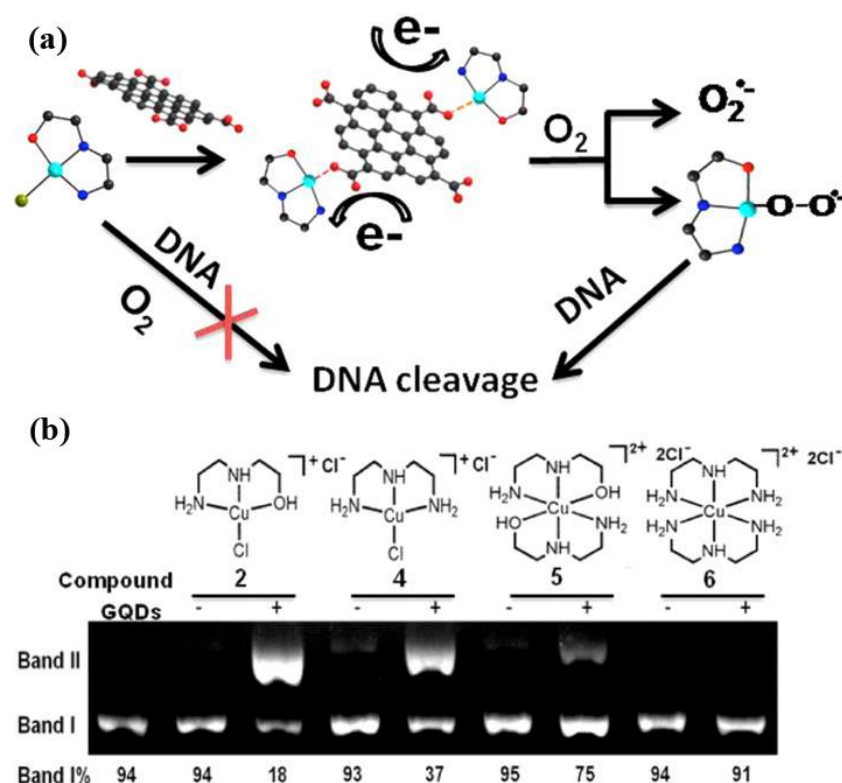


**Figure 2.7** (a) GQD enhances the reduction of copper ions, promoting the formation of oxidative species and consequent DNA cleavage. (b) Gel electrophoresis diagram of DNA (38  $\mu$ M in bp) cleavage by copper complexes 2, 4, 5 and 6 in the absence and presence of GQDs (100  $\mu$ g mL $^{-1}$ ) in 50 mM Tris/18 mM NaCl buffer (pH 7.2) at 37  $^{\circ}$ C. Incubation time was 0.5 h. First lane on the left is the DNA control. Reproduced with permission.<sup>91</sup> Copyright 2014, American Chemical Society.

#### 2.4.7 Antibacterial activity

Infectious diseases induced by bacteria are a worldwide health problem and antibacterial materials are widely used to protect the public health. GQDs possess high peroxidase-like activity due to their excellent electron transport capability. Taking advantages of both peroxidase-like activity and excellent biocompatibility of GQDs, an antibacterial system based on GQDs and low dose of  $H_2O_2$  has been designed by Sun *et al.*<sup>92</sup> The GQDs can convert  $H_2O_2$  with low antibacterial activity into  $\cdot OH$  radicals with high antibacterial activity, thus it is possible to avoid using high concentration of  $H_2O_2$  in wound disinfection. The designed system was tested to possess broad-spectrum antibacterial

activity against both Gram-negative and Gram-positive bacteria. Moreover, GQD-Band-Aids were prepared which showed excellent antibacterial property *in-vivo*.

Mycoplasma is a major problem in clinical medicine. In addition, mycoplasma is a common contamination source in cell culture and is difficult to eliminate. For the first time, amine-functionalized GQDs prepared by Jiang *et al.* were found to exhibit good antimycoplasma properties.<sup>93</sup> HeLa cells were observed to tolerate *M. urealyticum* in the presence of GQDs. Moreover, the cellular viability of HeLa cells increased as the GQD concentration was increased from 10  $\mu\text{g mL}^{-1}$  to 50  $\mu\text{g mL}^{-1}$ . The cytoprotection mechanism of amine-functionalized GQDs may be related to their peroxidase-like activities. It is worth noting that the minimum dose of GQDs (10  $\mu\text{g mL}^{-1}$ ) applied here was comparable with the commercial mycoplasma removal agent BM-Cyclin containing the macrolide tiamulin. These GQDs are potential antimycoplasma agents, which will widen their application in biomedicine.

This chapter is partly adapted / reproduced with permission from our review article. “Glowing Graphene Quantum Dots and Carbon Dots: Properties, Syntheses, and Biological Applications Small, 2014, 11, 1620.” Copyright 2014, Wiley VcH.

## Chapter 3 Facile Synthesis of Graphene Quantum Dots from 3D graphene for Fe<sup>3+</sup> Ion Sensing

As discussed in Chapter 2, top-down approaches for GQD synthesis gives a higher production yield of GQDs. Chemical exfoliation is the most commonly used method; however, the GQDs produced are non-ideal or non-uniformly distributed lateral size and thickness. And the harsh synthetic process inevitably damages the graphene lattice.

Electrochemical exfoliation has been reported as an alternative top-down synthesis strategy to chemical exfoliation and is milder in comparison.<sup>30</sup> Electrochemical approaches usually use graphite rod or graphene sheets as bulk precursor for synthesis. These precursors are usually chosen for the convenience to use as an electrode to which a voltage can be applied to carry out the exfoliation process. The main drawback of electrochemical exfoliation using these bulk precursors is the long duration of synthesis. Intuitively, direct scissoring from defect-free graphene would ensure high-yield and high-quality of GQDs with a shorter duration of synthesis.

In this chapter, we report a facile, “green” and rapid synthesis strategy for high quality graphene quantum dots using a 3-dimensional free standing graphene as the precursor as well as electrode material (Figure 3.1). We also employ the as-synthesized GQDs for the specific detection of ferric ions in solution by a fluorescence turn-off mechanism.

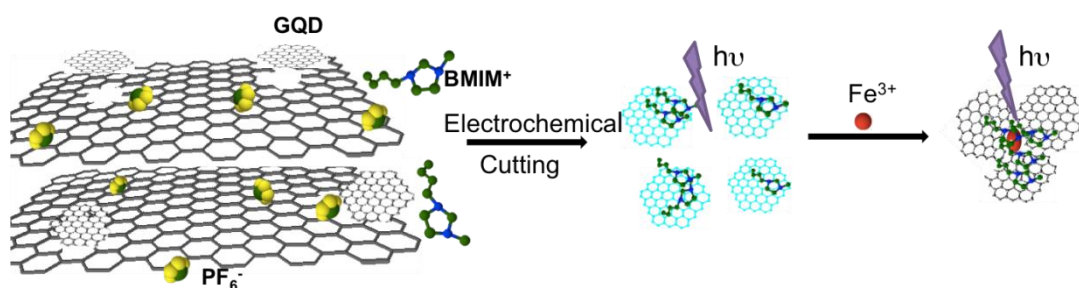


**Figure 3.1.** Schematic illustration of GQD synthesis from 3D graphene and mechanism of Fe<sup>3+</sup> detection.

### **3.1 Materials and Methods**

#### **3.1.1 Materials**

All chemicals were purchased from Sigma Aldrich (Singapore). Nickel foam was purchased from Alantum Advanced Technology Materials. Dialysis membranes were purchased from Spectra/Pro Biotec.

#### **3.1.2 3D graphene synthesis**

As previously reported, 3D graphene was synthesized by chemical vapour deposition (CVD)<sup>94</sup> using nickel foam as growth substrate and ethanol as the carbon source. Nickel foam was subsequently removed by heating in 3M HCl at 60 °C, leaving free-standing 3D graphene foam. After thorough rinsing with MilliQ water and drying in oven at 50 °C, 3D graphene (cut into 0.6 × 1 cm) was mounted onto a glass slide. Finally, an electrode is fabricated by making an electrical lead from one end of graphene substrate using silver paint and a copper wire (insulated by silicon rubber).

#### **3.1.3 GQD Synthesis**

Using 1-Butyl-3-methylimidazolium hexafluorophosphate (BMIMPF<sub>6</sub>) in acetonitrile (10%, v/v) as the electrolyte, a constant voltage or a cyclic voltage waveform was applied to 3D graphene using a CHI 660D electrochemical workstation (Chenhua) with a platinum wire as the counter electrode and an Ag/AgCl electrode as the reference. After the electrochemical exfoliation, the resultant GQD solution was centrifuged at 6000 rpm for 20 min to remove large particles, and then diluted with DI water (1/20, v/v). Acetonitrile was removed by rotary evaporator at 55° C. GQD solution was then dialyzed with cellulose ester dialysis membrane (MWCO 500-1000D) for 3 days to completely remove the electrolyte. Finally, GQD solution was ultra-filtrated by a centrifugal filter device with a molecular-weight-cut-off at 3000 Da.

#### ***3.1.4 Measurement of Magnetic Properties of Fe<sup>3+</sup>-induced GQD Aggregates***

Fe(NO<sub>3</sub>)<sub>3</sub> (4 mM) was added into GQD aqueous solution (0.325 mg/ml) to induce Fe<sup>3+</sup>-GQD complexation. The mixture was kept at room temperature for 2 hr and further dialysed with cellulose ester dialysis membrane (MWCO 500-1000D, Spectro/Pro Biotec) membrane for 24 hr. Different concentrations of the produced Fe<sup>3+</sup>-GQD complexes were embedded into a 1.6% agarose matrix in 24-well tissue culture plates. Pure GQD samples were used as control. For T1-weighted images the acquisition was done with different inversion times (TR= 2800 ms, TE= 8.5 ms, TI= 30, 50, 100, 200, 400, 500, 600, 800, 1000, 1200, 1800, 2000 and 2500 ms,) and T2 weighted images were acquired with different echo times (TR= 1000 ms, TE= 10, 15, 20, 40, 60, 80, 100, 150, 200 ms, slice thickness = 6.0 mm, matrix = 512 × 512, field of view = 27 cm). The values of T1 and T2 were calculated from the mean signal intensity of the MR images using MATLAB. T1 values were calculated by fitting the intensity data vs. inversion time using the inversion-recovery signal equation. The T2 values were calculated by fitting the intensities of T2 weighted images to a mono-exponential decay.

#### ***3.1.5 Characterization***

The surface properties of 3D graphene were characterized by field emission scanning electron microscopy (JSM6700-FESEM, JEOL). GQDs were inspected by atomic force microscopy (AFM) (MFP-3D AFM microscope, Asylum research) and high-resolution transmission electron microscope (HRTEM, JEOL 2010) at an accelerating voltage of 200 kV. Raman spectra were recorded using WITeCK CRM200 Raman System, with laser excitation wavelength of 514 nm. Fourier transform infrared spectroscopy (FTIR) and X-ray photoelectron spectroscopy (XPS) measurement were conducted with PerkinElmer Spectrum GX FTIR system and ESCALAB MK II X-ray photoelectron spectrometer, respectively. SDS-PAGE (12%) was conducted using Mino-Protean Tetra Cell (Bio-Rad)

to investigate the molecular weight distribution of prepared GQD sample. Spectra Multicolor Broad Range Protein Ladder (ThermoScientific) was employed as the molecular weight marker. The UV-vis absorption and photoluminescence spectrum of GQDs was characterized by UV-2450 spectrophotometer (Shimadzu) and LS-55 fluorescence spectrometer (PerkinElmer), respectively. Particle size of Fe<sup>3+</sup>-induced GQD aggregations was measured using Zetasizer (Malvern Instruments). For magnetic characterization, samples were scanned in a 3.0 Tesla whole body scanner (Magnetom Verio, Siemens) using a dedicated knee coil.

## **3.2 Results and Discussion**

### ***3.2.1 Synthesis mechanism***

The synthesized 3D graphene shows a monolithic macroporous structure (Figure 3.2a) of interconnected defect-free graphene network. It is pristine and single layered with few or no defects as evidenced by the intensity ratios of the G and 2D band and absence of D band in the Raman spectrum (Figure 3.2c). Electrochemical exfoliation has been reported for the etching of graphite rod into carbon nanoparticles and graphene nanoribbons.<sup>95</sup> In a similar procedure, we electrochemically incise the free-standing 3D graphene to produce GQDs, using room temperature ionic liquid (1-butyl-3-methylimidazolium hexafluorophosphate -- BMIMPF<sub>6</sub>) as the electrolyte dissolved in acetonitrile, which gives high ionic conductivity and wide electrochemical potential window.



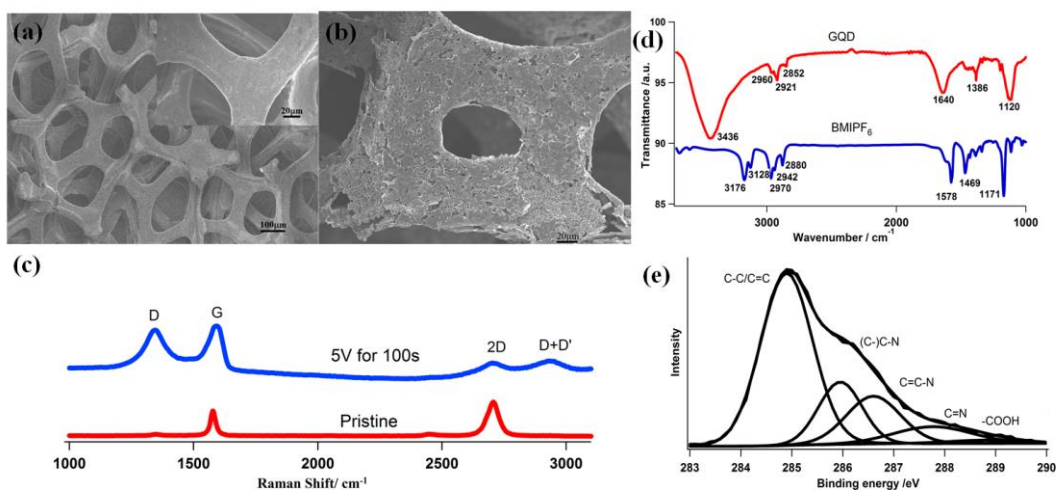


**Figure 3.2.** SEM images of 3D graphene (a) before and (b) after electrochemical treatment. The inset in (a) shows the surface of graphene skeleton at a higher magnification. (c) Raman spectra of 3D graphene before and after electrochemical treatment. (d) FTIR Spectra of GQDs and BMIMPF<sub>6</sub>. (e) XPS spectrum of GQDs.

After various attempts for optimizing the parameters for etching (Figure 3.3) we found that applying a constant voltage of 5V for 100s gives high yield of GQDs while achieving uniform etching of graphene foam and preserving its 3D structure. The etching process can be observed by the rapid flaking off of the 3D graphene electrode into the electrolyte solution that turns progressively from pale yellow to brown. The etching renders the graphene electrode with pinholes and structural and chemical defects that are confirmed by SEM images (Figure 3.2b) and Raman spectroscopy (Figure 3.2c) respectively. From the results we speculate the mechanisms underlying the exfoliation process to be governed by three factors namely; 1) high electrical stress by the applied voltage; 2) the ability of PF<sub>6</sub><sup>-</sup> to intercalate between the graphene layers<sup>95</sup>; 3) intimate interaction ( $\pi$ - $\pi$  or cation- $\pi$  interaction) between BMIM<sup>+</sup> group and GQD.<sup>95</sup>

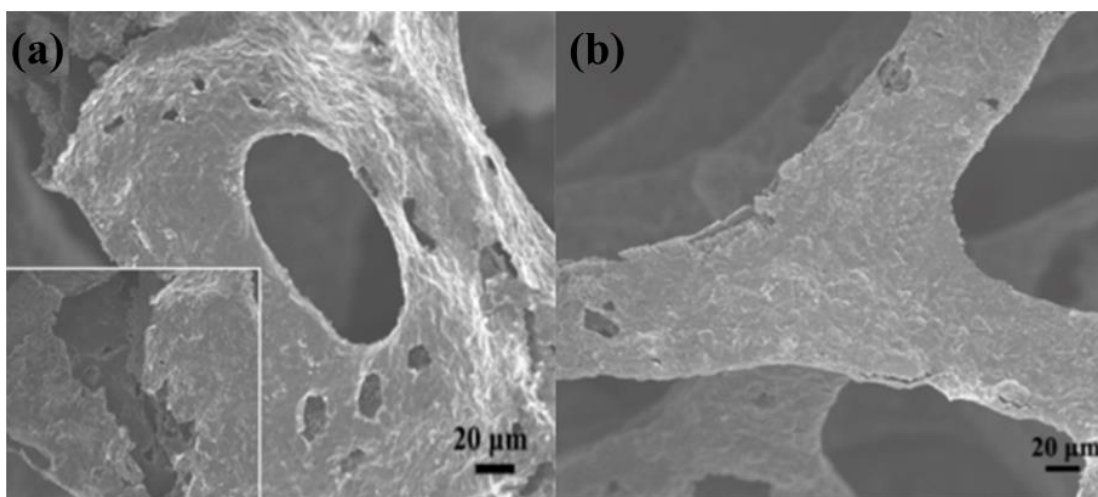


**Figure 3.3** SEM images of 3D graphene after (a) electrochemical etching with 100 voltammetric cycles ( $\pm 3V$ ) and (b) electrochemical etching with a constant voltage of 3V for 300s. The former protocol leads to collapse of graphene foam while the later gives low-yield of GQD production.

### 3.2.2 Chemical characterization

From the FTIR spectroscopy, it can be observed that the obtained GQDs show characteristic peaks of C-H asymmetric and symmetric vibration at 2960, 2921 and 2852  $\text{cm}^{-1}$  (Figure 3.2d).<sup>96, 97</sup> In addition, (XPS) demonstrates several characteristic peaks corresponding to the binding energies of C-C/C=C, and N-C=N, (C-)C-N bonds, in addition to the prominent C-C/C=C peak (Figure 3.2e). This observation confirms the hybridization between GQD and  $\text{BMIM}^+$ . We also found that, comparing to other ionic liquids (including 1-Butyl 3-Methyl Imidazolium chloride --  $\text{BMIMCl}$ , tetra ethyl ammonium chloride –  $\text{TEAC}$ ),  $\text{BMIMPF}_6$  gives the highest yield, confirming the facilitating role of  $\text{PF}_6^-$  in cleavage.  $\text{BMIM}^+$ , on the other hand, assists to disperse GQDs in both, organic solvents and water due to its amphiphilic property. The GQD dispersions are highly stable (no obvious aggregation observed for months).

### ***3.2.3 Morphological Characterization***

Gel electrophoresis (SDS-PAGE) data indicates the narrow size distribution of GQDs resulting in a single band with size lower than 10kDa (Figure 3.4a). From AFM measurements it can be observed that the average thickness of GQDs is ~1.25 nm, indicating that they are mostly single-layered (note that the attached BMIM<sup>+</sup> groups contribute to the measured thickness) (Figure 3.4b and c). The average lateral dimensions of the GQDs were found to be 3.0 nm with a narrow size distribution (Figure 3.4 d, e and f) as revealed by the TEM measurements. The graphitic lattice of GQD can be clearly resolved under high-resolution TEM (Figure 3.4e). The observed two kinds of lattice spacing (2.10 Å and 2.45 Å) correspond to the hexagonal lattice plane spacing of  $d_{1100}$ <sup>98</sup> and  $d_{1120}$ <sup>99</sup>, respectively. These measurements prove that the produced GQDs are uniform and of high crystallinity.

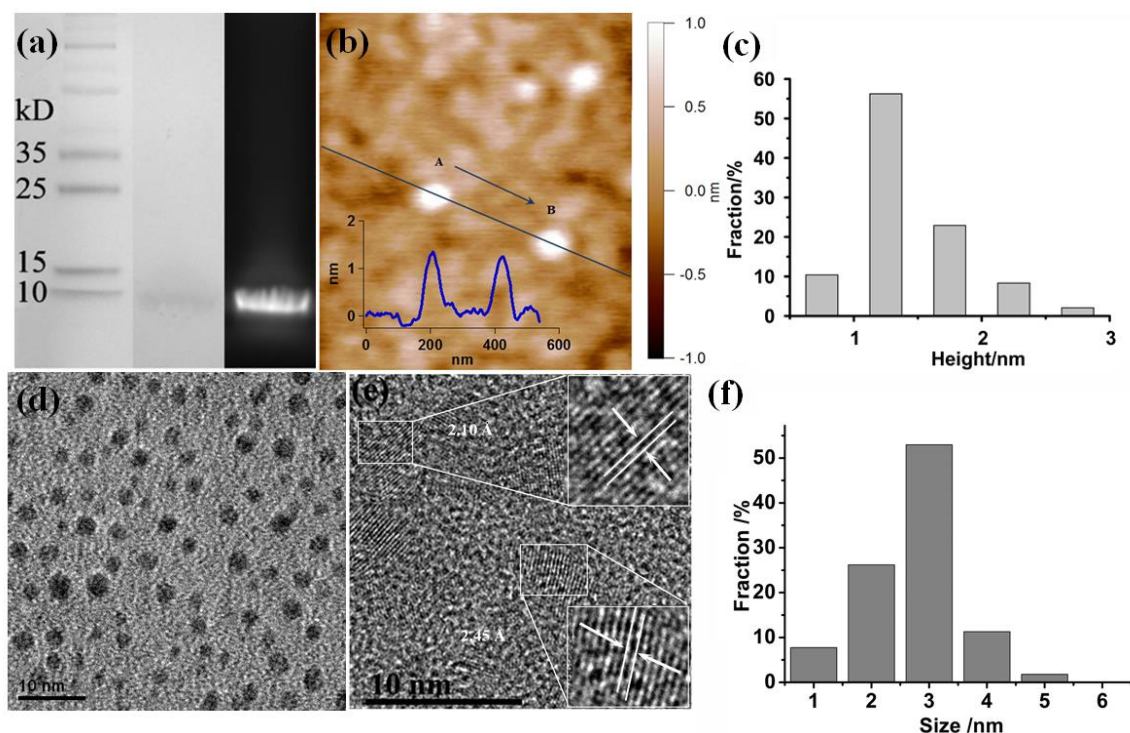


**Figure 3.4.** (a) Electrophoresis gel image of GQD samples. (b) AFM image and height profile (inset) of GQDs. (c) Height distribution obtained from AFM measurements (203 samples). (d) and (e) TEM images of GQDs. The insets show the lattice spacing of GQDs. (f) Diameter distribution obtained from TEM images (166 samples).

### 3.2.4 Optical Characterization

The dispersion of GQDs in water appears light-brown under white light and emits blue fluorescence under UV (365 nm) (Figure 3.5a, inset). Similar to the GQDs prepared by other methods, higher absorption in the UV range is observed (Figure 3.5a).  $\pi$ - $\pi^*$  transition of aromatic  $sp^2$  domains is reported to be responsible for the strong UV absorption below 300 nm.<sup>19</sup> The excitation spectrum exhibits two peaks (at 243 nm and 360 nm) corresponding to  $\sigma$ - $\pi$  and  $\pi$ - $\pi^*$  transitions originated from the carbene like triplet state of the zig-zag edges of GQDs (Figure 3.5a)<sup>100</sup>. Like commonly reported GQDs, our GQDs also demonstrate excitation dependent emission (Figure 3.5b). The maximum emission intensity of GQDs is observed at 440 nm when excited at 360 nm. A quantum yield of about 10% at pH 7 is calculated using quinine sulfate as the reference,

which is higher than that of the previously reported GQDs electrochemically exfoliated from graphite.<sup>100, 101</sup>

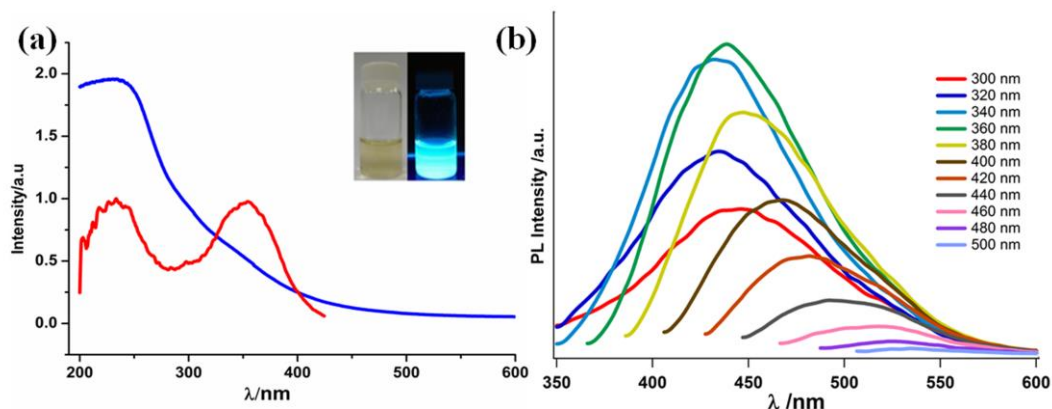


**Figure 3.5.** (a) UV-vis absorption (blue) and excitation (red) spectra of GQDs. The inset shows the photographs of aqueous dispersions of GQDs under day light (left) and UV (365 nm) illumination (right). (b) PL spectra of GQD solution under different excitation wavelength

### 3.2.5 Optical detection of ferric ions

As our GQDs were functionalized with BMIM<sup>+</sup> we speculated they can be used as optical sensors. It is known that the nitrogen groups on the imidazole ring of BMIM<sup>+</sup> has a high binding affinity to ferric ions (Fe<sup>3+</sup>) therefore addition of Fe<sup>3+</sup> would result in GQD aggregation.<sup>102</sup> Detection of Fe<sup>3+</sup> ions is important as they play important roles in biological systems by complexation with various regulatory proteins<sup>103</sup>. On the other hand, excess Fe<sup>3+</sup> ions can lead to over-production of free radicals resulting in DNA damage and cell death. High Fe<sup>3+</sup> concentration in neurons is also a key marker for Parkinson's disease and Alzheimer's disease.<sup>103</sup> Ferric ion concentration of 0.9 mM have been found in amyloid plaques in Alzheimer's disease.<sup>104</sup> Excessive Fe<sup>3+</sup> concentration is also relevant to environmental pollution where the maximum permissible limits of dissolved iron concentration is 300μM (USEPA).

GQDs fluoresce well over a wide pH range. But GQD fluorescence decreases with increasing pH because high pH possibly attenuates GQD's interaction with BMIM<sup>+</sup>

whose pyridinic nitrogen can enhance the fluorescence by imposing n-doping like characteristics to GQD (Figure 3.6a).<sup>27</sup> Also as shown in Figure 3.6a, the presence of  $\text{Fe}^{3+}$  ions (200  $\mu\text{M}$ ) causes significant quenching of GQD fluorescence. And the quenching is most prominent at pH 4 (Figure 3.6a), which is thus chosen for the following experiments. It is conceivable that  $\text{Fe}^{3+}$  ion acts as a coordinating center to bridge several  $\text{BMIM}^+$ -functionalized GQDs together and quenching occurs from the induced aggregation of GQDs (Figure 3.1).<sup>105</sup> Furthermore, the fluorescence quenching of GQDs is highly selective to  $\text{Fe}^{3+}$  (68% quenching upon addition of 400  $\mu\text{M}$   $\text{Fe}^{3+}$ ) while other metal ions ( $\text{Mg}^{2+}$ ,  $\text{Fe}^{2+}$ ,  $\text{Zn}^{2+}$ ,  $\text{Co}^{2+}$ ,  $\text{Ni}^{2+}$ ,  $\text{Cd}^{2+}$  and  $\text{K}^+$ ) are not able to exert significant quenching effect (Figure 3.6b). As shown in Figure 3.6c, the fluorescence quenching by  $\text{Fe}^{3+}$  is dose dependent. And the response spans over a wide concentration range with a theoretical lower detection limit of  $\sim 7.22 \mu\text{M}$  ( $= 3\sigma / m$  where  $\sigma$  is the standard deviation,  $m$  is the slope of the linear response region at low concentrations less than 80  $\mu\text{M}$ ) (Figure 3.6d).

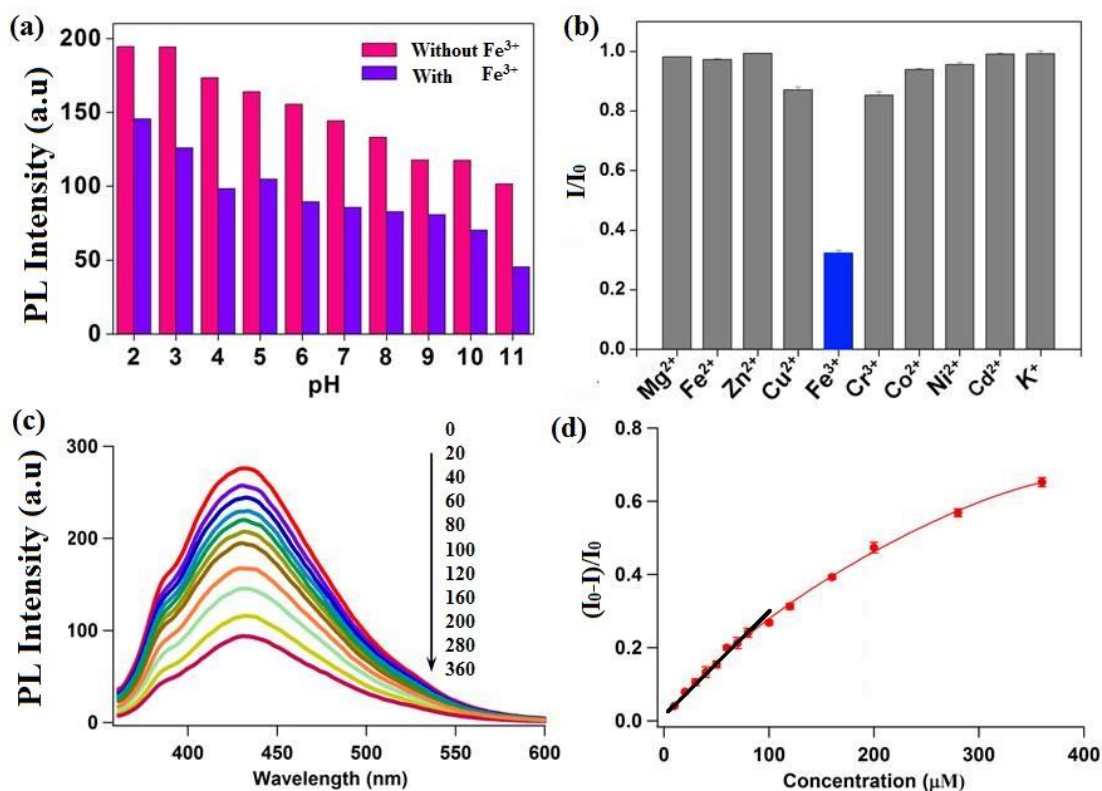


**Figure 3.6** (a) PL of GQDs (50 μg/mL) in the absence (red) and presence (purple) of 200 μM Fe<sup>3+</sup> at different pH. (b) Remaining percentage of GQD PL after addition of different metal ions (400 μM) in acetate buffer solution (pH 4.0). (c) Emission spectra of GQDs in the presence of Fe<sup>3+</sup> ions at increasing concentrations (μM). (d) Average concentration-dependent fluorescence response in the acetate buffer solution. The error bars indicate the standard deviations (n = 3). Linear fitting is performed in the low concentration range (black line).

### 3.2.6 Properties of Fe<sup>3+</sup> induced aggregates

Fe<sup>3+</sup> induced aggregation of GQDs is confirmed by AFM measurements (Figure 3.7) and particle size measurement based on dynamic light scattering. GQD aggregates are few-layered and  $10.425 \pm 4.275$  nm in diameter. We speculated that such small Fe<sup>3+</sup>-containing particles may serve as contrast agents for magnetic resonance imaging (MRI). As shown in Table 1, these particles indeed exhibit good magnetic response as evidenced



by much lowered spin-spin relaxation time ( $T_2$ ) as compared to the pure GQD samples at the same concentration.

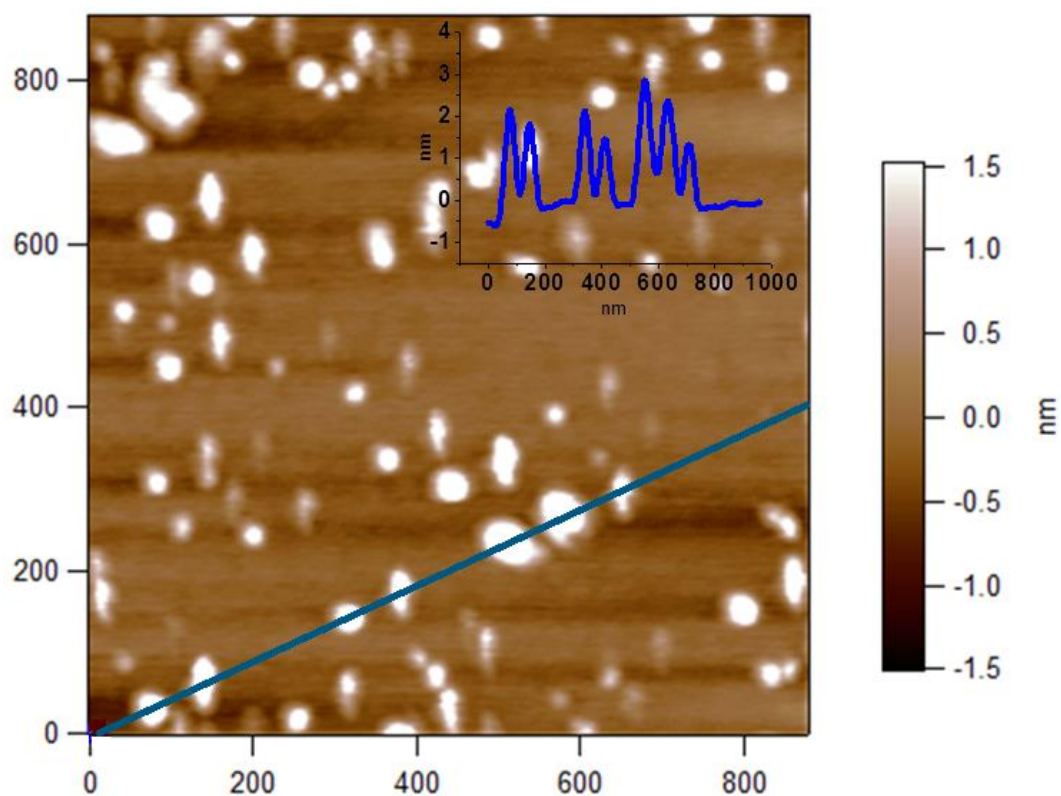


**Figure 3.7** AFM image of  $\text{Fe}^{3+}$ -GQD complexes



| Concentration of Fe <sup>3+</sup> (mM) | Concentration of GQDs (mg/ml) | 1/T1      | 1/T2     |
|--|-------------------------------|-----------|----------|
| 1.28                                   | 0.1625                        | 0.0006604 | 0.01147  |
| 0.64                                   | 0.08125                       | 0.0006447 | 0.008394 |
| 0.32                                   | 0.0406                        | 0.0006192 | 0.008172 |
| 0.16                                   | 0.0203                        | 0.0006032 | 0.007199 |
| 0.08                                   | 0.01                          | 0.0005988 | 0.008232 |
| 0.04                                   | 0.005                         | 0.0006125 | 0.007401 |
| 0                                      | 0.1625                        | 0.0006023 | 0.002749 |
| 0                                      | 0.08125                       | 0.0006036 | 0.00453  |
| 0                                      | 0.0406                        | 0.0005751 | 0.004199 |
| 0                                      | 0.0203                        | 0.0005583 | 0.004911 |
| 0                                      | 0.01                          | 0.0005604 | 0.006326 |
| 0                                      | 0.005                         | 0.0005711 | 0.006544 |

**Table 1** Comparison of different relaxation times of Fe<sup>3+</sup>-induced GQD aggregates to that of control (GQD) samples.

### 3.3 Conclusions

In summary, we have developed a highly efficient and “green” electrochemical strategy to synthesize GQDs from 3D CVD-graphene with high throughput. The synthesized GQDs are of high crystallinity and uniform distribution in lateral diameter (~3 nm) and thickness. The ionic liquid used in the synthetic process not only assists in exfoliation and dispersion of GQDs but also endows GQDs with the ability for sensitive and specific optical detection of Fe<sup>3+</sup> ions. In addition, the magnetic property of the Fe<sup>3+</sup>-induced GQD aggregates may promise other applications (e.g., for MRI imaging). We also envision that the versatility of this synthesis approach permits synthesis of GQDs with tailored functionalities by varying the used solvent or electrolyte and tuning the etching

protocol. This development would pave the way for the widespread applications of such emerging zero-dimensional materials in various fields.

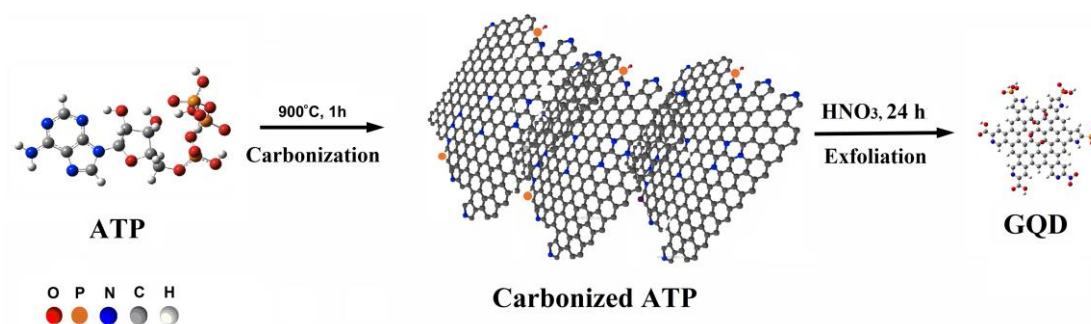
This chapter (including phrases and figures) is reproduced with permission from our published article “Facile synthesis of graphene quantum dots from 3D graphene and their application for Fe<sup>3+</sup> sensing. *Adv. Funct. Mater.*, 2014, 24, 3021.” Copyright 2014, Wiley VcH.

## **Chapter 4 Nitrogen and Phosphorus co-doped Graphene**

### **Quantum Dots: Synthesis from Adenosine Triphosphate, Optical Properties, and Cellular Imaging**

Owing to their tunable photoluminescence (PL), photostability, molecular size, biocompatibility, and ease to be conjugated with biomolecules, GQDs are particularly attractive fluorescent tools for bioimaging.<sup>13, 35, 39, 70, 106-112</sup> It has been shown that heteroatom doping endows GQDs with new PL properties due to the change in electron density around the graphene lattice.<sup>112-114</sup> Heteroatom-doped GQDs can be synthesized by exfoliating pre-doped graphene or graphene oxide sheets.<sup>28, 54, 55, 115</sup> But such top-down methods require multiple steps for synthesis as well as purification of multiple steps and are usually of low doping efficiency. Alternatively, doped GQDs can be obtained by pyrolyzing small organic molecules, with a combination of two or more precursors molecules, heteroatoms doped GQDs have been synthesized. The heteroatoms are naturally incorporated into the graphene lattice from the precursor molecules.<sup>4, 56, 116, 117</sup> However, co-doping of multiple heteroatoms has been rarely reported and their effects on GQD fluorescence still remain undiscovered.

In this chapter we report a simple and cost-effective method for the synthesis of GQDs co-doped with nitrogen, and phosphorus by carbonization and subsequent chemical exfoliation of a single precursor molecule - adenosine triphosphate (ATP) (Scheme 1). The dually-doped GQDs show high quantum yield (~27.5%) and strong two-photon excitation with a two-photon absorption cross section (20000 GM). Carbonaceous micro-sheets resulted from ATP carbonization exhibits good catalytic properties towards oxygen reduction. Upon conjugation with transferrin, heteroatom-doped GQDs have been employed to image and track transferrin receptors in live cells.



**Scheme 4.1** Illustration of the synthesis procedure for ATP-GQDs

## 4.1 Materials and Methods

### 4.1.1 Synthesis of ATP-GQDs

ATP powder (1g, Acros Organics) was completely carbonized by heating in a quartz tube furnace at 900°C for 1h under argon atmosphere. The obtained carbonaceous powder was further refluxed in 6M HNO<sub>3</sub> at 130°C for 24h. The solution was then cooled and centrifuged at 7500Xg for 20 min. The supernatant was collected and filtered through filter paper to remove large particles. The excess HNO<sub>3</sub> was removed by evaporation at 200°C. The resulting powder was subsequently dissolved in DI water and dialyzed using a cellulose ester dialysis membrane (500-1000 Da MWCO, Spectra/Pro Biotec) for 2 days to remove impurities.

### 4.1.2 Oxygen reduction reaction (ORR)

The carbonized ATP samples were washed with DI water by centrifugation at 10000 rpm 6 times to remove ions or other impurities and dried at 50°C in a hot air oven. Carbonized ATP dispersion (2 mg/ml) was drop-casted onto a polished glassy carbon electrode. The ORR measurements were conducted with a CHI 660D electrochemical workstation (Chenhua), using nitrogen or oxygen saturated KOH (0.1 M) solution as the electrolyte.

#### ***4.1.3 Transferrin conjugation***

Transferrin (Sigma Aldrich) was conjugated to ATP-GQDs according to a previously reported procedure.<sup>70</sup> Briefly, the ATP-GQD solution was filtered by a 10 kDa MWCO filter device (Millipore) and the fraction <10 kDa (0.5 mg/ml in PBS) was mixed with 1-ethyl-3-(3-dimethylaminopropyl) carbodiimide hydrochloride (10 mM) followed by N-hydroxysuccinimide (10 mM) and the mixture was kept at room temperature for 15 min for carboxyl group activation. Transferrin (~80 kDa, Sigma) was added to the activated ATP-GQDs and incubated at room temperature for 4 h. Finally, hydroxylamine (10 mM) was added to quench the reaction. The unreacted GQDs were separated by ultrafiltration (3 times) with 30 kDa MWCO ultracentrifugal filters.

#### ***4.1.4 Characterizations***

Samples were characterized by Raman spectroscopy (WITeCK CRM200), field-emission scanning electron microscopy (JSM6700-FESEM, JEOL), AFM (MFP-3D AFM, Asylum research), high-resolution transmission-electron microscopy (JEOL-2010), FTIR (PerkinElmer Spectrum GX FTIR system), XPS (Theta Probe), X-ray diffraction analysis (Bruker D8 Advanced Diffraction meter using Cu K $\alpha$  radiation), UV-vis absorption spectroscopy (UV-2450 spectrophotometer, Shimadzu), photoluminescence spectroscopy (LS-55 fluorescence spectrometer, PerkinElmer) and polyacrylamide gel electrophoresis and imaging (Mini-Protean Tetra Cell, Bio-Rad and ProXPRESS 2D, Perkin Elmer). The two-photon excited PL properties at 800 nm excitation were investigated using a femtosecond amplified-pulsed laser with repetition rate of 1000 Hz and pulse-width of 100 fs.<sup>118</sup> The lifetime measurements were carried out for the one and two-photon excitation by an Optronics streak camera system.<sup>119</sup>

#### ***4.1.5 Cell Imaging***

Human cervical cancer cells (HeLa, ATCC) were cultured in Dulbeccos modified eagle medium (DMEM) containing 10% Fetal bovine serum (Gibco). For the imaging experiments, HeLa cells were seeded on a Lab-Tek II chambered cover glass and grown overnight. Prior to imaging, the cells were incubated with ATP-GQDs for 2 h or Tr-GQDs for 30 min at 37°C. The cells were rinsed thrice and incubated in the bath solution (150 mM NaCl, 5 mM KCl, 1.1 mM MgCl<sub>2</sub>, 2.6 mM CaCl<sub>2</sub>, 10 mM HEPES, and 10 mM glucose, pH 7.4) during imaging. Confocal microscope (Zeiss LSM 510) with a 63X oil objective and a 488 nm laser was used to obtain the confocal images. Time-lapse digital images were recorded using a Zeiss Axiovert-200M inverted total-internal-reflection fluorescence microscope system (Carl Zeiss, Germany) equipped with a 100x objective lens (numerical aperture, NA=1.45) and a charge coupled device (CCD) camera with pixel size of 0.248  $\mu$ m. Using MetaMorph 6.3 (Universal Imaging Corp., Downingtown, PA), time-lapse images of 361 frames (0.5 s/frame) were acquired at 37°C, and analyzed using ImageJ (National Institute of Health, US).

### **4.2 Results and Discussion**

#### ***4.2.1 Properties of carbonized ATP***

Adenosine triphosphate (ATP) is a good substrate for carbonization at it contains sugar moieties and  $\pi$  conjugated carbon rings with nitrogen. Complete carbonization of ATP molecules yields carbonaceous micro-sheets abundant in heteroatoms (Figure 4.1a), resulting from removal of water molecules and subsequent re-organization and fusion of the precursor molecules at high temperature. From the Raman spectrum of the carbonized ATP (cATP) it can be observed that cATP shows prominent D and G bands (Figure 4.1b), suggesting the presence of graphitic domains with the presence both C=C bond and also covalent bond with heteroatoms. As reported earlier, heteroatom doping confers the inert graphene or graphitic materials with catalytic abilities such as oxygen reduction.<sup>113, 120</sup>

Similarly, we tested the cATP for activity towards oxygen reduction reaction. From our experiments it can be seen that cATP exhibits good catalytic activity towards oxygen reduction (ORR) as evidenced by the prominent reduction peak at  $\sim -0.26$  V in the presence of oxygen (Figure 4.1c). Linear sweep voltammograms of cATP in oxygen-saturated 0.1M KOH obtained using a rotating disk electrode at various rotating speeds help to determine the number of electrons transferred for the ORR process (Figure 4.1d). Koutecky–Levich (K–L) plots at different potentials are plotted in Figure 4.1d inset. From the slopes of the K–L curves we calculate the number of electrons involved in the ORR and find that a highly efficient 4-electron reduction pathway catalyzes the ORR in cATP. The onset potential is also found to be around 0.14 V, which is desirably lower than the previously reported N-doped graphene.<sup>121-124</sup> This experiment confirms the presence of heteroatoms that render cATP with catalytic properties.

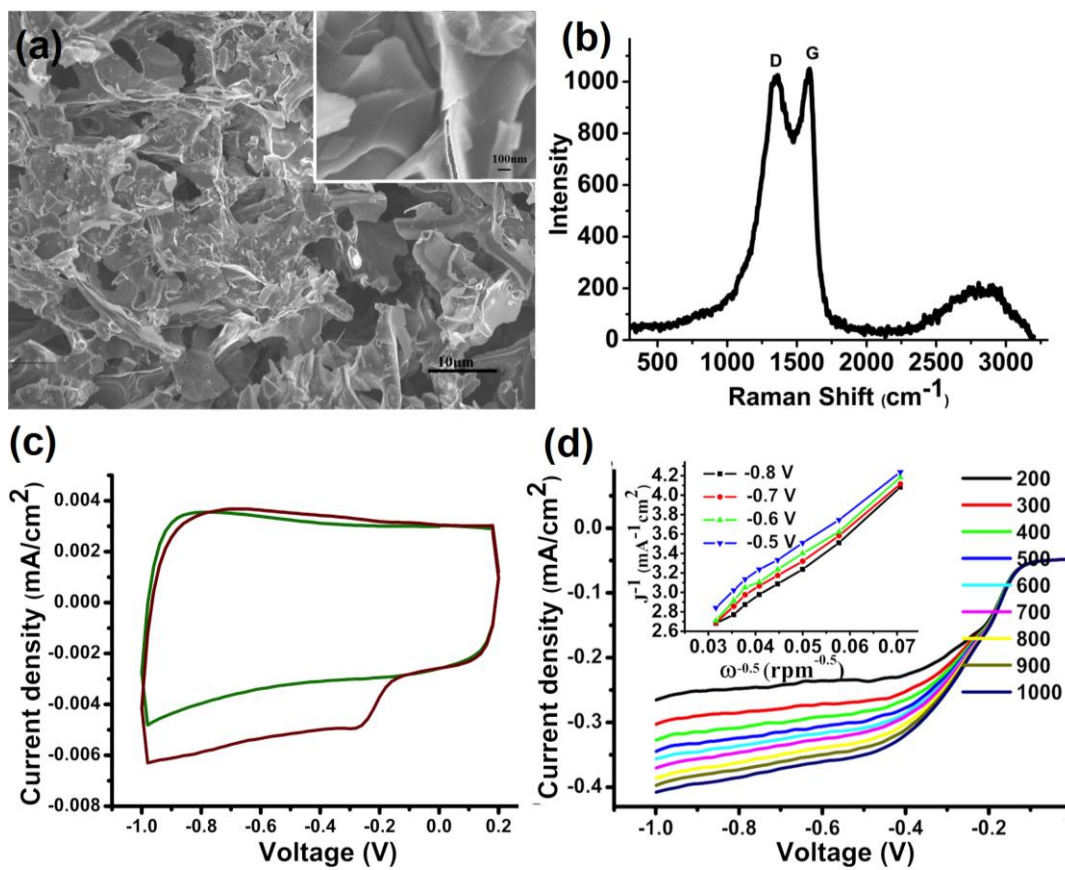


**Figure 4.1** a) SEM images of carbonized ATP (cATP). The inset shows the surface of cATP sheets at higher magnification. b) Raman spectrum of carbonized ATP. c) Cyclic voltammograms of cATP in oxygen (red) or nitrogen (green) saturated KOH (0.1 M) solution. d) Linear-sweep voltammetry curves of cATP in 0.1 M KOH at different rotation speeds. The Koutecky-Levich plots at different potentials (the slopes of the curves indicate the electron transfer number of 4.2 - 4.4) are shown in inset.

#### 4.2.2 Morphological characterization of GQDs

cATP is further exfoliated by refluxing in nitric acid to yield a brown water soluble dispersion. The results from transmission electron microscopy (TEM) show that carbon nanosheets  $\sim 2.06 (\pm 0.69, n = 161)$  in diameter have been produced (Figure 4.2a & b). A lattice spacing of 0.24 nm is also observed from the high-resolution TEM image. The spacing corresponds to the d1120 plane of graphene (Figure 4.2a inset) thereby verifying the synthesized carbonaceous dots are GQDs.<sup>99</sup> The small sizes of GQDs have also been confirmed by gel electrophoresis where a narrow band ( $\ll 10$  kDa) is observed (Figure 4.2c). AFM characterization reveals that the average thickness of these GQDs is  $\sim 1.26$



nm ( $\pm 0.66$ ,  $n = 231$ ) corresponding to 1-3 layers of graphitic carbon (Figure 4.2b & c). These observations demonstrate that cATP exfoliation yields a nearly homogenous dispersion of GQDs.

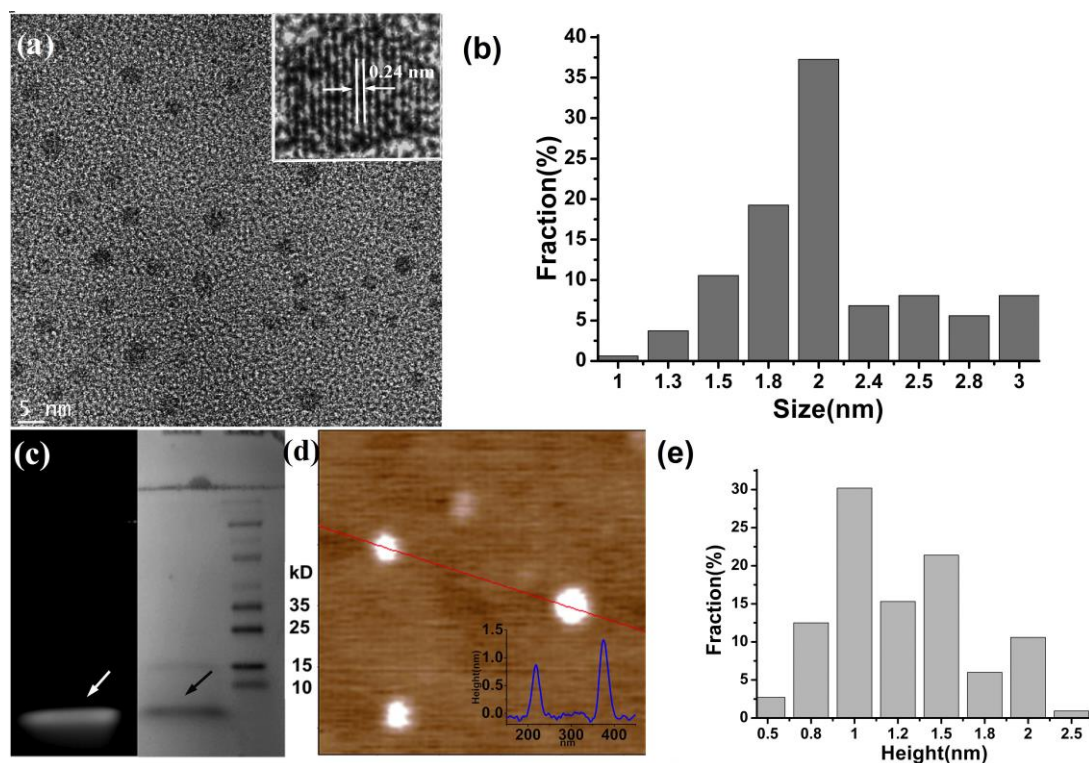


**Figure 4.2** a) TEM image of ATP-GQDs. The HR-TEM image in inset reveals the lattice spacing. b) Size distribution histogram from TEM images (161 samples). c) Gel electrophoresis image of ATP-GQD samples (left: excitation at 488 nm; right: bright view). (d) AFM image of GQDs with the height profile along the indicated line shown in inset. (e) Height distribution obtained from 213 samples.

#### 4.2.3 Chemical characterization of GQDs

From the FTIR spectroscopy characteristic peaks for C=O ( $1722\text{ cm}^{-1}$ ), C=C ( $1629\text{ cm}^{-1}$ ), OH ( $3414\text{ cm}^{-1}$ ), -COOH ( $1388\text{ cm}^{-1}$ ), P-O ( $966\text{ cm}^{-1}$ ) and CH<sub>2</sub> ( $2922\text{ cm}^{-1}$ ) (Figure 4.3a) are revealed. XPS is conducted to understand the type of doping in the ATP-GQDs, the high resolution C<sup>1s</sup> spectrum of GQDs can be well-fitted with the characteristic peaks for C=C bonds ( $284.2\text{ eV}$ ),<sup>101</sup> C-N/ C-P=O ( $285.1\text{ eV}$ ),<sup>125, 126</sup> C-O ( $286.3\text{ eV}$ )<sup>127</sup> and O-C=O ( $288.2\text{ eV}$ )<sup>126</sup> (Figure 4.3b). It correlates well with the FTIR results. The N<sup>1s</sup> spectrum consists of three peaks at  $399.3$ ,  $400.5$  and  $405.1\text{ eV}$ , corresponding to the pyridinic,<sup>128</sup>

pyrrolic,<sup>128</sup> and NO<sub>2</sub> groups, respectively (Figure 4.3c). The NO<sub>2</sub> groups are likely introduced at the edges during the exfoliation with HNO<sub>3</sub>. Analysis of the P<sup>2p</sup> XPS spectrum gives two peaks at 132.6 eV and 133.5 eV (Figure 4.3d), which can be assigned to P-O and P-C bond.<sup>129, 130</sup> Likely, these bonds belong to phosphonic acid groups (-PO<sub>3</sub>H<sub>2</sub>) at the edges because incorporation of P in the graphene lattice would introduce unstable structural distortion due to the longer length of P-C bond than that of C-C bond.<sup>131</sup> As reported by XPS, the doping percentage of nitrogen and phosphorous are 6.2 (C/N ratio of 7.0) and 6.9 (C/P ratio of 6.3), respectively. Evidently, ATP-GQDs are doped with both N and P atoms. The N-doping level here is higher than the previously reported N-/B- co-doped GQDs.<sup>57</sup>

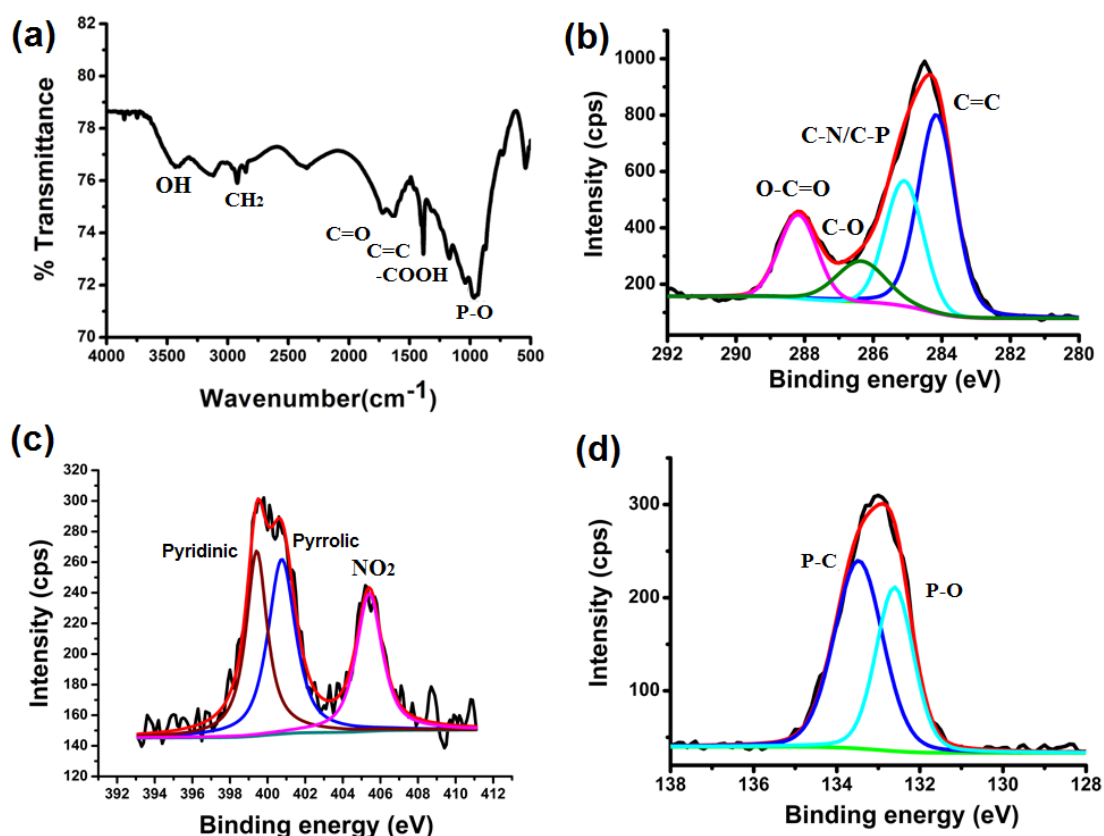


**Figure 4.3.** a) FTIR spectrum of ATP-GQDs. (b, c, d) High resolution XPS spectra for C<sup>1s</sup>, N<sup>1s</sup>, and P<sup>2p</sup>.

The interlayer spacing of ATP-GQDs analyzed by X-ray diffraction (XRD) is ~0.36 nm (Figure 4.4a), slightly higher than the spacing of graphite (0.34 nm) due to the presence of

chemical groups. The Raman spectrum of ATP-GQD is similar to that of cATP (Figure 4.4b).

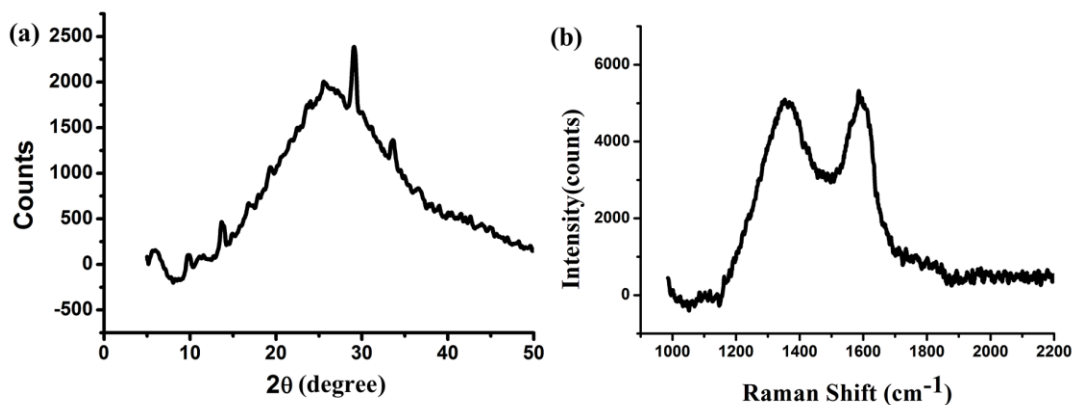


**Figure 4.4** (a) XRD and (b) Raman spectrum of ATP-GQDs.

#### 4.2.4 Optical characterization of GQDs

The colloidal dispersion of ATP-GQDs in water appears brown under bright light and a green emission is observed on illumination with 365 nm UV lamp (Figure 4.5a, inset). From the UV-Vis spectrum, it can be seen that, ATP-GQDs can more efficiently absorb short-wavelengths due to  $\pi$ - $\pi^*$  transitions of the aromatic  $sp^2$  domains in the graphene lattice<sup>101</sup> and the absorption extends to the visible regime (Figure 4.5a). The PL excitation spectrum shows a prominent peak at 460 nm and a shoulder peak at 360 nm which is due to the  $\sigma$  -  $\pi$  and  $\pi$ - $\pi^*$  transitions originated from the carbene like triplet state of the zig-zag edges of GQDs (Figure 4.5a).<sup>43</sup>

The PL spectra of ATP-GQDs exhibit a slight excitation dependent emission with maximum emission at 520 nm when excited at 460 nm (Figure 4.5b). This result is in contrast to most of the reported GQDs.<sup>132</sup> A uniform size and chemical composition of GQDs could possibly explain this behaviour.<sup>114</sup> The quantum yield (QY) is calculated to be ~27.5% using rhodamine 6G (QY 96%) as the reference, which is much higher than the non-doped GQDs.<sup>35</sup> The improved QY could be attributable to the interplay of the different dopants in the graphene lattice. It has been proposed that coexistence of n- and

p-dopants can increase QY due to formation of p-n type photochemical diodes.<sup>81</sup> In ATP-GQD, pyridinic and pyrrolic N atoms are strongly electron withdrawing conferring p-type doping characteristics.<sup>133</sup> The electron-withdrawing  $-\text{PO}_3\text{H}_2$  groups impose p-doping effects.<sup>134</sup> Additionally, the presence of oxygenated groups at the edges also give rise to either weak n- (e.g.,  $-\text{OH}$ ) or p- (e.g.,  $-\text{COOH}$ ) doping effects.<sup>81</sup>

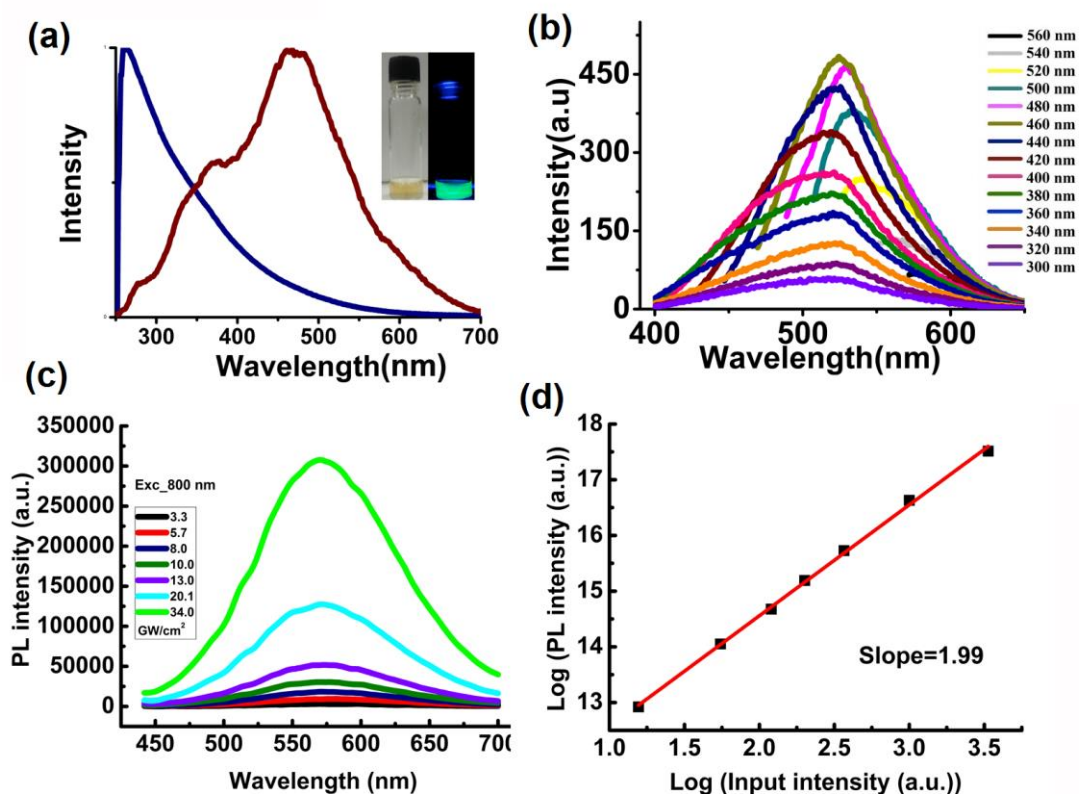


**Figure 4.5.** a) UV-Vis absorption (blue) and excitation (red) spectra of GQDs. The inset shows the optical image of aqueous solution of ATP-GQDs under visible (left) and UV light (right, 365 nm). (b) PL spectra of GQDs at different excitation wavelengths. (c) Laser power dependent emission spectra of ATP-GQDs under two-photon excitation using a femtosecond pulsed laser (800 nm). (d) Quadratic relation between excitation intensity and PL intensity with a fitting (red line).

It is known that oxygenated groups on GQDs compromise QY because of non-radiative recombination at these sites.<sup>135</sup> Consistently, we show that chemical reduction of ATP-GQDs using  $\text{NaBH}_4$  can largely increase QY to 53%, and at the same time, blue-shift the emission peak to ~475 nm (Figure 4.6a). But the emission spectrum is broadened,

presumably due to increased chemical heterogeneity after reduction. In addition, removing oxygenated groups makes GQDs more prone to aggregation and more difficult to be conjugated with biomolecules. Therefore, in the later bio imaging experiments, we use as-prepared ATP-GQDs without reduction.

Furthermore, we examined the two-photon absorption properties of ATP-GQDs as two-photon fluorescence microscopy has advantageous over normal one-photon fluorescence microscopy in terms of larger penetration depth amenable for tissue imaging, higher spatial resolution and lower background signal due to highly non-linear and localized adsorption process.<sup>136</sup> Interestingly, ATP-GQD also exhibits good two-photon excitation properties. Under the excitation at 800 nm, which is far away from the one-photon absorption regime of GQD, strong upconverted PL is observed with emission maximum at ~560 nm (Figure 4.5c). The quadratic dependence of PL signal on the excitation intensity confirms the nonlinear two-photon absorption and emission process (Figure 4.5d).<sup>86</sup> The Z-scan technique is employed to estimate the two-photon absorption cross-section ( $\sigma$ ) of our ATP-GQDs (Figure 4.6b). The nonlinear absorption signal of the ATP-GQDs can be well-fitted by the Z-scan theory,<sup>86, 118</sup> giving a  $\sigma$  as high as ~20000 GM. This value is two-orders higher than organic fluorophores<sup>137</sup> and comparable to much larger-sized CdSe quantum dots.<sup>138</sup>

It has been observed that two-photon absorption cross-section of quadrupolar molecules increases due to co-existence of electron withdrawing and donating groups which facilitates intramolecular charge transfer.<sup>139</sup> Theoretical study also suggests non-linear emission from GQDs could arise when electron-withdrawing NO<sub>2</sub> and electron-donating NH<sub>2</sub> groups at the edges forms a donor-GQD-acceptor system.<sup>140</sup> Liu et. al. have demonstrated that dimethyl amine functionalized GQD shows strong two-photon absorption and attributed this to the electron-donating nature of the dimethyl amine groups.<sup>111</sup> Hence conceivably, the co-existence of electron withdrawing and donating

sites (which can form p-n type photochemical diodes) in heteroatom-doped ATP-GQD leads to its good two-photon absorption properties.

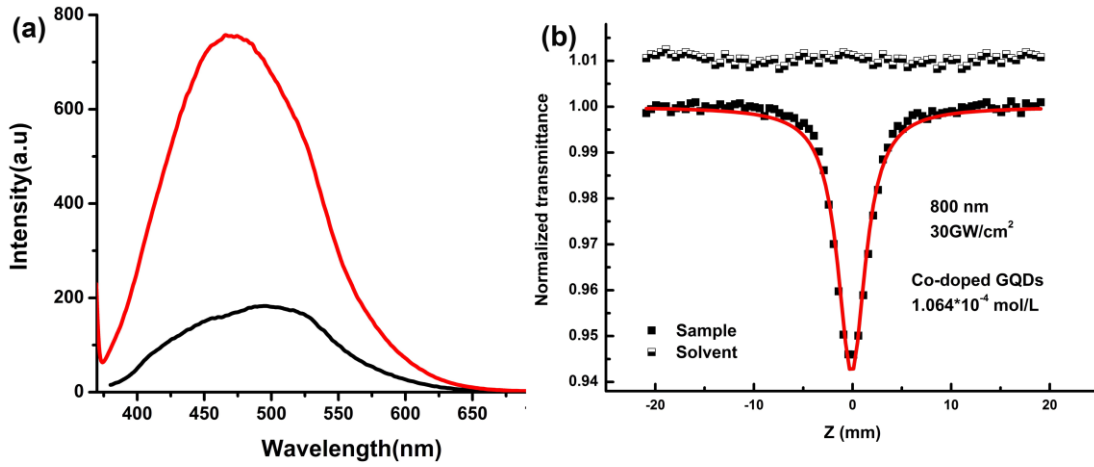


**Figure 4.6** (a) PL spectra of ATP-GQDs before (black) and after (red) chemical reduction. (b) Z-scan of ATP-GQDs and water (solvent control).

#### 4.2.6 PL lifetime and photostability of GQDs

ATP-GQD demonstrates excellent photostability under continuous one-photon or two-photon laser excitation (Figure 4.7a). The lifetime measurements of ATP-GQDs under both one- (400 nm) and two-photon excitation show nearly identical PL decay dynamics (Figure 4.7b), suggesting the common radiative recombination channels.<sup>118</sup> The PL decay curves can be fitted into a double-exponential function:  $I_{(t)} = A_1 \exp(-t/\tau_1) + A_2 \exp(-t/\tau_2)$ , where  $\tau_1$  and  $\tau_2$  are the time constants of the two radiative decay channels;  $A_1$  and  $A_2$  are the corresponding amplitudes. From the decay curves, the PL lifetimes,  $\tau_1(A_1)$  and  $\tau_2(A_2)$  are derived to be 320 ps (0.44) and 1.62 ns (0.56). The nanosecond-scale lifetime suggests that ATP-GQDs are suitable fluorescent probes for bioimaging.<sup>29</sup>

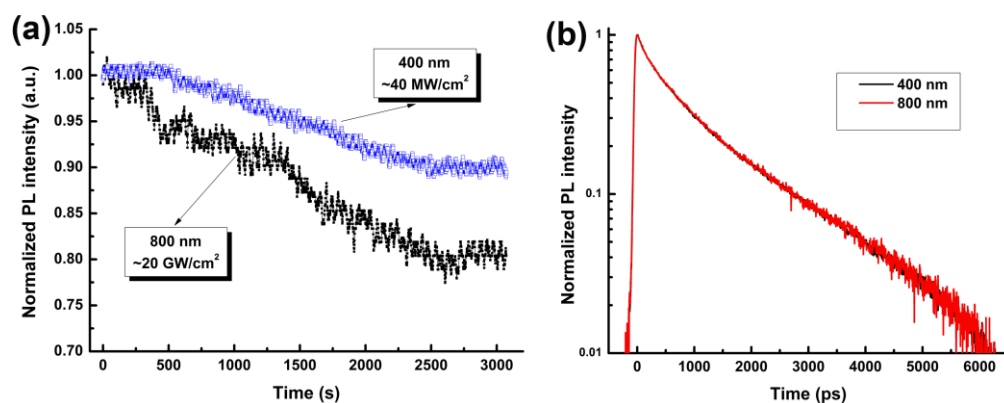


**Figure 4.7** (a) Normalized PL intensity vs. time of ATP-GQDs under one (blue) or two-photon (black) excitation. (b) Fluorescence decay of ATP-GQDs under one- (400 nm) or two-photon (800 nm) excitation.

#### 4.2.7 Transferrin conjugated GQDs for in-vitro cell imaging

ATP-GQD is desirable as a fluorescence tag for bioimaging because of its high QY, small molecular weight, excellent photostability, and good biocompatibility (Figure 4.8). As a proof of concept demonstration, we conjugate ATP-GQD with transferrin molecule for imaging and real-time tracking of transferrin receptors in human cervical cancer cells (HeLa) cells.

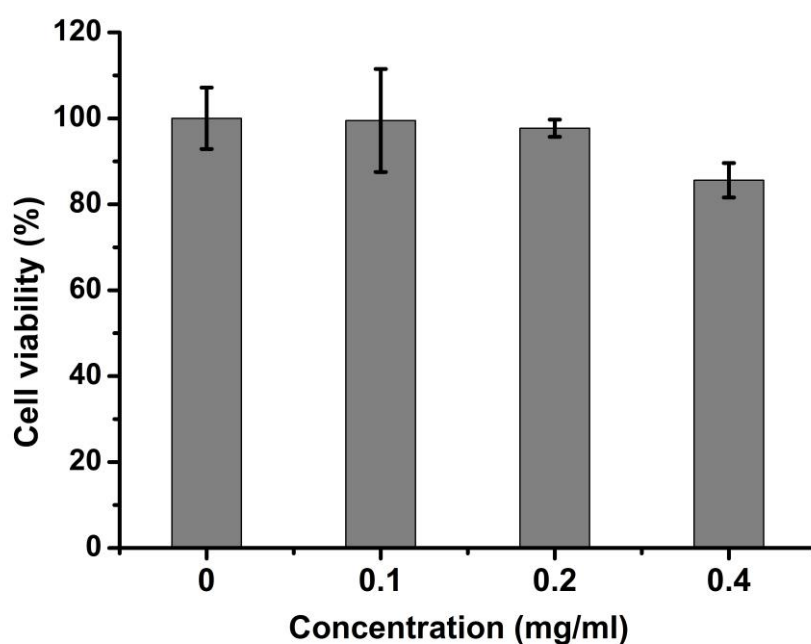


**Figure 4.8** Cell viability assay of HeLa cells in the presence of GQDs at various concentrations.

Many cancerous cells overexpress transferrin receptors, which are responsible for internalization and recycling of iron-bound transferrin molecules. Gel electrophoresis experiment indicates that the molecular weight of transferrin-conjugated GQD (Tr-GQD) is similar to that of bare transferrin molecule (80 kDa) implying one-to-one pairing between ATP-GQD and transferrin (Figure 4.9). The successful conjugation of transferrin is evidenced by staining of Tr-GQD by transferrin-binding coomassie blue (Figure 4.9a).

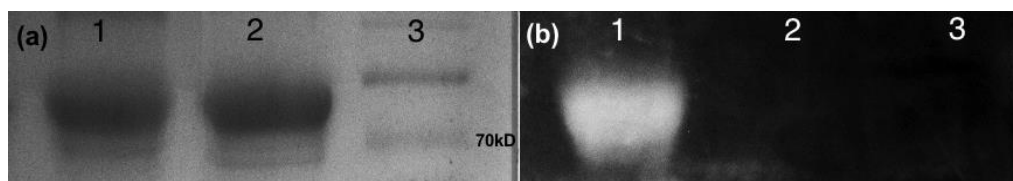


**Figure 4.9** Gel electrophoresis images of Tr-GQDs (lane 1), transferrin (lane 2) and protein marker (lane 3) under white light (a) and 488 nm excitation (b).

Using confocal microscopy, it is found that ATP-GQDs can be readily and non-specifically uptaken by HeLa cells (Figure 4.10a). The internalized ATP-GQDs scatter in the cytoplasm. In comparison, the uptaken Tr-GQDs are segregated near the nucleus because the specific binding of Tr-GQDs with transferrin receptors on the cell membrane triggers endocytosis and compartmentalization in the recycling endosomes (a network of tubular structures adjacent to the nucleus) as shown in Figure 4.10b.<sup>141</sup> When excess free transferrin molecules are introduced together with Tr-GQDs, fewer fluorescent puncta could be observed within the cells due to competitive inhibition, confirming the specific binding between Tr-GQDs and transferrin receptors (Figure 4.10c). Furthermore, Tr-GQD staining is much weaker in human fibroblasts (ATCC) because these non-cancerous cells have lower number of transferrin receptors expressed on the membrane. Using total internal reflection fluorescence microscopy (TIRFM) which evanescently illuminates only the thin plasmalemmal region (< 200 nm thick), it is further observed that Tr-GQD / transferrin complexes on the cell membrane are quickly endocytosed and many endocytic



events are observed within 3 mins of imaging (Figure 4.10e). Individual endocytic (Figure 4.10e, right top) and exocytic events (Figure 4.10e, right bottom) of the vesicles containing internalized complexes can also be resolved.

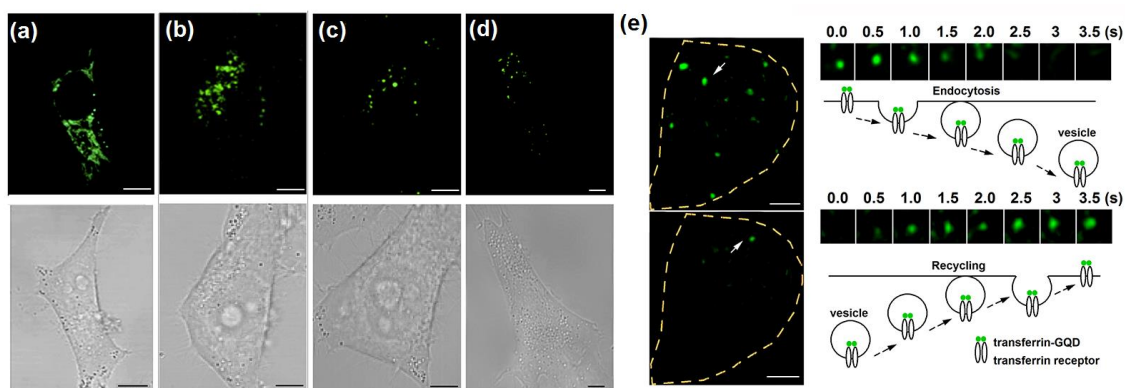


**Figure 4.10.** Confocal (top) and bright-field (bottom) images (Scale bars = 5 μm). of HeLa cells labeled with (a) ATP-GQDs, (b) Tr-GQDs, and (c) excess transferrin molecules together with Tr-GQDs. (d) Confocal and bright-field images of human fibroblast cells labeled with Tr-GQDs. (e) TIRFM images of HeLa cells with transferrin receptors labeled by Tr-GQDs (Scale bars = 5 μm). Right top: a typical endocytic event of Tr-GQD/transferrin receptor complexes; Right bottom: a typical endocytotic event of a vesicle containing Tr-GQD / receptor complexes.

### 4.3 Conclusions

In summary, we have devised a simple strategy to synthesize N and P co-doped GQDs using a biomolecule (ATP) as the precursor. Such novel QD exhibits high brightness (QY ~27.5% and ~53.0% after chemical reduction), low molecular weight (~1.4 kDa), strong two-photon excitation property (absorption cross section as high as 20000 GM), excellent one-photon and two-photon stability, good biocompatibility, high water solubility, and ease to be conjugated with biomolecules. We further demonstrate the potential of ATP-GQD for real-time molecular tracking in live cells whereby uncovering the dynamic cellular events, in this case, distribution, trafficking, and recycling of transferrin receptors.

This chapter (including phrases and figures) is adapted/ reproduced with permission from our published article “Nitrogen and phosphorus co-doped graphene quantum dots: synthesis from adenosine triphosphate, optical properties, and cellular imaging Nanoscale, 2015, 7, 8159.” Copyright 2015, The Royal Society of Chemistry

## Chapter 5 Graphene Quantum Dots as Robust Carriers for Hydrophobic Drugs

Graphene-based materials have been used as carriers for drug and gene delivery<sup>142,83</sup> because of their biocompatible nature, vast surface area, ease of surface modification and small size. While, the small size facilitates rapid cellular internalization through endocytic mechanisms<sup>143</sup> (clathrin, caveolae-mediated), the large surface area augments high drug loading through  $\pi$ - $\pi$ , electrostatic and other non-covalent interactions that are advantageous for controlling the release kinetics. GQDs are promising candidates as drug carriers for  $\pi$ -conjugated drugs due to their high biocompatibility, large surface to volume ratio and hydrophilicity.<sup>144</sup> Furthermore their stable photoluminescence provides avenues for in-vitro tracking.<sup>22</sup> Furthermore, the numerous functional groups (carboxyl, hydroxyl) on GQDs are suitable for bio-conjugation with targeting molecules or proteins for cell-specific uptake.

GQDs are reported perform as good drug carriers for amphiphilic drugs like doxorubicin that has a predominantly  $\pi$  conjugated structure.<sup>85, 145</sup> However, the use of GQDs as carriers for highly hydrophobic drugs has not yet been explored. We speculate that the higher crystallinity and number of  $sp^2$  domains would make GQDs as a suitable carrier for hydrophobic  $\pi$  conjugated drugs.

In this chapter we explore the use of GQD as a carrier for hydrophobic anticancer drug,  $\beta$ -Lapachone. A high yield top-down synthetic strategy using carbon black as a precursor was demonstrated for the synthesis of GQDs. The as prepared GQDs show good fluorescence and biocompatibility. The drug loaded GQDs exhibit enhanced cytotoxicity at low drug doses for two different cancer cell lines as compared to free drug. The drug release is pH dependent and shows a burst release profile at low pH.

## **5.1 Materials and Methods**

### ***5.1.1 Synthesis of GQDs***

Carbon black (5 g) was mixed with 5.0 g of  $\text{NaNO}_3$  and 250 ml of concentrated  $\text{H}_2\text{SO}_4$ . The mixture was cooled to  $0^\circ\text{C}$  in an ice bath and stirred for 2 h. Then, 30 g of  $\text{KMnO}_4$  was added slowly and continuously stirred for another 1.5 hours (temperature was maintained at  $0^\circ\text{C}$  throughout mixing). The cooling bath was removed and the mixture was cooled to room temperature and kept left overnight with stirring. It was then treated with 300 ml DI water and 30 ml of 30%  $\text{H}_2\text{O}_2$ .

The resulting oxidized carbon black was washed several times with distilled water to remove the impurities and oven dried completely. Then this 3g of the dried carbon black was loaded into a ball milling apparatus and set at 500 rpm for 48 hrs for mechanical cleaving.

After the ball milling process, the resultant powder was first washed with dilute HCl followed by neutralization with ammonia. The solution was further vacuum filtered by  $0.2\mu\text{m}$  membrane to obtain the soluble GQDs. The GQDs were size separated using centrifugal filtration ( $< 3 \text{ KDa}$ ,  $3\text{-}10\text{KDa}$ ,  $>10 \text{ KDa}$ ) and stored at room temperature.

### ***5.1.2 Drug Loading***

Various GQD:drug ratios were tried out for loading to see the effect of drug loading on the influence on GQDs fluorescence upon loading. Briefly, 0.1mg of GQDs was fixed and the drug amounts were varied as to match the GQD: drug ratios of 1:1, 2:1 and 5:1. The mixture was allowed to react in 5ml (pH 8, PBS) buffer in a beaker for 24h with stirring. The unreacted drug was removed using centrifugal filtration or dialysis. The amount of drug loaded was calculated using the absorbance measurement at 440nm.

### ***5.1.3 Drug Release***

The GQD-drug conjugates were dialysed against PBS buffers of pH 5.5 and 7.4 for mimicking cancer cell environment (pH 5.5) and normal cell environment (pH 7.4). The amount of drug released was determined by measuring the absorbance value of the sink solution (50 ml) at 440 nm at various time intervals. The experiments were conducted as triplicates.

### ***5.1.4 Cell culture and cytotoxicity assay***

Human breast cancer cells MCF-7, cervical cancer HeLa cells were cultured in Dulbecco's modified eagle media (DMEM) supplemented with 10% fetal bovine serum and 1% penicillin streptomycin and 1% sodium pyruvate at 37°C under 5% CO<sub>2</sub> for a week and used for further experiments.

To test the biocompatibility of GQDs cultured, cells were seeded onto 96 well plates and grown till they attained 80% confluency. The media was removed and the cells were washed with PBS thrice after which they were incubated with GQDs of various concentrations from 50 to 200 µg/ml for 24h. Cell viability was assessed using MTT assay for all both cell lines. Briefly, 100 µl of 10% MTT solution in cell media was added to the wells and left for a 4h incubation period. Finally the MTT solution was removed and 100 µl of filtered DMSO was added to dissolve the crystals formed and absorbance at 570 nm was recorded to assess cell viability, with the untreated cells serving as positive control (100 % cell viability).

A similar procedure was performed to evaluate the anticancer effects of GQD-drug conjugates. Briefly, cells were seeded onto 96% well plates and allowed to attain 80% confluency. Then cells were washed thrice with PBS (pH 7.4) and incubated with free  $\beta$ -Lapachone and GQD- $\beta$ -Lapachone in serum-free medium corresponding to a free drug concentration of 5, 10 and 15 µM. The plate was incubated for a further 24h and the

solutions (free drug and GQD-drug conjugates) were removed and cells were washed with PBS. A MTT assay was then performed to assess cell viability assuming untreated cells has 100% cell viability.

### 5.1.5 Characterizations

Samples were characterized by Raman spectroscopy (WITeck CRM200), AFM (MFP-3D AFM, Asylum Research), high-resolution transmission-electron microscopy (JEOL-2010), FTIR (Perkin-Elmer Spectrum GX FTIR system), XPS (Theta Probe), UV-vis absorption spectroscopy UV-2450 spectrophotometer (Shimadzu), Photoluminescence spectroscopy (LS-55 fluorescence spectrometer, Perkin-Elmer).

## 5.2 Results and Discussion

Ball-milling is a simple and high throughput mechanical strategy to synthesize nanomaterials. The high mechanical and thermal energy generated during the ball milling process due the collisions facilitates the breakdown of materials to form nanostructures.<sup>146-148</sup> Also, ball milling generates copious amounts of highly reactive species that indicated by the formation of sparks upon ariel contact. Here ball-milling of oxidized carbon black sheets is used to generate edge oxidized GQDs (Figure 5.1).

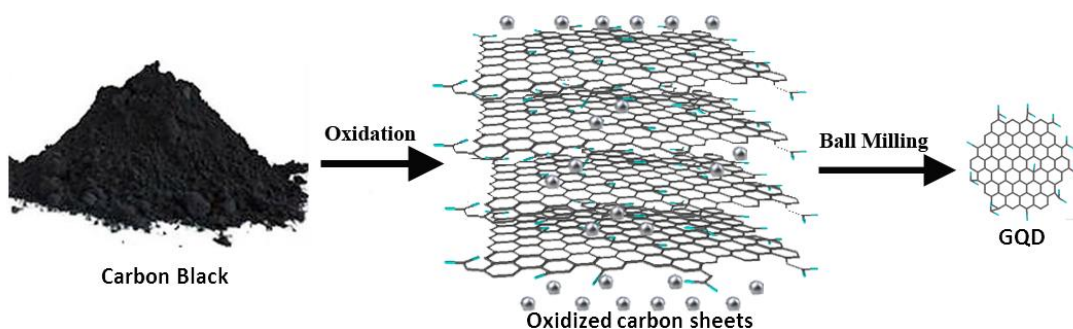


**Figure 5.1.** Schematic illustration of GQD synthesis

### 5.2.1 Morphological Characterization

From the transmission electron microscopy results it is observed that GQDs are individual sheets (Figure 5.2a) and have an average lateral size of  $\sim 9.066$  nm ( $\pm 2.04$ ,  $n=99$ ) (Figure

5.2 b). A lattice spacing of 0.25nm is observed (Figure 5.2a, inset), which corresponds to the lattice spacing of d1120 plane of graphene.<sup>99</sup> AFM images reveal that the obtained GQDs are single or few layered with average thickness of 1.2 nm ( $\pm 0.47$ , n=120) as from Figure 5.2c & d. These observations suggest that ball milling method results in the formation of non-homogenously sized GQDs, but it is effective in exfoliating monolayer graphene sheets.

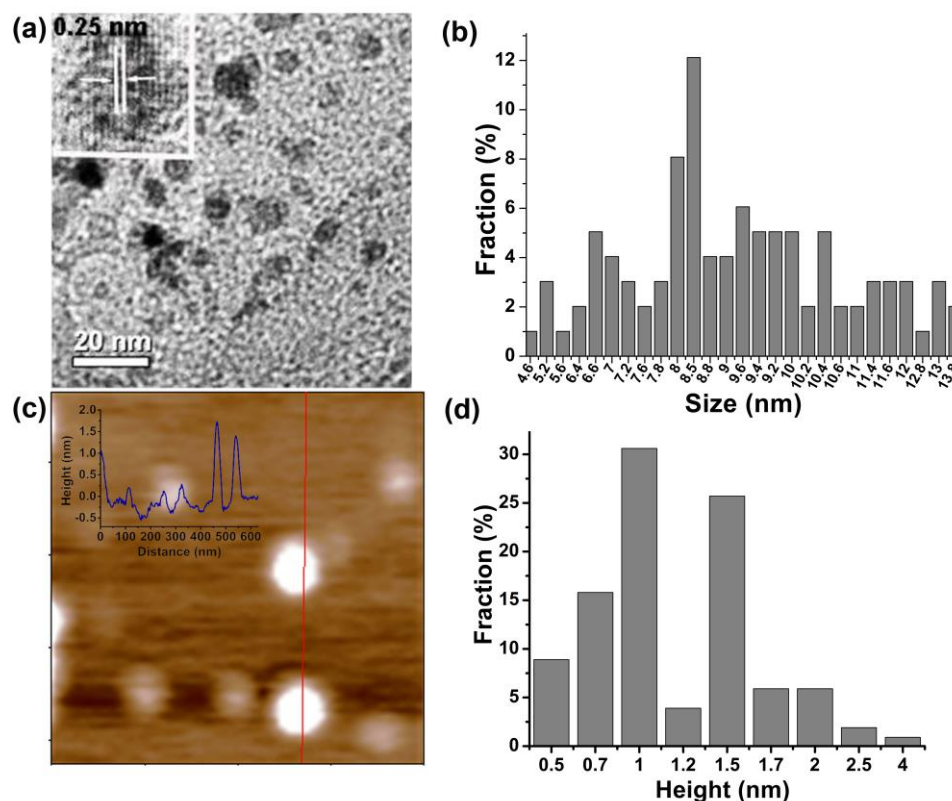


**Figure 5.2.** a) TEM and HR-TEM image of GQDs, inset reveals lattice spacing b) Size distribution histogram (n=99 particles) of GQDs c) AFM image of GQDs (inset- height profile along the indicated line) d) height distribution histogram of GQDs (n=120 particles).

### 5.2.2 Optical Characterization

As observed in GQDs synthesized by oxidative protocols, the ball-milling GQDs appear brown under bright light and green under excitation with UV light (365nm). The UV-visible spectroscopy of GQDs reveals that they show good absorption in the visible

region, which increases exponentially in the UV region with (Figure 5.3a) a peak at 230 nm, presumably due to the  $\pi$  to  $\pi^*$  transition of C=C bonds.<sup>43</sup>

The fluorescence spectra of GQDs indicate that the emission wavelength is excitation dependent probably due to the heterogeneous distribution of GQDs with various sizes (Figure 5.3b). The excitation maximum is found to be 460 nm for the corresponding emission maximum at 520 nm (Figure 5.3b). The estimated quantum yield of the GQDs is estimated to be ~10% using rhodamine 6G as the reference.

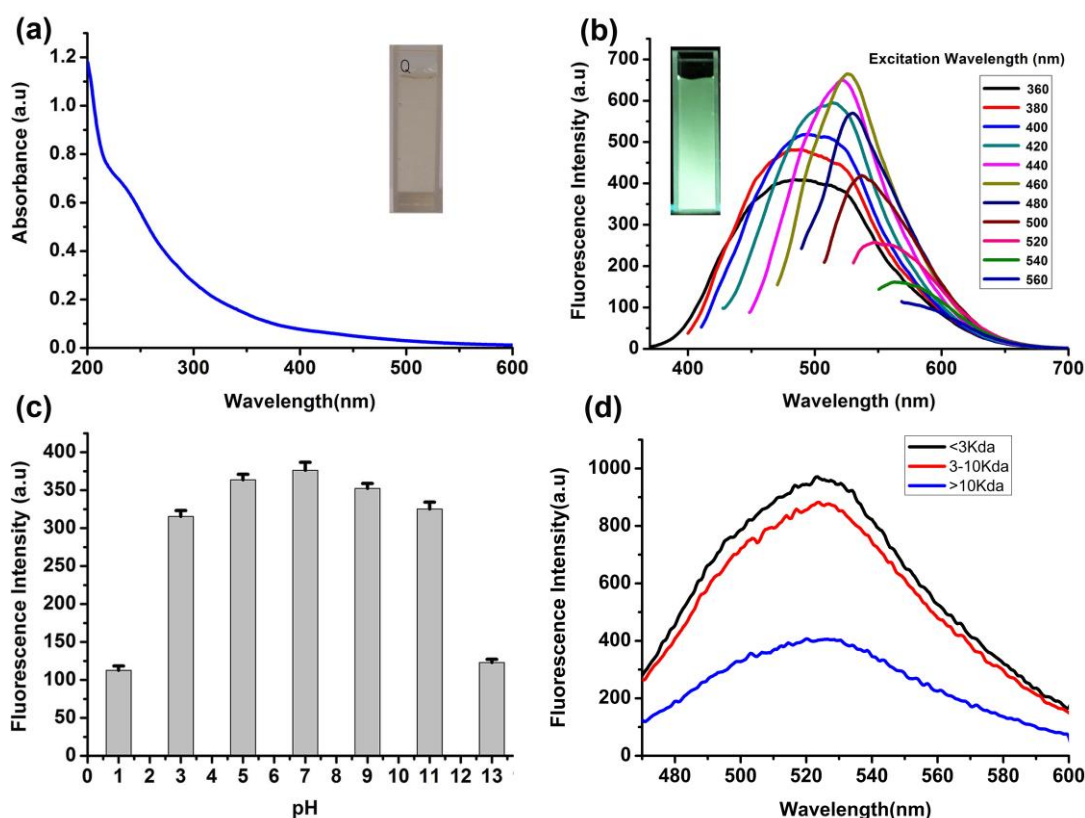


**Figure 5.3.** (a) UV absorption spectra of GQD, inset shows the image of GQD solution under bright light b) PL spectra of GQD at different excitation wavelength, inset shows image of GQD solution under UV light (365 nm) (c) Effect of pH on GQD PL intensity experiments were performed as triplicates (d) PL spectra of GQDs after size separation (excitation at 460nm, concentration 0.1mg/ml)

The influence of pH on GQD fluorescence was tested in aqueous solutions adjusted to vary from pH 1-14 using 1M HCl or 1M NaOH. GQDs show stable fluorescence within the biologically relevant pH range 5 to 9 (Figure 5.3c). However, there is significant loss



in fluorescence intensity at extreme pH such as 1 (highly acidic) and 13 (highly alkaline), which agree with the reported pH effects on carboxyl functionalized GQDs (Figure 5.3c).<sup>33</sup>

The size of the GQDs also has an influence on the fluorescence intensity. It can be observed that the largest sized (>10 KDa) GQD is least fluorescent, whereas the relatively smaller sized GQDs (<3KDa and 3-10 KDa) are highly fluorescent (3 orders of magnitude) and have similar fluorescence intensities (Figure 5.3d). The decrease in fluorescence with increased size is common due to greater surface traps and a more continuous electron band structure.

### 5.2.3 Chemical Characterization

From the FTIR spectrum of GQDs (Figure 5.4a) the characteristic peaks for C=O ( $1727\text{ cm}^{-1}$ ), C=C ( $1597\text{ cm}^{-1}$ ), COOH ( $1382\text{ cm}^{-1}$ ), C-O ( $1046\text{ cm}^{-1}$ ), and O-H ( $3100\text{ cm}^{-1}$ ) are observed indicating that the GQDs are decorated with oxygenated surface functional groups (Figure 5.4a).

XPS further confirms the presence of the functional groups with the  $\text{C}^{1s}$  spectra display a strong C=C signal at 284 eV, C-N signal at 284.4 eV and O-C=O bonds at 288 eV (Figure 5.4b).

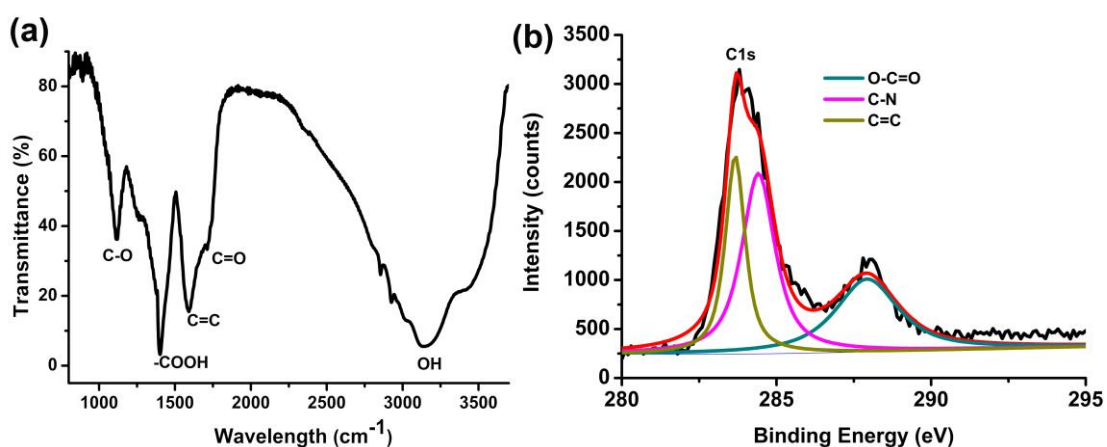


**Figure 5.4** a) FTIR spectrum of GQDs b)  $\text{C}^{1s}$  XPS spectrum of GQDs

#### 5.2.4 Drug Loading and Release

$\beta$ -Lapachone was loaded onto GQDs by simple mixing. Drug loading onto GQDs was confirmed from the resultant UV spectra (Figure 5.5a), where the drug's prominent peak at 287 nm changes steeply due to an overlap with the GQDs peak. The characteristic  $\beta$ -Lapachone peak at 440 nm that is usually used for quantitative measurements is however observed in the GQD-drug conjugates. The absorption of the drug at 440nm is also useful as GQDs show very low absorption at this wavelength.

The drug loading efficiency (LE) or capacity of GQDs is calculated by the following equation.

$$\text{LE} = \text{Mass of loaded drug} \times 100 / \text{Mass of GQD}.$$

The largest sized GQDs (>10 KDa) demonstrate the highest loading of 25% and GQDs <3 KDa and 3-10KDa- showed loading capacities of 13% and 17% respectively. The higher loading of drug onto larger sized GQDs would presumably be due the availability of larger surface of basal  $\pi$  conjugated basal plane if graphene. The highly hydrophobic nature of the drug prevents higher loading capacities onto hydrophilic GQDs. Since the difference in drug loading capacities were relatively much smaller than the difference in fluorescence of differently sized GQDs, 3-10 KDa sized GQDs were used for further experiments. The GQD-drug conjugates prepared according to the above ratio were used for biocompatibility testing and cytotoxicity assays.

On conjugation with the drug, fluorescence of GQDs is slightly lowered (Figure 5.5b) due to the  $\pi$ - $\pi$  stacking interactions between drug and GQDs quenches fluorescence by energy transfer, which promotes non-radiative recombination of electron-hole pairs.<sup>149</sup>

The drug release profiles shows that the release at pH 5.5 (cytosolic cancer cell pH) is significantly higher ( $p > 0.05$ ) than release at physiological pH of 7.4 over a 24-hour period. Nearly 80 % of the drug is released at pH 5.5 as compared to 30 % at pH 7.4 (Figure 5.5c). This confirms that GQD-conjugated drug can travel in circulation without

losing much of the bound drug and will be effective in-vivo for site-specific drug delivery. The drug release profile at pH 5.5 is similar to a biphasic release generally observed in pills and tablets.<sup>150</sup> A rapid release till 48 % occurs within the first 5 hours after which a slower release profile is observed (Figure 5.5c). Also as expected there was fluorescence recovery from the GQDs with increased time of dialysis (Figure 5.5d).

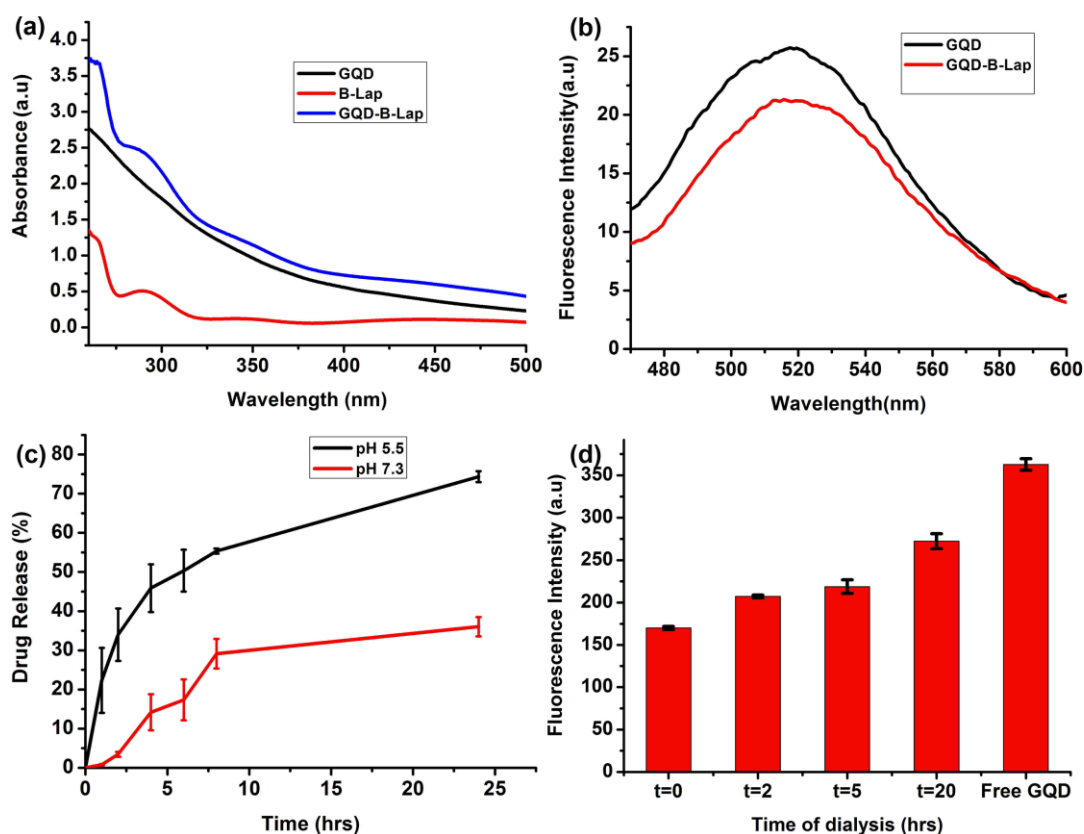


**Figure 5.5** a) UV absorption spectra of GQD, B-Lapachone and GQD-B-Lapachone b) PL spectra of GQD and GQD-B-Lapachone c) Drug release profile of GQD-B-Lapachone at pH 5.5 and pH 7.4 d). Fluorescence recovery profile of GQDs-drug conjugates measured at (t= 2, 5 and 20h).

From the cell viability assay data it can be observed that GQDs show good biocompatibility in both HeLa and MCF-7 cells (Figure 5.6a & b). The cell viability decreased by only 20% even at a high GQD concentration of 200  $\mu\text{g}/\text{ml}$ . The working concentration of GQDs used in this study is lower than 50  $\mu\text{g}/\text{ml}$ .

To estimate the performance of GQD-drug conjugates, cell viability assays are conducted in both HeLa and MCF-7 cells and their effectiveness were compared to the free drug at

the same concentrations. In the MCF-7 cells, GQD-drug conjugates perform significantly ( $p < 0.1$ ) better than free drug at the  $10\mu\text{M}$  concentration, whereas in HeLa cells, GQD-drug conjugates outperform the free drug at lower concentration of 5 and  $10\mu\text{M}$  ( $p < 0.01$ ) (Figure 5.6c). The drug is found be most effective against MCF-7 cells, where the viability goes down to 22% at  $5\mu\text{M}$  drug concentration (Figure 5.6d). The above values are for a 24-hour period and can be expected to rise as the exposure time increases, resulting in greater cancer cell death.

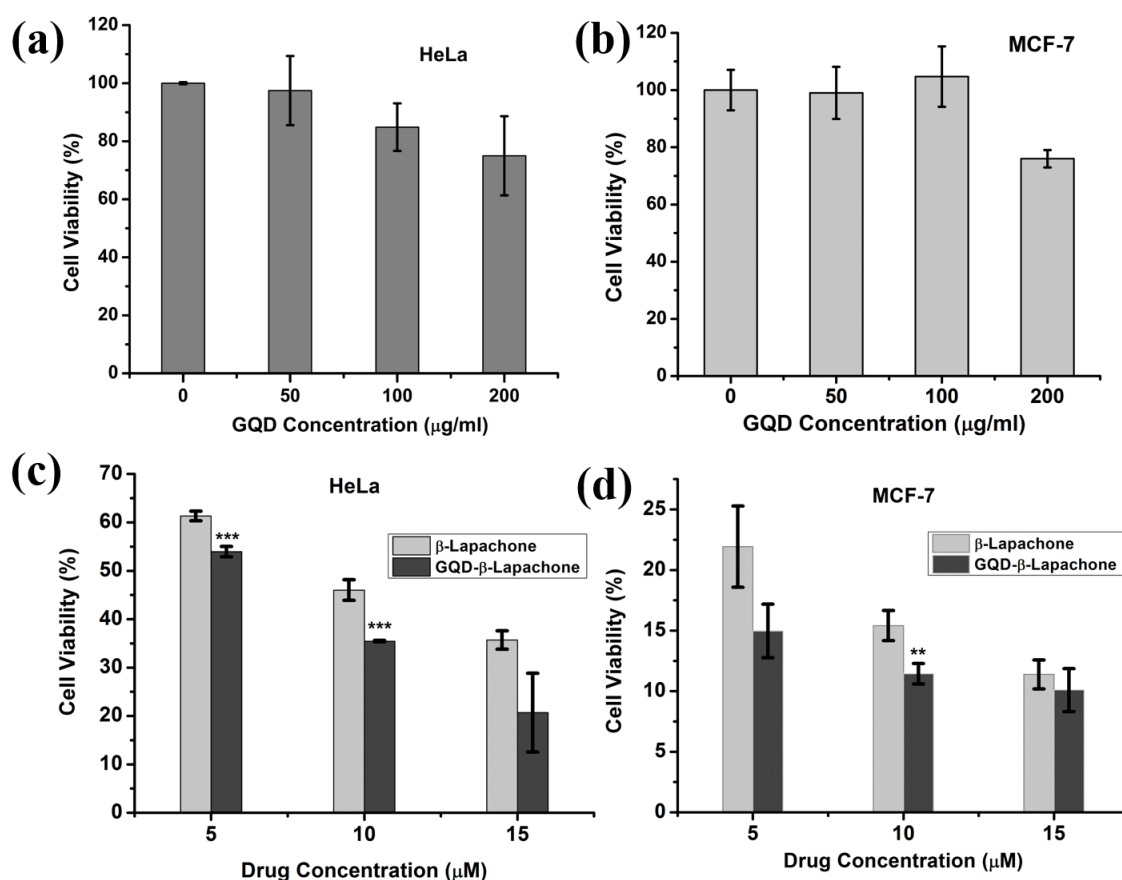


**Figure 5.6** The effect of GQDs on HeLa (a) and MCF-7 (b) cell viability at different GQD concentrations. Cytotoxic effect of GQD-drug conjugates and free drug (relative to untreated control) on HeLa (c) and MCF-7 (d) cells treated for a 24h period.

### 5.3 Conclusion

In summary, a ball-milling method has been used for the first time to produce high yield of GQDs. The GQDs have a large size distribution and show green emission with a quantum yield of 10%. The biocompatible GQDs are used as drug carriers for the

intracellular delivery of the hydrophobic drug  $\beta$ -lapachone. We observe that the GQDs show good drug loading and follow a pH dependent drug release. Nearly 80% drug release is achieved at pH 5.5 within 24h. It is also demonstrated that the GQD-drug conjugates perform better than the free drug for cancer cell against cervical (HeLa) and breast (MCF-7) cancer cells, demonstrating its efficiency as a drug delivery vehicle. With tuning of GQD properties and tissue specific targeting, GQDs can be further explored as multi-modal drug delivery vehicles for hydrophobic drugs.

## Chapter 6 Factors Influencing GQD Fluorescence: A

### Theoretical Study

Pristine graphene is a zero band gap material with infinite exciton Bohr radius due to the linear energy dispersion of the charge carriers.<sup>2</sup> Therefore, quantum confinement arises in a graphene sheet with finite size and becomes prominent in GQDs. Hence, band gap opening (and related PL emission) of GQD should be highly size-dependent, i.e., the larger its diameter the longer wavelength it emits. By definition graphene quantum dots are small sheets of graphene containing entirely  $sp^2$  hybridized carbon at the core perhaps with some oxygenated groups at the edges. Such GQDs would the quantum confinement effects similar to other semiconductor quantum dots. However, such expected size-dependent emission, however, has not been unambiguously demonstrated experimentally.

The synthesized GQDs (ranging from 1.5 to 60 nm) can emit different PL colors (including deep UV, blue, green, yellow and red) without obvious size dependence.<sup>151</sup> The large GQDs (~60 nm) synthesized by pyrolysis of hexa-*peri*-hexabenzocoronene (HBC) molecules emit blue fluorescence.<sup>152</sup> However, the small GQDs (1.5 – 5 nm) hydrothermally cropped from graphene oxide (GO) sheets are green fluorescent.<sup>33</sup> With similar size (2 – 3 nm), the GQDs oxidatively exfoliated from carbon black are green<sup>153</sup> while the GQDs electrochemically cut from defect-free CVD-grown graphene are blue.<sup>154</sup> These observed discrepancies are because of the large and uncontrolled heterogeneity of GQDs synthesized by the current approaches and the fact that the optical properties of GQDs sensitively depend on a number of parameters (e.g., size, chemical moieties, and defects). Theoretical modeling and calculations allow us to specifically investigate the influences of any particular parameter that influence GQD PL.

This chapter reports the systematic theoretical investigation of such parameters to provide better understanding of mechanisms behind GQD fluorescence.

## 6.1 Computational Methods

All the calculations are carried out using Gaussian 09 suite of program<sup>155</sup>. The ground-state geometries of GQDs were firstly optimized by DFT<sup>156, 157</sup> B3LYP (Becke's three-parameter hybrid function<sup>158</sup> with the non-local correlation of Lee-Yang-Parr<sup>159</sup>) method with the Pople 6-31G(d) basis set (B3LYP/6-31G(d)). The dangling carbon bonds are passivated by hydrogen atoms. The absorption spectra of GQDs were calculated using TDDFT method (at the B3LYP/6-31G(d) level) based on optimized ground-state geometries. The first excited state was optimized using TDDFT method to calculate the emission energy (wavelength), which is the energy difference between the ground and the first excited state.

## 6.2 Results and Discussion

### 6.2.1 Effect of size

We carried out investigations to study the influence of size on GQD fluorescence. For this we modeled GQDs with varying size. To reveal the size-dependent PL of GQD, we used pristine zigzag-edged GQDs models with different diameters (Figure 6.1). From the calculations it is observed that, these GQDs (G1- G6) fluoresce from deep UV to near infrared when the size is varied from 0.46 to 2.31 nm (Figure 6.2). Specifically, the smallest GQD (benzene) emits at 235.2 nm while 2.31 nm GQD emits at 999.5 nm. The observed linear and steep size-dependence indicates that by varying the diameter of GQD from 0.89 to 1.80 nm, its emission covers the entire visible light spectrum (400 - 770 nm). The calculated emission wavelengths in vacuum (235.2, 399.5, 492.3 nm) of G1-G3 (defect- and functionality-free small  $sp^2$ -carbon clusters known as benzene, coronene, ovalene) correlates well with the experimental measurements ( $\sim 278$  nm in water,<sup>160</sup>  $\sim 427$  nm in dimethyl sulphoxide,<sup>161</sup>  $\sim 484$  nm in tetrabutylammonium sulfonate salt,<sup>162</sup> respectively). As expected, as size increases the decrease of band gap resulting from  $\pi$ -electron delocalization induces a red shift in emission. This size-dependent emission has been traditionally observed in metallic semi-conductor QDs.<sup>163-167</sup>

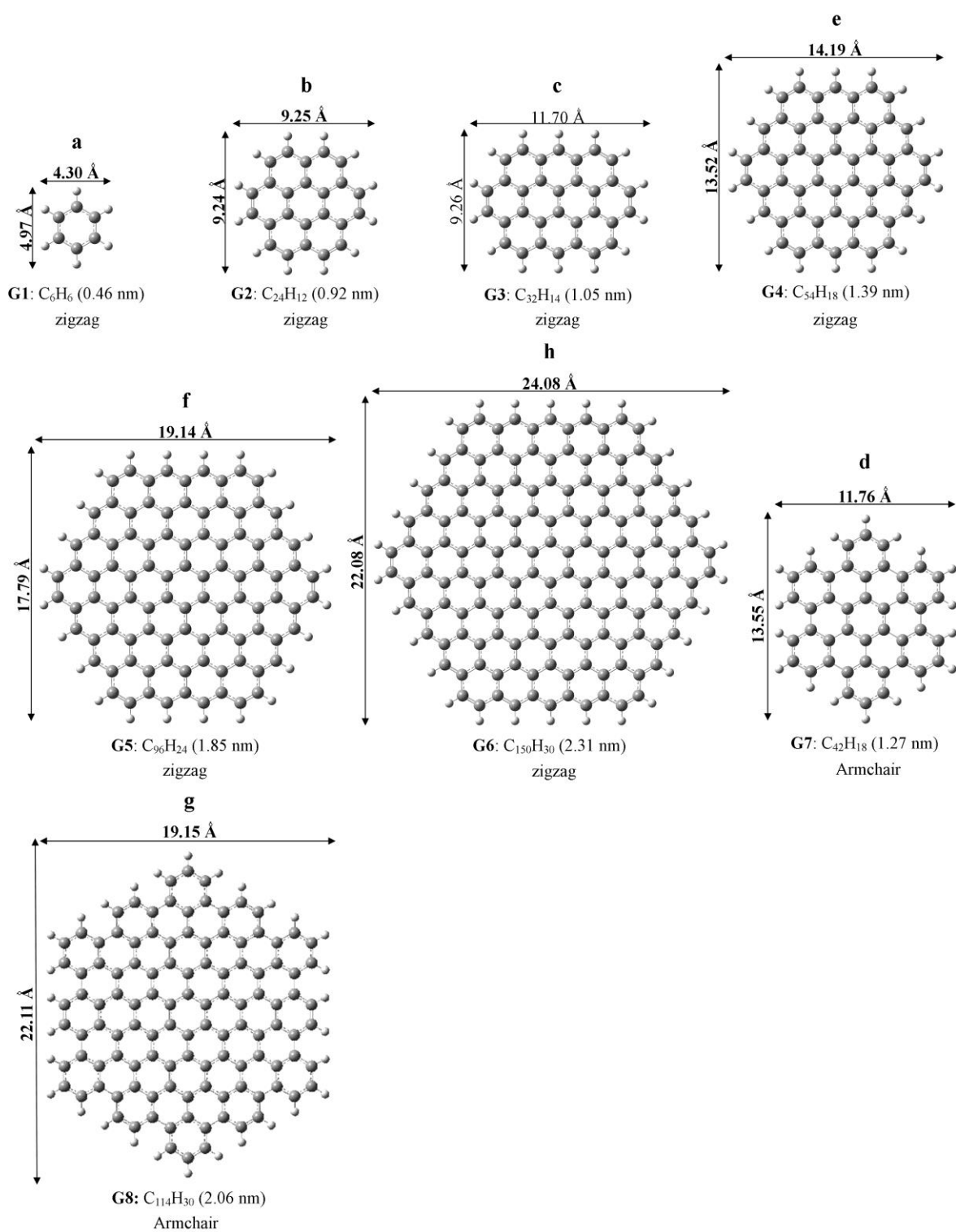


**Figure 6.1** Structure of hexagonal GQDs with zigzag edge (G1-G6) and armchair edge (G7-G8).



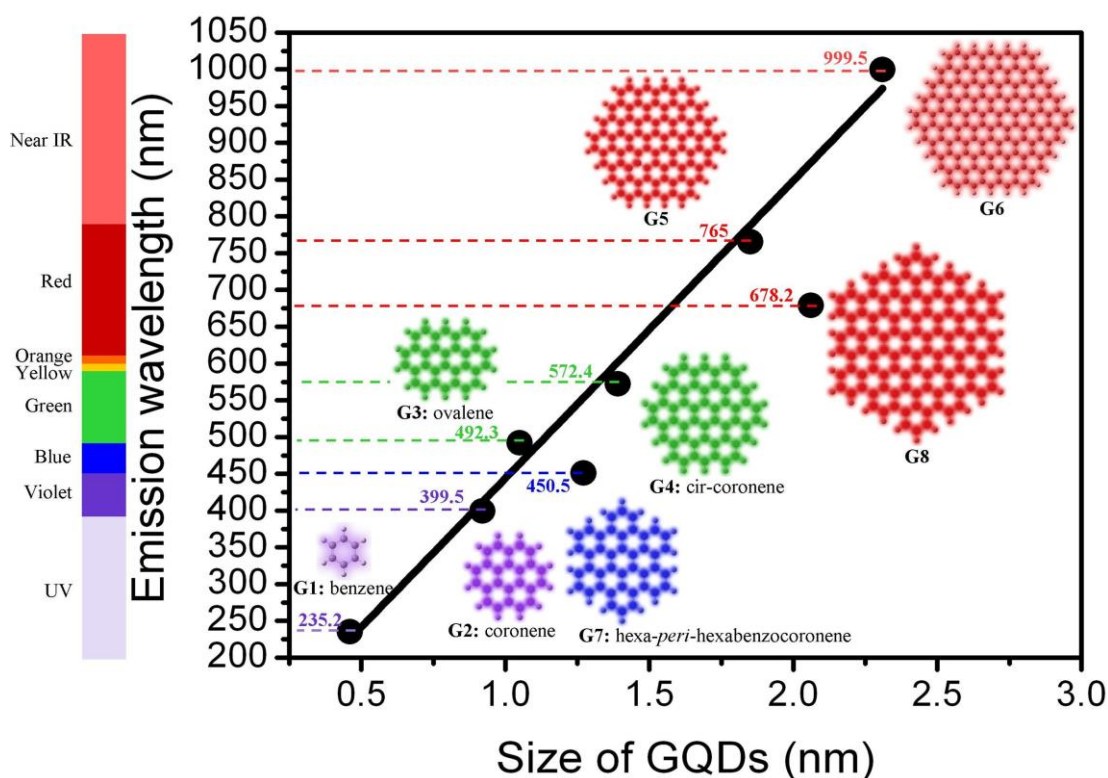


**Figure 6.2** Calculated emission wavelength (nm) using TDDFT method in vacuum as a function of the diameter of GQDs. The solid line is the linear fitting of zigzag-edged GQDs (G1 – G6). The indicated diameter is the average of the horizontal and vertical dimensions.

### 6.2.2 Effect of edge configuration

The edge configuration of GQDs can also influence the confinement properties. Graphene can have either zigzag or armchair edges and it has been shown that graphene nanoribbons (GNRs) with dominant zigzag edges have a smaller band gap (0.14 eV) as compared to similarly-sized GNRs with dominant armchair edges (0.38 eV),<sup>168</sup> because of localized states on zigzag edges.<sup>169</sup> We observe a similar trend for GQDs where the localized states in zigzag-edged GQD are pushed to the edge sites while similarly-sized armchair-edged GQD has localized states scattered in the center. As opposed to their armchair-edged counterparts, the localized states at zigzag edge sites lower the energy of conduction band and thus reduce the band gap. Thus, it no surprise that the armchair edge would widen the band gap of GQD and consequently blue-shift the emission. As observed from our calculations, 1.27 nm and 2.06 nm armchair-edged GQDs (G7 and G8

in Figure 6.2) emit at 450.5 and 678.2 nm while the predicted emission wavelengths of their zigzag-edged counterparts are ~551 and ~872 nm, respectively.

### ***6.2.3 Effect of oxygenated functional groups***

Most practical synthesis approaches for GQDs often render them with functional groups (e.g., oxygenated groups resulting from the oxidative exfoliation processes). From our calculations we find that oxidation of GQDs by –OH or –COOH functional groups red-shifts the emission peaks due to band gap reduction, in a coverage dependent manner (Figure 6.3a). Attaching –OH groups to the edge carbon atoms (varying from 0 - 100% coverage) continuously tunes G4 from green (572.4 nm) to red (732.3 nm). Edge -COOH groups also red-shift the fluorescence emission (Figure 6.3a). In contrast to the smooth change observed in incremental functionalization of edges, -OH groups conjugated on the basal plane of GQD cause more drastic red-shift because of disruption of graphitic carbon lattice. Specifically, two -OH groups on the basal plane of G4 makes it to emit red fluorescence at 746.1 nm. The predicted red-shift of oxidized GQDs is in line with experimental observations. For example, the GQDs (2-7 nm) exfoliated by acid oxidation emit greenish yellow-luminescence (~500 nm) and they become blue-luminescence (~450 nm) after reduction by NaBH<sub>4</sub>.<sup>19</sup>

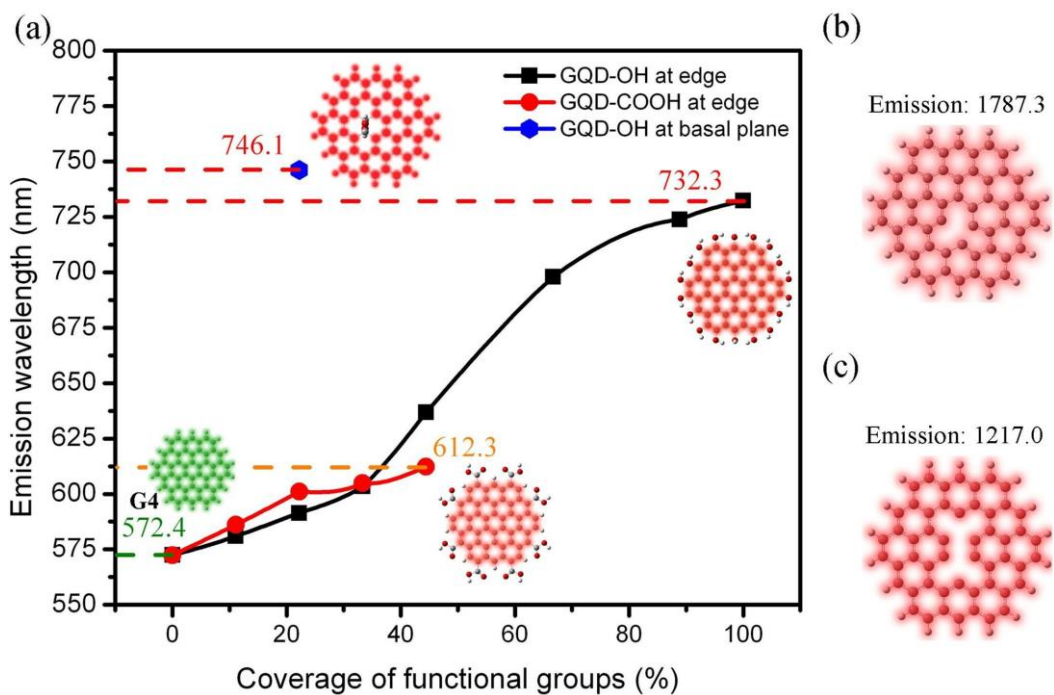


**Figure 6.3.** (a) Emission wavelength of oxidized GQD (G4) as a function of the coverage of –OH and –COOH groups. (b) and (c) are G4 with single or double vacancy defect, respectively.

#### 6.2.4 Effect of vacancy defects

GQDs synthesized by top-down methods usually bear number of lattice defects. Our calculations show that creating single or double vacancy defects on green G4 largely red-shifts the emission peak to 1787.3 or 1217.0 nm, respectively (Figure 6.3b and c). It indicates the strong influence of vacancy defects.

#### 6.2.5 Effect of hybridization state in larger GQDs

From our calculations we have demonstrated that the PL properties of GQDs can be tuned by their size, edge structure, shape, functional groups, and defects. However, when correlated experimentally, red-shifting effects induced by functional groups and defects do not completely explain why relatively large and dopant-free GQDs (a few nm) synthesized by top-down methods are usually green or blue, instead of red as predicted in Figure 6.2.<sup>154, 170,33</sup> Loh *et al.*,<sup>171</sup> Chien *et al.*<sup>172</sup> and Eda *et al.*<sup>173</sup> have proposed that the small  $sp^2$  clusters isolated by  $sp^3$  carbons are responsible for the observed PL emission

from graphene oxide (GO) sheets. Since most GQDs are synthesized from GO or with extreme oxidative procedures we speculate that most synthesized GQDs are composed of isolated  $sp^2$  clusters, which dictate their PL properties.

To test this hypothesis, we calculated the emission of small GQD-like models consisting of small  $sp^2$  clusters (benzene or coronene) joined by either  $sp^2$  or  $sp^3$  carbons (Figure 6.4). Our calculations show that the molecule consisting of two benzene molecules connected *via* two  $sp^2$  carbons (i.e., anthracene molecule, Figure 6.4a) emits blue fluorescence at 435.0 nm, close to the experimentally measured value<sup>160</sup> whereas the molecule with benzene rings are connected with two (Figure 6.4b) and six (Figure 6.4c, top)  $sp^3$  carbons, emit DUV at 256.9 nm or 241.9 nm respectively. Similarly, when  $sp^3$  carbons join six benzenes and two coronenes, the emission of the entire GQD is close to the individual benzene or coronene molecules (Figure 6.4d-g). These results imply that, when  $sp^3$  carbons isolate small  $sp^2$  clusters,  $\pi$ -electrons are confined within these domains and these small individual  $sp^2$  clusters dominate PL emission.

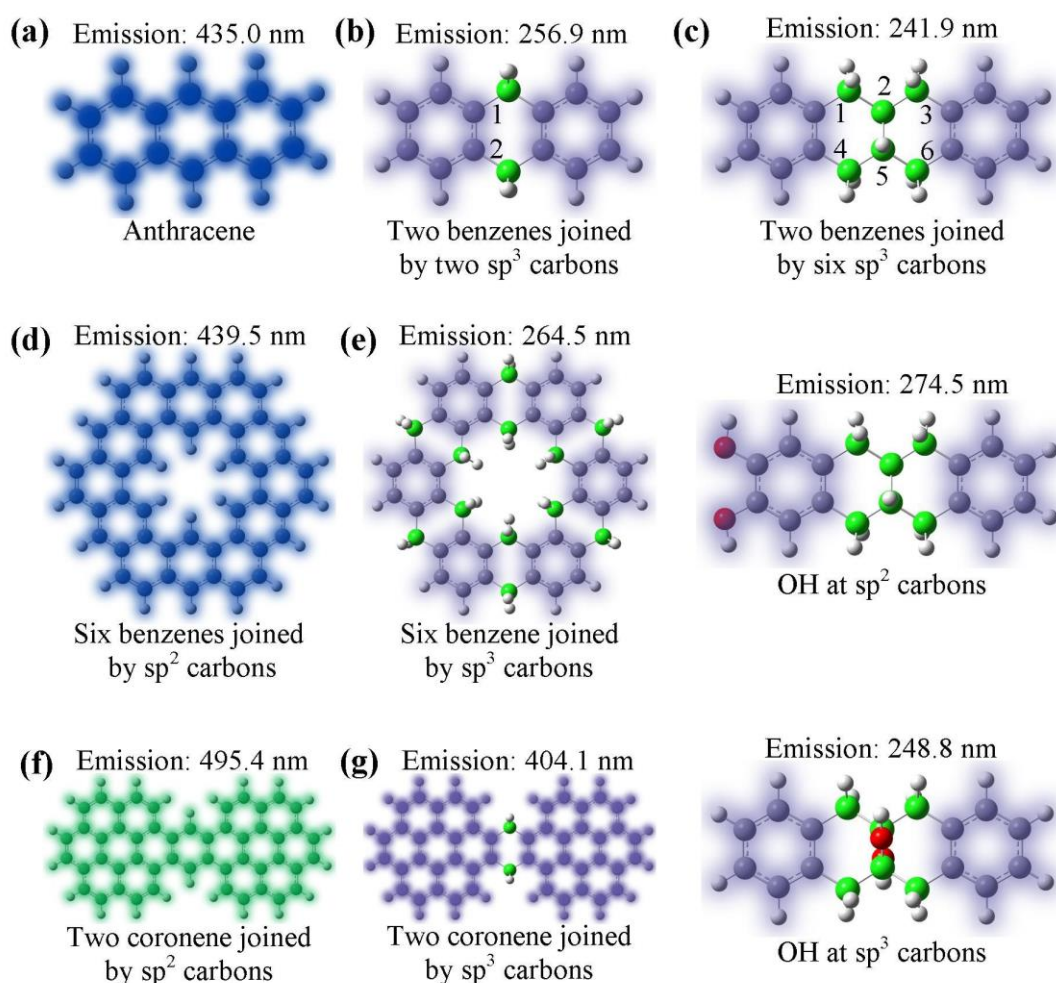


**Figure 6.4** Two benzenes joined *via* (a) two  $sp^2$  carbons (i.e., anthracene), (b) two  $sp^3$  carbons (green spheres), or (c) six  $sp^3$  carbons (top). In c, middle: two H atoms of benzene are substituted with  $-OH$  groups (red spheres); bottom: substituting two H atoms of the bridging  $sp^3$  carbons with  $-OH$  groups. (d and e) Six benzenes are joined *via*  $sp^2$  or  $sp^3$  carbons, respectively. (f and g) Two coronenes are joined *via*  $sp^2$  or  $sp^3$  carbons, respectively.

To investigate the effects of oxidation, two  $-OH$  groups are attached to benzene without altering the  $sp^2$  hybridization state of carbon atoms. This shifts the emission wavelength from 241.9 to 274.5 nm (Figure 6.4c, middle). On the other hand, attaching two  $-OH$  groups onto the bridging  $sp^3$  carbons only slightly shifts the emission to 248.8 nm (Figure 6.4c, bottom). This suggests that oxidation at  $sp^2$  clusters can exert stronger influence on PL than oxidation at  $sp^3$  carbons.

Figure 6.5a depicts a GQD ( $C_{96}H_{58}$ ) consisting of 4  $sp^2$  domains (pyrene) separated by  $sp^3$  carbon network. This GQD has a ground-state band gap of 3.58 eV, which is much larger than that of the pristine  $sp^2$ -hybridized counterpart (0.35 eV). It emits violet fluorescence at 418.1 nm, which is red-shifted as compared to free pyrene molecule (emitting at 359.4 nm). The pyrene domains embedded in  $C_{96}H_{58}$  GQD are bonded to either (a) five  $sp^3$  carbons (pentamethyl pyrene which emits at 389.2 nm) or (b) six  $sp^3$  carbons (hexamethyl-pyrene which emits at 404.9 nm) (Figure 6.5a). Evidently, the emission of the entire GQD is dependent more strongly on the hexamethyl-pyrene domains.

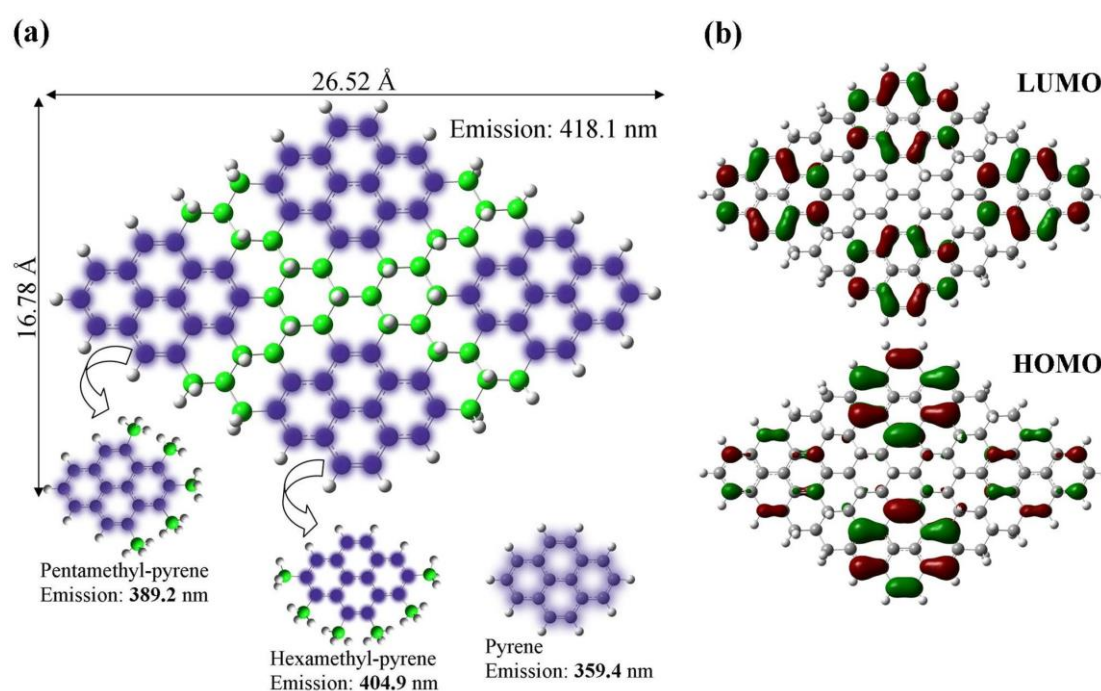


**Figure 6.5.** (a) GQD composed of four pyrene domains separated by  $sp^3$  carbons (green spheres). (b) Molecular orbitals for LUMO and HOMO from ground-state.

Therefore, it can be concluded that PL of a heterogeneous GQD ( $C_{96}H_{58}$  here) is essentially determined by the  $sp^2$  domains of lowest energy band gap (hexamethyl-pyrene here). To further support the notion that the PL properties of heterogeneously hybridized GQDs are dictated by the small  $sp^2$  clusters, we show that increasing the size of  $sp^2$  domains leads to the decrease of ground-state band gap of GQD (Figure 6.6a). In



addition, with the size of  $sp^2$  clusters fixed, increasing the diameter of GQDs (as well as the number of  $sp^2$  clusters) does not alter the ground-state band gap (Figure 6.6b)

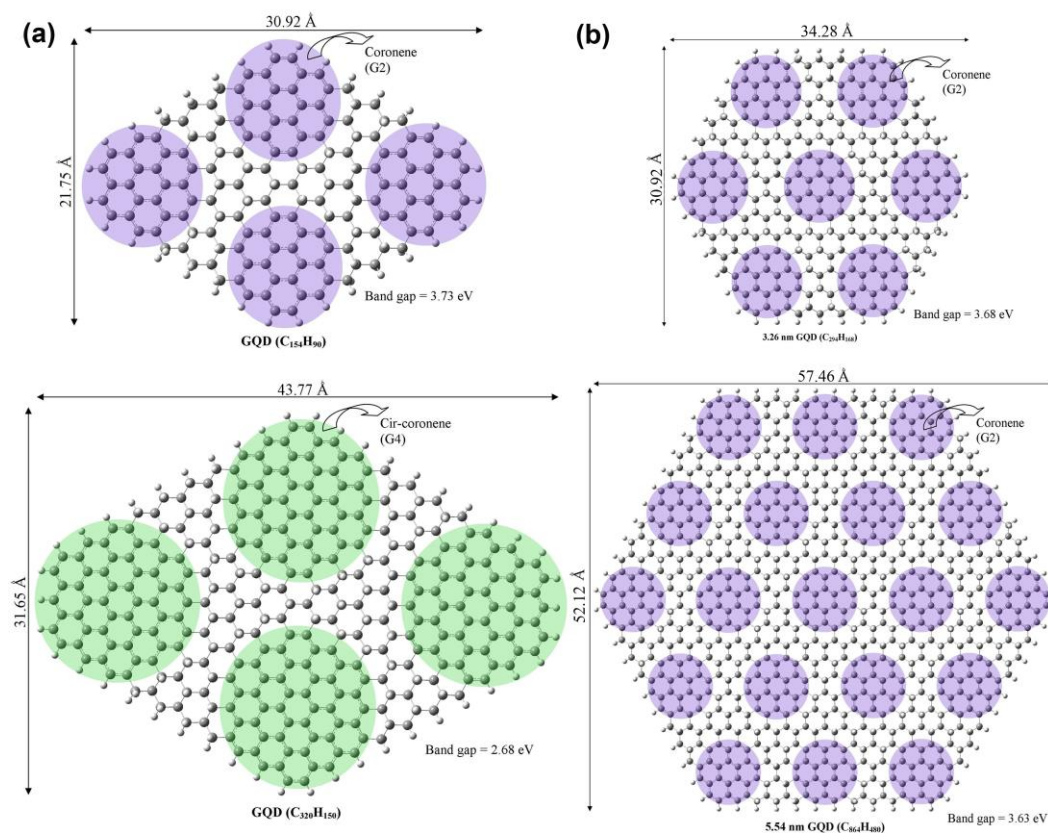


**Figure 6.6** (a) Heterogeneously hybridized GQDs with differently sized  $sp^2$  domains composed of four coronene (Top) and (b) four cir-coronene (Bottom) domains. The GQD (C154H90) and (C320H150) have ground-state band gap of 3.73 and 2.68 eV, respectively. (b) 3.26 nm C294H168 GQD (Top) and 5.54 nm C864H480 GQD (bottom) composed of seven and nineteen coronene domains, respectively.

This study provides explanation to the previous experimental observations. For example, the peculiar size-increase induced blue-shift observed by Kim *et al.* can be explained by the increase of armchair edge configurations in large GQDs.<sup>11</sup> Hexa-peri-hexabenzocoronene (HBC) emits blue fluorescence at ~490 nm in 2-methyl-tetrahydrofuran.<sup>174</sup> GQDs (~60 nm) obtained by pyrolysis of HBC molecules followed by oxidative exfoliation also fluoresce similarly (~489 nm).<sup>152</sup> Thus, it is conceivable that the HBC domains in such a large GQD are connected by  $sp^3$  carbons causing  $\pi$ -electrons to localize on the  $sp^2$  hybridized HBC domains. Gokus *et al.* have shown that PL can be

induced in graphene by oxygen plasma treatment and attributed this phenomenon to carboxy-related localized electronic states at the oxidation sites but not to  $sp^2$  sites.<sup>175</sup> But, we show that oxygenated functional groups can only lower the band gap (instead of opening band gap for PL emission). Therefore, their observation should be resulted from creation of small  $sp^2$  clusters on graphene sheet. The GQDs synthesized from top-down approaches exhibit excitation-dependent behavior and broad emission spectrum.<sup>30,152, 154, 176-178</sup> This can be attributed to the heterogeneity of produced GQDs in size, shape, functional groups, defects, and composition of  $sp^2$  clusters.

### 6.3 Conclusion

In summary, we for the first time have systematically studied the mechanisms underlying the tunable PL properties of GQDs using DFT and TDDFT calculations. From our studies we find that the emission of zigzag-edged pristine GQDs covers the entire visible spectrum by varying the diameter from 0.89 to 1.80 nm. Armchair edge blue-shift the GQD PL emission whereas chemical functionalities and defects cause red-shift. The PL emission of a heterogeneously hybridized GQD is dictated by its isolated small  $sp^2$  domains. This study confirms the exciting possibility of GQDs to serve as universal fluorophores for various imaging purposes and shall provide important insights and guidance for the development of methods to controllably synthesize GQDs with well-defined and desired properties towards specific purposes.

This chapter (including phrases and figures) is partly adapted/ reproduced with permission from our published article “Revealing the tunable photoluminescence properties of graphene quantum dots”. J. Mater. Chem. C., 2014, 2, 6954. Copyright 2014, Royal Society of Chemistry.



## Chapter 7 Conclusions and Future Perspectives

### 7.1 Conclusions

Of the many faces of graphene, GQDs emerge as another interesting derivative that show immense promise for fundamental applications in biology or biomedicine. In this thesis we have explored various synthesis strategies for GQDs keeping in mind several issues in GQD properties that need to be addressed for their practical applications in biology. This chapter summarizes the primary results and findings of the studies that contributed to this thesis.

We have demonstrated an easy, versatile and efficient synthesis strategy for GQDs using 3-dimensional graphene electrode. We find that using 3-dimensional graphene electrode provides high conductivity for efficient exfoliation with a lower applied potential. We also observe that using an imidazolium ionic liquid for the exfoliation not only serves as the electrolyte but also chemically interacts with the GQDs to give functionality. The as-synthesized imidazolium ion functionalized GQDs specifically interacts with ferric ions, which induces quenching of GQD fluorescence. This interaction is used to develop a fluorescence turn-off sensor for ferric ions.

The practical application of GQDs for cell labeling requires certain favorable properties like high quantum yield and ease of bio-conjugation. In this respect, we have demonstrated a simple synthesis strategy for heteroatom doped GQDs, which show higher quantum yield and ease of bioconjugation. Heteroatom doping in GQD was adopted to enhance optical properties. We also found that GQDs show good two-photon absorption properties with high absorption cross-section of 20000 GM. Using transferrin conjugated GQDs we have demonstrated labeling of HeLa cells and receptor tracking using TIRFM. We observe that GQDs show promise as robust fluorophores for cell labeling and tracking.

Apart from fluorescence, the unique structure of GQDs can serve as a platform for drug loading. In this respect we investigated use of GQDs as a carrier for hydrophobic drug  $\beta$ -lapachone and tested the efficacy of drug-GQD conjugates on two types of cancer cells. We found that GQDs show good drug loading and high pH and a burst release at low pH of 5.5. Furthermore the release of drug at physiological pH is significantly slower than low pH environment thus indicating their effectiveness in killing cancer cells. It is also demonstrated that the GQD-drug conjugates perform significantly better than the free drug for cancer cell against cervical and breast cancer cells, demonstrating its efficiency as a drug delivery vehicle.

GQDs are relatively new fluorescent materials and show interesting fluorescence properties. However, emission properties deviate from standard inorganic semiconductor QDs. In this respect we have conducted systematic theoretical studies to better understand the mechanism of GQD fluorescence. From this study, we have demonstrated that factors like edge, size, chemical functionalization and  $sp^2$  domains play a significant role on the fluorescence of GQDs. The results of this study are important to guide experimental synthesis of GQDs for improved properties and applications.

## **7.2 Future Directions**

GQDs have emerged as a new class of fluorescent nanomaterials for various applications in various fields, which have proven competitive in many aspects as compared to conventional semiconductor QDs. However research on GQDs is still at a very nascent stage and there are countless directions that remain open for exploration.

Firstly, in terms of synthesis, strategies to provide GQDs with very high yield, quantum yield and tunable emission are still the need of the hour. Exploring various new chemical synthesis techniques to produce GQDs with desired properties would be beneficial for practical applications.

Secondly, in the field of nanomedicine GQDs show enormous potential as imaging agents, drug carriers, photothermal and antibacterial agents. Since their chemical structure renders certain favorable properties they can be used as imaging as well as therapeutic agents. The  $\pi$ -conjugated structure might also be useful for delivery of small molecules such as siRNA and mRNA. The amphiphilic nature of GQDs also makes them useful as reducing agents/ templates for growth of metal nano crystals. For instance, GQD assisted growth of iron oxide nanoparticles can be used as MRI contrast agents or multimodal drug delivery vehicles.

Thirdly, the experimental synthesis of GQDs would also help researchers understand the properties and behavior of small sheets of graphene. The study of properties of such dimensionally confined graphene is incumbent for the development of exciting new field of applications.

Lastly, GQDs show immense promise for applications in various other fields like label-free detection, energy, electrochemistry, catalysis, electronics, and display technologies.

## Appendix I- List of Publications

1. **Ananthanarayanan A** et al., “Nitrogen and Phosphorus co-doped Graphene Quantum Dots: Synthesis from Adenosine triphosphate, Optical Properties, and Cellular Imaging” *Nanoscale*, 2015,7, 8159-8165.
2. **Ananthanarayanan A**, et al., “Facile Synthesis of Graphene Quantum Dots from 3D Graphene and their Application for  $Fe^{3+}$  Sensing”, *Advanced Functional Materials*, 2014, 24, 3021-3026.
3. Zheng XT\*, **Ananthanarayanan A**\*, Luo KQ, Chen P\*, 2015 “Glowing graphene quantum dots and carbon dots: properties, syntheses, and biological applications”, *Small*, 2015, 11, 1620-1636.
4. Ting SL, Ee SJ, **Ananthanarayanan A**, Leong KC, Chen P\*, “Graphene quantum dots functionalized gold nanoparticles for sensitive electrochemical detection of heavy metal ions”, *Electrochimica Acta*, 2015, 172, 7-11.
5. Sk MA, **Ananthanarayanan A**, Huang L, Lim KH, and Chen P\*, 2014, “Revealing the tunable photoluminescence properties of graphene quantum dots”, *Journal of Material Chemistry C*, 2014, 2, 6954-6960.
6. Liu Y, Loh W, **Ananthanarayanan A**, Yang C, Chen P and Xu CJ\*, 2014, “Fluorescence quenching between unbonded graphene quantum dots and gold nanoparticles upon simple mixing” *RSC Advances*, 2014,4, 35673-35677.
7. Zheng XT, Than A, **Ananthanaraya A**, Kim DH, Chen P\*, 2013, “Graphene Quantum Dots as Universal Fluorophores and Their Use to Reveal Regulated Trafficking of Insulin Receptors in Adipocytes”, *ACS Nano*, 2013, 7, 6278–6286.

## Appendix II- List of Figures

|   |    |
|---|----|
| Figure 2.1 Structural depiction of (a) GQDs. HRTEM images of (b) GQDs showing combination of zigzag and armchair edges .....  | 7  |
| Figure 2.2 (a) UV-vis absorption (ABS) spectra of the GQDs aqueous solution. (b) The excitation-dependent PL behavior of GQDs, when the GQDs were excited at wavelengths from 400 to 540 nm. (c) Two-photon-induced fluorescence spectrum of N-GQDs under 800 nm femtosecond laser excitation. Inset: Two-photon fluorescence image of dry N-GQDs (scale bar: 10 $\mu\text{m}$ ) R (d) Schematic illustration of the ECL and PL mechanisms in GQDs. $\text{R}^{\bullet+}$ , $\text{R}^{\bullet-}$ , and $\text{R}^*$ represent negatively charged, positively charged, and excited-state GQDs, respectively.....                              | 10 |
| 2.1.3 Electrochemical properties .....  | 10 |
| Figure 2.3 Top-down fabrication of GQDs. Schematic illustration of (a) GQDs synthesis by acidic oxidation of coal.; (b) mechanism for the hydrothermal cutting of oxidized graphene sheets into GQDs: a mixed epoxy chain composed of epoxy and carbonyl pair groups (left) is converted into a complete cut (right) under the hydrothermal treatment. Reproduced with permission. <sup>33</sup> (c) exfoliation process showing the attack of the graphite edge planes by hydroxyl and oxygen radicals, and intercalation of $\text{BF}_4^-$ anion.....  | 14 |
| Figure 2.4 (a-b) Bottom-up synthesis of large GQDs (1-3) from 3-iodo-4-bromoaniline (4) via stepwise organic chemistry. GQDs in (a) consisting of graphene moieties containing 168, 132, and 170 conjugated carbon atoms respectively.....  | 16 |
| Figure 2.5 (a-e) Application of insulin-GQD conjugates for real-time tracking of insulin receptors in adipocytes. (a) Total internal reflection fluorescence microscopy (TIRFM) image of a 3T3-L1 adipocyte after 1 h incubation with insulin conjugated GQDs. Scale bar = 5 $\mu\text{m}$ . (b) Membrane patch consisting of insulin conjugated GQD/insulin receptor clusters. (c) Endocytosis of fluorescent membrane into a vesicle. (d) Exocytosis of a vesicle containing insulin conjugated GQD/insulin receptor complexes. (e) Transient approaching and retrieval of insulin conjugated GQD/insulin receptor containing vesicle ..... | 24 |
| Figure 2.7 (a) GQD enhances the reduction of copper ions, promoting the formation of oxidative species and consequent DNA cleavage. (b) Gel electrophoresis diagram of DNA (38 $\mu\text{M}$ in bp) cleavage by copper complexes 2, 4,5 and 6 in the absence and presence of GQDs (100 $\mu\text{g mL}^{-1}$ ) in 50 mM Tris/18 mM NaCl buffer (pH 7.2) at 37 $^{\circ}\text{C}$ . Incubation time was 0.5 h. First lane on the left is the DNA control. <sup>91</sup> .....  | 35 |

|   |    |
|---|----|
| Figure 3.1. Schematic illustration of GQD synthesis from 3D graphene and mechanism of $\text{Fe}^{3+}$ detection. ....  | 37 |
| Figure 3.2. SEM images of 3D graphene (a) before and (b) after electrochemical treatment. The inset in (a) shows the surface of graphene skeleton at a higher magnification. (c) Raman spectra of 3D graphene before and after electrochemical treatment. (d) FTIR Spectra of GQDs and BMIMPF <sub>6</sub> . (e) XPS spectrum of GQDs. ....   | 41 |
| Figure 3.3 SEM images of 3D graphene after (a) electrochemical etching with 100 voltammetric cycles ( $\pm 3\text{V}$ ) and (b) electrochemical etching with a constant voltage of 3V for 300s. The former protocol leads to collapse of graphene foam while the later gives low-yield of GQD production. ....  | 42 |
| Figure 3.4. (a) Electrophoresis gel image of GQD samples. (b) AFM image and height profile (inset) of GQDs. (c) Height distribution obtained from AFM measurements (203 samples). (d) and ....  | 44 |
| (e) TEM images of GQDs. The insets show the lattice spacing of GQDs. (f) Diameter distribution obtained from TEM images (166 samples). ....   | 44 |
| Figure 3.6 (a) PL of GQDs (50 $\mu\text{g/mL}$ ) in the absence (red) and presence (purple) of 200 $\mu\text{M}$ $\text{Fe}^{3+}$ at different pH. (b) Remaining percentage of GQD PL after addition of different metal ions (400 $\mu\text{M}$ ) in acetate buffer solution (pH 4.0). (c) Emission spectra of GQDs in the presence of $\text{Fe}^{3+}$ ions at increasing concentrations ( $\square\text{M}$ ). (d) Average concentration-dependent fluorescence response in the acetate buffer solution. The error bars indicate the standard deviations ( $n = 3$ ). Linear fitting is performed in the low concentration range (black line). .... | 47 |
| Scheme 4.1 Illustration of the synthesis procedure for ATP-GQDs.....  | 52 |
| Figure 4.1 a) SEM images of carbonized ATP (cATP). The inset shows the surface of cATP sheets at higher magnification. b) Raman spectrum of carbonized ATP. c) Cyclic voltammograms of cATP in oxygen (red) or nitrogen (green) saturated KOH (0.1 M) solution. d) Linear-sweep voltammetry curves of cATP in 0.1 M KOH at different rotation speeds. The Koutecky-Levich plots at different potentials (the slopes of the curves indicate the electron transfer number of 4.2 - 4.4) are shown in inset. ....  | 56 |
| Figure 4.2 a) TEM image of ATP-GQDs. The HR-TEM image in inset reveals the lattice spacing. b) Size distribution histogram from TEM images (161 samples). c) Gel electrophoresis image of ATP-GQD samples (left: excitation at 488 nm; right: bright view). (d) AFM image of GQDs with the height profile along the indicated line shown in inset. (e) Height distribution obtained from 213 samples. ....  | 57 |

|   |    |
|---|----|
| Figure 4.3. a) FTIR spectrum of ATP-GQDs. (b, c, d) High resolution XPS spectra for $C^{1s}$ , $N^{1s}$ , and $P^{2p}$ .....  | 58 |
| Figure 4.4 (a) XRD and (b) Raman spectrum of ATP-GQDs. ....   | 59 |
| Figure 4.5. a) UV-Vis absorption (blue) and excitation (red) spectra of GQDs. The inset shows the optical image of aqueous solution of ATP-GQDs under visible (left) and UV light (right, 365 nm). (b) PL spectra of GQDs at different excitation wavelengths. (c) Laser power dependent emission spectra of ATP-GQDs under two-photon excitation using a femtosecond pulsed laser (800 nm). (d) Quadratic relation between excitation intensity and PL intensity with a fitting (red line). ....   | 60 |
| Figure 4.6 (a) PL spectra of ATP-GQDs before (black) and after (red) chemical reduction. (b) Z-scan of ATP-GQDs and water (solvent control). ....   | 62 |
| Figure 4.7 (a) Normalized PL intensity vs. time of ATP-GQDs under one (blue) or two-photon (black) excitation. (b) Fluorescence decay of ATP-GQDs under one- (400 nm) or two-photon (800 nm) excitation.....  | 63 |
| Figure 4.8 Cell viability assay of HeLa cells in the presence of GQDs at various concentrations. ....   | 63 |
| Figure 4.9 Gel electrophoresis images of Tr-GQDs (lane 1), transferrin (lane 2) and protein marker (lane 3) under white light (a) and 488 nm excitation (b). ....   | 64 |
| Figure 4.10. Confocal (top) and bright-field (bottom) images (Scale bars = 5 $\mu$ m). of HeLa cells labeled with (a) ATP-GQDs, (b) Tr-GQDs, and (c) excess transferrin molecules together with Tr-GQDs. (d) Confocal and bright-field images of human fibroblast cells labeled with Tr-GQDs. (e) TIRFM images of HeLa cells with transferrin receptors labeled by Tr-GQDs (Scale bars = 5 $\mu$ m). Right top: a typical endocytic event of Tr-GQD/transferrin receptor complexes; Right bottom: a typical endocytotic event of a vesicle containing Tr-GQD / receptor complexes. .... | 65 |
| Figure 5.1. Schematic illustration of GQD synthesis .....   | 70 |
| Figure 5.2. a) TEM and HR-TEM image of GQDs, inset reveals lattice spacing b) Size distribution histogram (n=99 particles) of GQDs c) AFM image of GQDs (inset- height profile along the indicated line) d) height distribution histogram of GQDs (n=120 particles).....  | 71 |
| Figure 5.3. (a) UV absorption spectra of GQD, inset shows the image of GQD solution under bright light b) PL spectra of GQD at different excitation wavelength, inset shows image of GQD solution under UV light (365 nm) (c) Effect of pH on GQD PL intensity experiments were performed as triplicates (d) PL spectra of GQDs after size separation (excitation at 460nm, concentration 0.1 mg/ml) .....  | 72 |

|   |    |
|---|----|
| Figure 5.4 a) FTIR spectrum of GQDs b) C <sup>1s</sup> XPS spectrum of GQDs .....   | 73 |
| Figure 5.5 a) UV absorption spectra of GQD, B-Lapachone and GQD-B-Lapachone b) PL spectra of GQD and GQD-B-Lapachone c) Drug release profile of GQD-B-Lapachone at pH 5.5 and pH 7.4 d). Fluorescence recovery profile of GQDs-drug conjugates measured at (t= 2, 5 and 20h). .....   | 75 |
| Figure 5.6 The effect of GQDs on HeLa (a) and MCF-7 (b) cell viability at different GQD concentrations. Cytotoxic effect of GQD-drug conjugates and free drug (relative to untreated control) on HeLa (c) and MCF-7 (d) cells treated for a 24h period. ....  | 76 |
| Figure 6.1 Structure of hexagonal GQDs with zigzag edge (G1-G6) and armchair edge (G7-G8). ....   | 80 |
| Figure 6.2 Calculated emission wavelength (nm) using TDDFT method in vacuum as a function of the diameter of GQDs. The solid line is the linear fitting of zigzag-edged GQDs (G1 – G6). The indicated diameter is the average of the horizontal and vertical dimensions. ....   | 81 |
| Figure 6.3. (a) Emission wavelength of oxidized GQD (G4) as a function of the coverage of –OH and –COOH groups. (b) and (c) are G4 with single or double vacancy defect, respectively. ....   | 83 |
| Figure 6.4 Two benzenes joined via (a) two sp <sup>2</sup> carbons (i.e., anthracene), (b) two sp <sup>3</sup> carbons (green spheres), or (c) six sp <sup>3</sup> carbons (top). In c, middle: two H atoms of benzene are substituted with –OH groups (red spheres); bottom: substituting two H atoms of the bridging sp <sup>3</sup> carbons with –OH groups. (d and e) Six benzenes are joined via sp <sup>2</sup> or sp <sup>3</sup> carbons, respectively. (f and g) Two coronenes are joined via sp <sup>2</sup> or sp <sup>3</sup> carbons, respectively. .... | 85 |
| Figure 6.5. (a) GQD composed of four pyrene domains separated by sp <sup>3</sup> carbons (green spheres). (b) Molecular orbitals for LUMO and HOMO from ground-state. ....  | 86 |
| Figure 6.6 (a) Heterogeneously hybridized GQDs with differently sized sp <sup>2</sup> domains composed of four coronene (Top) and (b) four cir-coronene (Bottom) domains. The GQD (C154H90) and (C320H150) have ground-state band gap of 3.73 and 2.68 eV, respectively. (b) 3.26 nm C294H168 GQD (Top) and 5.54 nm C864H480 GQD (bottom) composed of seven and nineteen coronene domains, respectively. ....   | 87 |



## References

1. Ghaderi, S., Ramesh, B. & Seifalian, A.M. Synthesis of Mercaptosuccinic Acid/MercaptoPolyhedral Oligomeric Silsesquioxane Coated Cadmium Telluride Quantum Dots in Cell Labeling Applications. *Journal of Nanoscience and Nanotechnology* **12**, 4928-4935 (2012).
2. Geim, A.K. & Novoselov, K.S. The rise of graphene. *Nature Materials* **6**, 183-191 (2007).
3. Zhou, X., Guo, S. & Zhang, J. Solution-Processable Graphene Quantum Dots. *Chemical Physics Physical Chemistry*, **14**, 2627-2640 (2013).
4. Qu, D. et al. Highly luminescent S, N co-doped graphene quantum dots with broad visible absorption bands for visible light photocatalysts. *Nanoscale* **5**, 12272-12277 (2013).
5. Shen, J., Zhu, Y., Yang, X. & Li, C. Graphene quantum dots: emergent nanolights for bioimaging, sensors, catalysis and photovoltaic devices. *Chemical communications* **48**, 3686-3699 (2012).
6. Zhang, Z.P., Zhang, J., Chen, N. & Qu, L.T. Graphene quantum dots: an emerging material for energy-related applications and beyond. *Energ Environ Sci* **5**, 8869-8890 (2012).
7. Shen, J., Zhu, Y., Yang, X. & Li, C. Graphene quantum dots: emergent nanolights for bioimaging, sensors, catalysis and photovoltaic devices. *Chemical communications* **48**, 3686-3699 (2012).
8. Liu, R.L., Wu, D.Q., Feng, X.L. & Mullen, K. Bottom-Up Fabrication of Photoluminescent Graphene Quantum Dots with Uniform Morphology. *Journal of the American Chemical Society* **133**, 15221-15223 (2011).
9. Lu, J., Yeo, P.S.E., Gan, C.K., Wu, P. & Loh, K.P. Transforming C-60 molecules into graphene quantum dots. *Nature Nanotechnology* **6**, 247-252 (2011).
10. Li, L.L. et al. Focusing on luminescent graphene quantum dots: current status and future perspectives. *Nanoscale* **5**, 4015-4039 (2013).
11. Kim, S. et al. Anomalous Behaviors of Visible Luminescence from Graphene Quantum Dots: Interplay between Size and Shape. *ACS Nano* **6**, 8203-8208 (2012).
12. Zhu, S.J. et al. Strongly green-photoluminescent graphene quantum dots for bioimaging applications. *Chemical communications* **47**, 6858-6860 (2011).

13. Wu, X. et al. Fabrication of highly fluorescent graphene quantum dots using l-glutamic acid for in vitro/in vivo imaging and sensing. *Journal of Materials Chemistry C* **1**, 4676-4684 (2013).
14. Liu, Q., Guo, B., Rao, Z., Zhang, B. & Gong, J.R. Strong Two-Photon-Induced Fluorescence from Photostable, Biocompatible Nitrogen-Doped Graphene Quantum Dots for Cellular and Deep-Tissue Imaging. *Nano Letters* **13**, 2436-2441 (2013).
15. Lee, E., Ryu, J. & Jang, J. Fabrication of graphene quantum dots via size-selective precipitation and their application in upconversion-based DSSCs. *Chemical communications* **49**, 9995-9997 (2013).
16. Zhu, S.J. et al. Graphene quantum dots with controllable surface oxidation, tunable fluorescence and up-conversion emission. *Rsc Advances* **2**, 2717-2720 (2012).
17. Shen, J., Zhu, Y., Chen, C., Yang, X. & Li, C. Facile preparation and upconversion luminescence of graphene quantum dots. *Chemical communications* **47**, 2580-2582 (2011).
18. Wen, X., Yu, P., Toh, Y.-R., Ma, X. & Tang, J. On the upconversion fluorescence in carbon nanodots and graphene quantum dots. *Chemical communications* **50**, 4703-4706 (2014).
19. Li, L.L. et al. A Facile Microwave Avenue to Electrochemiluminescent Two-Color Graphene Quantum Dots. *Advanced Functional Materials* **22**, 2971-2979 (2012).
20. Lu, Q. et al. Electrochemiluminescence resonance energy transfer between graphene quantum dots and gold nanoparticles for DNA damage detection. *Analyst* **139**, 2404-2410 (2014).
21. Lu, J.J. et al. Electrochemiluminescence of blue-luminescent graphene quantum dots and its application in ultrasensitive aptasensor for adenosine triphosphate detection. *Biosensors & Bioelectronics* **47**, 271-277 (2013).
22. Zheng, L., Chi, Y., Dong, Y., Lin, J. & Wang, B. Electrochemiluminescence of Water-Soluble Carbon Nanocrystals Released Electrochemically from Graphite. *Journal of the American Chemical Society* **131**, 4564-4565 (2009).
23. Ambrosi, A., Chua, C.K., Bonanni, A. & Pumera, M. Electrochemistry of graphene and related materials. *Chemical reviews* **114**, 7150-7188 (2014).

24. Shinde, D.B. & Pillai, V.K. Electrochemical Resolution of Multiple Redox Events for Graphene Quantum Dots. *Angewandte Chemie International Edition* **52**, 2482-2485 (2013).
25. Zhang, Y. et al. Graphene quantum dots/gold electrode and its application in living cell H<sub>2</sub>O<sub>2</sub> detection. *Nanoscale* **5**, 1816-1819 (2013).
26. Sun, H., Gao, N., Dong, K., Ren, J. & Qu, X. Graphene Quantum Dots-Band-Aids Used for Wound Disinfection. *ACS Nano* **8**, 6202-6210 (2014).
27. Li, Q., Zhang, S., Dai, L. & Li, L.-s. Nitrogen-Doped Colloidal Graphene Quantum Dots and Their Size-Dependent Electrocatalytic Activity for the Oxygen Reduction Reaction. *Journal of the American Chemical Society* **134**, 18932-18935 (2012).
28. Li, Y. et al. Nitrogen-Doped Graphene Quantum Dots with Oxygen-Rich Functional Groups. *Journal of the American Chemical Society* **134**, 15-18 (2012).
29. Peng, J. et al. Graphene Quantum Dots Derived from Carbon Fibers. *Nano Letters* **12**, 844-849 (2012).
30. Zhang, M. et al. Facile synthesis of water-soluble, highly fluorescent graphene quantum dots as a robust biological label for stem cells. *J Mater Chem* **22**, 7461-7467 (2012).
31. Shang, W. et al. The uptake mechanism and biocompatibility of graphene quantum dots with human neural stem cells. *Nanoscale* **6**, 5799-5806 (2014).
32. Chong, Y. et al. The in vitro and in vivo toxicity of graphene quantum dots. *Biomaterials* **35**, 5041-5048 (2014).
33. Pan, D.Y., Zhang, J.C., Li, Z. & Wu, M.H. Hydrothermal Route for Cutting Graphene Sheets into Blue-Luminescent Graphene Quantum Dots. *Advanced Materials* **22**, 734-738 (2010).
34. Ye, R. et al. Coal as an abundant source of graphene quantum dots. *Nat Commun* **4** (2013).
35. Dong, Y.Q. et al. One-step and high yield simultaneous preparation of single- and multi-layer graphene quantum dots from CX-72 carbon black. *Journal of Material Chemistry* **22**, 8764-8766 (2012).
36. Pan, D.Y. et al. Cutting sp<sup>2</sup> clusters in graphene sheets into colloidal graphene quantum dots with strong green fluorescence. *Journal of Material Chemistry* **22**, 3314-3318 (2012).

37. Shen, J.H. et al. One-pot hydrothermal synthesis of graphene quantum dots surface-passivated by polyethylene glycol and their photoelectric conversion under near-infrared light. *New Journal of Chemistry* **36**, 97-101 (2012).
38. Zhao, H.X. et al. Highly selective detection of phosphate in very complicated matrixes with an off-on fluorescent probe of europium-adjusted carbon dots. *Chemical communications* **47**, 2604-2606 (2011).
39. Lin, L. & Zhang, S. Creating high yield water soluble luminescent graphene quantum dots via exfoliating and disintegrating carbon nanotubes and graphite flakes. *Chemical communications* **48**, 10177-10179 (2012).
40. Yang, F. et al. Influence of pH on the fluorescence properties of graphene quantum dots using ozonation pre-oxide hydrothermal synthesis. *Journal of Material Chemistry* **22**, 25471-25479 (2012).
41. Zhang, C.Z., Mahmood, N., Yin, H., Liu, F. & Hou, Y.L. Synthesis of Phosphorus-Doped Graphene and its Multifunctional Applications for Oxygen Reduction Reaction and Lithium Ion Batteries. *Advanced Materials* **25**, 4932-4937 (2013).
42. Lu, J. et al. One-Pot Synthesis of Fluorescent Carbon Nanoribbons, Nanoparticles, and Graphene by the Exfoliation of Graphite in Ionic Liquids. *ACS nano* **3**, 2367-2375 (2009).
43. Li, Y. et al. An Electrochemical Avenue to Green-Luminescent Graphene Quantum Dots as Potential Electron-Acceptors for Photovoltaics. *Advanced Materials* **23**, 776-780 (2011).
44. Zhuo, S.J., Shao, M.W. & Lee, S.T. Upconversion and Downconversion Fluorescent Graphene Quantum Dots: Ultrasonic Preparation and Photocatalysis. *ACS nano* **6**, 1059-1064 (2012).
45. Yan, X., Cui, X. & Li, L.-s. Synthesis of Large, Stable Colloidal Graphene Quantum Dots with Tunable Size. *Journal of the American Chemical Society* **132**, 5944-5945 (2010).
46. Hamilton, I.P., Li, B.S., Yan, X. & Li, L.S. Alignment of Colloidal Graphene Quantum Dots on Polar Surfaces. *Nano Letters* **11**, 1524-1529 (2011).
47. Li, L.S. & Yan, X. Colloidal Graphene Quantum Dots. *Journal of Physical Chemistry Letters* **1**, 2572-2576 (2010).
48. Mueller, M.L., Yan, X., McGuire, J.A. & Li, L.S. Triplet States and Electronic Relaxation in Photoexcited Graphene Quantum Dots. *Nano Letters* **10**, 2679-2682 (2010).

49. Yan, X., Cui, X., Li, B. & Li, L.-s. Large, Solution-Processable Graphene Quantum Dots as Light Absorbers for Photovoltaics. *Nano Letters* **10**, 1869-1873 (2010).
50. Mueller, M.L., Yan, X., Dragnea, B. & Li, L.-s. Slow Hot-Carrier Relaxation in Colloidal Graphene Quantum Dots. *Nano Letters* **11**, 56-60 (2010).
51. Yan, X. et al. Independent Tuning of the Band Gap and Redox Potential of Graphene Quantum Dots. *The Journal of Physical Chemistry Letters* **2**, 1119-1124 (2011).
52. Dong, Y.Q. et al. Blue luminescent graphene quantum dots and graphene oxide prepared by tuning the carbonization degree of citric acid. *Carbon* **50**, 4738-4743 (2012).
53. Wang, X. et al. Heteroatom-doped graphene materials: syntheses, properties and applications. *Chemical Society Reviews* **43**, 7067-7098 (2014).
54. Li, M. et al. Synthesis and upconversion luminescence of N-doped graphene quantum dots. *Applied Physics Letters* **101**, 103107 (2012).
55. Hu, C.F. et al. One-step preparation of nitrogen-doped graphene quantum dots from oxidized debris of graphene oxide. *Journal of Materials Chemistry B* **1**, 39-42 (2013).
56. Ju, J. & Chen, W. Synthesis of highly fluorescent nitrogen-doped graphene quantum dots for sensitive, label-free detection of Fe (III) in aqueous media. *Biosensors and Bioelectronics* **58**, 219-225 (2014).
57. Tang, L. et al. Deep Ultraviolet to Near-Infrared Emission and Photoresponse in Layered N-Doped Graphene Quantum Dots. *ACS nano* **8**, 6312-6320 (2014).
58. Fan, Z. et al. Surrounding media sensitive photoluminescence of boron-doped graphene quantum dots for highly fluorescent dyed crystals, chemical sensing and bioimaging. *Carbon* **70**, 149-156 (2014).
59. Dey, S., Govindaraj, A., Biswas, K. & Rao, C.N.R. Luminescence properties of boron and nitrogen doped graphene quantum dots prepared from arc-discharge-generated doped graphene samples. *Chemical Physics Letters* **595-596**, 203-208 (2014).
60. Dong, Y. et al. Carbon-Based Dots Co-doped with Nitrogen and Sulfur for High Quantum Yield and Excitation-Independent Emission. *Angewandte Chemie International Edition* **52**, 7800-7804 (2013).

61. Zhu, S.J. et al. Surface Chemistry Routes to Modulate the Photoluminescence of Graphene Quantum Dots: From Fluorescence Mechanism to Up-Conversion Bioimaging Applications. *Advanced Functional Materials* **22**, 4732-4740 (2012).
62. Sun, H.J., Wu, L., Gao, N., Ren, J.S. & Qu, X.G. Improvement of Photoluminescence of Graphene Quantum Dots with a Biocompatible Photochemical Reduction Pathway and Its Bioimaging Application. *Acs Applied Materials & Interfaces* **5**, 1174-1179 (2013).
63. Shen, J. et al. One-pot hydrothermal synthesis of graphene quantum dots surface-passivated by polyethylene glycol and their photoelectric conversion under near-infrared light. *New Journal of Chemistry* **36**, 97-101 (2012).
64. Abdullah Al, N. et al. Target Delivery and Cell Imaging Using Hyaluronic Acid-Functionalized Graphene Quantum Dots. *Molecular Pharmaceutics* **10**, 3736-3744 (2013).
65. Wang, Z. et al. Synthesis of strongly green-photoluminescent graphene quantum dots for drug carrier. *Colloids and Surfaces B: Biointerfaces* **112**, 192-196 (2013).
66. Yan, X., Li, B. & Li, L.-s. Colloidal Graphene Quantum Dots with Well-Defined Structures. *Accounts of Chemical Research* **46**, 2254-2262 (2013).
67. Tetsuka, H. et al. Optically Tunable Amino-Functionalized Graphene Quantum Dots. *Advanced Materials* **24**, 5333-5338 (2012).
68. Kumar, V. et al. Facile, rapid and upscaled synthesis of green luminescent functional graphene quantum dots for bioimaging. *Rsc Advances* **4**, 21101-21107 (2014).
69. Solanki, A., Kim, J.D. & Lee, K.-B. Nanotechnology for regenerative medicine: nanomaterials for stem cell imaging. *Nanomedicine* **3**, 567-578 (2008).
70. Zheng, X.T., Than, A., Ananthanaraya, A., Kim, D.-H. & Chen, P. Graphene Quantum Dots as Universal Fluorophores and Their Use in Revealing Regulated Trafficking of Insulin Receptors in Adipocytes. *ACS nano* **7**, 6278-6286 (2013).
71. Nurunnabi, M., Khatun, Z., Nafiujjaman, M., Lee, D.-g. & Lee, Y.-k. Surface Coating of Graphene Quantum Dots using Mussel Inspired Polydopamine for Biomedical Optical Imaging. *ACS Applied Materials & Interfaces* **5**, 8246-8253 (2013).
72. Ran, X., Sun, H.J., Pu, F., Ren, J.S. & Qu, X.G. Ag Nanoparticle-decorated graphene quantum dots for label-free, rapid and sensitive detection of Ag<sup>+</sup> and biothiols. *Chemical communications* **49**, 1079-1081 (2013).

73. Li, Y.-H., Zhang, L., Huang, J., Liang, R.-P. & Qiu, J.-D. Fluorescent graphene quantum dots with a boronic acid appended bipyridinium salt to sense monosaccharides in aqueous solution. *Chemical communications* **49**, 5180-5182 (2013).
74. Liu, J.J. et al. Glutathione-functionalized graphene quantum dots as selective fluorescent probes for phosphate-containing metabolites. *Nanoscale* **5**, 1810-1815 (2013).
75. Amjadi, M., Manzoori, J.L. & Hallaj, T. Chemiluminescence of graphene quantum dots and its application to the determination of uric acid. *Journal of Luminescence* **153**, 73-78 (2014).
76. Wang, Y., Zhang, L., Liang, R.-P., Bai, J.-M. & Qiu, J.-D. Using Graphene Quantum Dots as Photoluminescent Probes for Protein Kinase Sensing. *Analytical Chemistry* **85**, 9148-9155 (2013).
77. Qian, Z.S. et al. A universal fluorescence sensing strategy based on biocompatible graphene quantum dots and graphene oxide for the detection of DNA. *Nanoscale* **6**, 5671-5674 (2014).
78. Zhang, P. et al. Dual-Peak Electrogenerated Chemiluminescence of Carbon Dots for Iron Ions Detection. *Analytical Chemistry* **86**, 5620-5623 (2014).
79. Zhao, J., Chen, G.F., Zhu, L. & Li, G.X. Graphene quantum dots-based platform for the fabrication of electrochemical biosensors. *Electrochemistry Communications* **13**, 31-33 (2011).
80. Razmi, H. & Mohammad-Rezaei, R. Graphene quantum dots as a new substrate for immobilization and direct electrochemistry of glucose oxidase: Application to sensitive glucose determination. *Biosensors & Bioelectronics* **41**, 498-504 (2013).
81. Yeh, T.-F., Teng, C.-Y., Chen, S.-J. & Teng, H. Nitrogen-Doped Graphene Oxide Quantum Dots as Photocatalysts for Overall Water-Splitting under Visible Light Illumination. *Advanced Materials* **26**, 3297-3303 (2014).
82. Zhou, X. et al. Photo-Fenton Reaction of Graphene Oxide: A New Strategy to Prepare Graphene Quantum Dots for DNA Cleavage. *ACS nano* **6**, 6592-6599 (2012).
83. Liu, Z., Robinson, J.T., Sun, X.M. & Dai, H.J. PEGylated nanographene oxide for delivery of water-insoluble cancer drugs. *Journal of the American Chemical Society* **130**, 10876-10877 (2008).
84. Sun, X. et al. Nano-graphene oxide for cellular imaging and drug delivery. *Nano Research*. **1**, 203-212 (2008).

85. Wang, Z. et al. Synthesis of strongly green-photoluminescent graphene quantum dots for drug carrier. *Colloids and Surfaces B: Biointerfaces*.
86. Wang, Y. et al. Near resonant and nonresonant third-order optical nonlinearities of colloidal InP/ZnS quantum dots. *Applied Physics Letters* **102**, 021917 (2013).
87. Jing, Y.J., Zhu, Y.H., Yang, X.L., Shen, J.H. & Li, C.Z. Ultrasound-Triggered Smart Drug Release from Multifunctional Core-Shell Capsules One-Step Fabricated by Coaxial Electrospray Method. *Langmuir* **27**, 1175-1180 (2011).
88. Nie, H. et al. Carbon Dots with Continuously Tunable Full-Color Emission and Their Application in Ratiometric pH Sensing. *Chemistry of Materials* **26**, 3104-3112 (2014).
89. Chen, T. et al. Graphene Quantum Dots-Capped Mesoporous Silica Nanoparticles through an Acid-Cleavable Acetal Bond for Intracellular Drug Delivery and Imaging. *Journal of Materials Chemistry B* (2014).
90. Markovic, Z.M. et al. Graphene quantum dots as autophagy-inducing photodynamic agents. *Biomaterials* **33**, 7084-7092 (2012).
91. Zheng, B. et al. Electron Transfer from Graphene Quantum Dots to the Copper Complex Enhances Its Nuclease Activity. *The Journal of Physical Chemistry C* **118**, 7637-7642 (2014).
92. Sun, H., Gao, N., Dong, K., Ren, J. & Qu, X. Graphene Quantum Dots-Band-Aids Used for Wound Disinfection. *ACS nano* (2014).
93. Jiang, F. et al. Eco-friendly synthesis of size-controllable amine-functionalized graphene quantum dots with antimycoplasma properties. *Nanoscale* **5**, 1137-1142 (2013).
94. Dong, X.C. et al. 3D Graphene-Cobalt Oxide Electrode for High-Performance Supercapacitor and Enzymeless Glucose Detection. *Acs Nano* **6**, 3206-3213 (2012).
95. Lu, J. et al. One-Pot Synthesis of Fluorescent Carbon Nanoribbons, Nanoparticles, and Graphene by the Exfoliation of Graphite in Ionic Liquids. *ACS Nano* **3**, 2367-2375 (2009).
96. Grondin, J. et al. Revisited vibrational assignments of imidazolium-based ionic liquids. *Journal of Raman Spectroscopy* **42**, 733-743 (2011).
97. Yang, H. et al. Covalent functionalization of polydisperse chemically-converted graphene sheets with amine-terminated ionic liquid. *Chemical communications*, 3880-3882 (2009).



98. Jin, S.H., Kim, D.H., Jun, G.H., Hong, S.H. & Jeon, S. Tuning the Photoluminescence of Graphene Quantum Dots through the Charge Transfer Effect of Functional Groups. *Acs Nano* **7**, 1239-1245 (2013).
99. Peng, J. et al. Graphene Quantum Dots Derived from Carbon Fibers. *Nano Letters* **12**, 844-849 (2012).
100. Li, Y. et al. An electrochemical avenue to green-luminescent graphene quantum dots as potential electron-acceptors for photovoltaics. *Advanced materials* **23**, 776-780 (2011).
101. Li, Y. et al. Nitrogen-doped graphene quantum dots with oxygen-rich functional groups. *J Am Chem Soc* **134**, 15-18 (2012).
102. Bian, N., Chen, Q., Qiu, X.L., Qi, A.D. & Han, B.H. Imidazole-bearing tetraphenylethylene: fluorescent probe for metal ions based on AIE feature. *New Journal of Chemistry* **35**, 1667-1671 (2011).
103. Beard, J.L. Iron biology in immune function, muscle metabolism and neuronal functioning. *The Journal of nutrition* **131**, 568S-579S; discussion 580S (2001).
104. Pithadia, A.S. & Lim, M.H. Metal-associated amyloid- $\beta$  species in Alzheimer's disease. *Current Opinion in Chemical Biology* **16**, 67-73 (2012).
105. Bai, J.M., Zhang, L., Liang, R.P. & Qiu, J.D. Graphene quantum dots combined with europium ions as photoluminescent probes for phosphate sensing. *Chemistry* **19**, 3822-3826 (2013).
106. Xie, M.M. et al. Blue and green photoluminescence graphene quantum dots synthesized from carbon fibers. *Material Letters* **93**, 161-164 (2013).
107. Shinde, D.B. & Pillai, V.K. Electrochemical Preparation of Luminescent Graphene Quantum Dots from Multiwalled Carbon Nanotubes. *Chemistry an European Journal* **18**, 12522-12528 (2012).
108. Peng, J. et al. Graphene quantum dots derived from carbon fibers. *Nano Letters* **12**, 844-849 (2012).
109. Xie, W.J., Fu, Y.Y., Ma, H., Zhang, M. & Fan, L.Z. Preparation of Fluorescent Graphene Quantum Dots as Biological Imaging Marker for Cells. *Acta Chim Sinica* **70**, 2169-2172 (2012).
110. Zhang, L. et al. Preparation of graphene quantum dots for bioimaging application. *Journal of Nanoscience and Nanotechnology* **12**, 2924-2928 (2012).
111. Liu, Q., Guo, B., Rao, Z., Zhang, B. & Gong, J.R. Strong two-photon-induced fluorescence from photostable, biocompatible nitrogen-doped graphene quantum dots for cellular and deep-tissue imaging. *Nano letters* **13**, 2436-2441 (2013).

112. Zheng, X.T., Ananthanarayanan, A., Luo, K.Q. & Chen, P. Glowing Graphene Quantum Dots and Carbon Dots: Properties, Syntheses, and Biological Applications. *Small* **11**, 1620–1636 (2014).
113. Wang, X. et al. Heteroatom-doped graphene materials: syntheses, properties and applications. *Chemical Society Reviews* **43**, 7067-7098 (2014).
114. Sk, M.A., Ananthanarayanan, A., Huang, L., Lim, K.H. & Chen, P. Revealing the tunable photoluminescence properties of graphene quantum dots. *Journal of Materials Chemistry C* **2**, 6954-6960 (2014).
115. Palaniselvam, T., Valappil, M.O., Illathvalappil, R. & Kurungot, S. Nanoporous graphene by quantum dots removal from graphene and its conversion to a potential oxygen reduction electrocatalyst via nitrogen doping. *Energy and Environment Science* **7**, 1059-1067 (2014).
116. Qu, D. et al. Formation mechanism and optimization of highly luminescent N-doped graphene quantum dots. *Scientific Reports* **4** (2014).
117. Lin, L. et al. A facile synthesis of highly luminescent nitrogen-doped graphene quantum dots for the detection of 2,4,6-trinitrophenol in aqueous solution. *Nanoscale* **7**, 1872-1878 (2015).
118. Wang, Y. et al. Stimulated Emission and Lasing from CdSe/CdS/ZnS Core-Multi-Shell Quantum Dots by Simultaneous Three-Photon Absorption. *Advanced Materials* **26**, 2954-2961 (2014).
119. Wang, Y. et al. Blue Liquid Lasers from Solution of CdZnS/ZnS Ternary Alloy Quantum Dots with Quasi-Continuous Pumping. *Advanced Materials* **27**, 169-175 (2015).
120. Wang, H., Maiyalagan, T. & Wang, X. Review on Recent Progress in Nitrogen-Doped Graphene: Synthesis, Characterization, and Its Potential Applications. *ACS Catalysis* **2**, 781-794 (2012).
121. Jeon, I.-Y. et al. Large-Scale Production of Edge-Selectively Functionalized Graphene Nanoplatelets via Ball Milling and Their Use as Metal-Free Electrocatalysts for Oxygen Reduction Reaction. *Journal of the American Chemical Society* **135**, 1386-1393 (2012).
122. Qu, L.T., Liu, Y., Baek, J.B. & Dai, L.M. Nitrogen-Doped Graphene as Efficient Metal-Free Electrocatalyst for Oxygen Reduction in Fuel Cells. *Acs Nano* **4**, 1321-1326 (2010).

123. Lu, Z.J. et al. Nitrogen-doped reduced-graphene oxide as an efficient metal-free electrocatalyst for oxygen reduction in fuel cells. *Rsc Advances* **3**, 3990-3995 (2013).
124. Sheng, Z.H. et al. Catalyst-Free Synthesis of Nitrogen-Doped Graphene via Thermal Annealing Graphite Oxide with Melamine and Its Excellent Electrocatalysis. *Acs Nano* **5**, 4350-4358 (2011).
125. Liao, S.H. et al. One-Step Reduction and Functionalization of Graphene Oxide with Phosphorus-Based Compound to Produce Flame-Retardant Epoxy Nanocomposite. *Industrial Engineering Chemical Research* **51**, 4573-4581 (2012).
126. Li, M. et al. Synthesis and upconversion luminescence of N-doped graphene quantum dots. *Applied Physics Letters* **101**, 103107 (2012).
127. Jabeen, H. et al. Enhanced Cr(VI) removal using iron nanoparticle decorated graphene. *Nanoscale* **3**, 3583-3585 (2011).
128. Luo, Z. et al. Pyridinic N doped graphene: synthesis, electronic structure, and electrocatalytic property. *Journal of Material Chemistry* **21**, 8038-8044 (2011).
129. Hart, J.N. et al. Towards new binary compounds: Synthesis of amorphous phosphorus carbide by pulsed laser deposition. *Journal of Solid State Chemistry* **198**, 466-474 (2013).
130. Prasad, K.S., Pallela, R., Kim, D.M. & Shim, Y.B. Microwave-Assisted One-Pot Synthesis of Metal-Free Nitrogen and Phosphorus Dual-Doped Nanocarbon for Electrocatalysis and Cell Imaging. *Particle & Particle Systems Characterization* **30**, 557-564 (2013).
131. Wang, H.-m. et al. Phosphorus-doped graphene and (8, 0) carbon nanotube: Structural, electronic, magnetic properties, and chemical reactivity. *Applied Surface Science* **273**, 302-309 (2013).
132. Wu, X. et al. Fabrication of highly fluorescent graphene quantum dots using L-glutamic acid for in vitro/in vivo imaging and sensing. *Journal of materials chemistry. C, Materials for optical and electronic devices* **1**, 4676-4684 (2013).
133. Schiros, T. et al. Connecting Dopant Bond Type with Electronic Structure in N-Doped Graphene. *Nano Letters* **12**, 4025-4031 (2012).
134. Gillaizeau-Gauthier, I. et al. Phosphonate-Based Bipyridine Dyes for Stable Photovoltaic Devices. *Inorganic Chemistry* **40**, 6073-6079 (2001).

135. Zhu, S. et al. Surface Chemistry Routes to Modulate the Photoluminescence of Graphene Quantum Dots: From Fluorescence Mechanism to Up-Conversion Bioimaging Applications. *Advanced Functional Materials* **22**, 4732-4740 (2012).
136. He, G.S., Tan, L.-S., Zheng, Q. & Prasad, P.N. Multiphoton Absorbing Materials: Molecular Designs, Characterizations, and Applications. *Chemical reviews* **108**, 1245-1330 (2008).
137. Zipfel, W.R., Williams, R.M. & Webb, W.W. Nonlinear magic: multiphoton microscopy in the biosciences. *Nature Biotechnology* **21**, 1369-1257 (2003).
138. Pu, S.-C. et al. The Empirical Correlation Between Size and Two-Photon Absorption Cross Section of CdSe and CdTe Quantum Dots. *Small* **2**, 1308-1313 (2006).
139. Lee, W.-H., Cho, M., Jeon, S.-J. & Cho, B.R. Two-Photon Absorption and Second Hyperpolarizability of the Linear Quadrupolar Molecule. *The Journal of Physical Chemistry A* **104**, 11033-11040 (2000).
140. Zhou, Z.-J., Liu, Z.-B., Li, Z.-R., Huang, X.-R. & Sun, C.-C. Shape Effect of Graphene Quantum Dots on Enhancing Second-Order Nonlinear Optical Response and Spin Multiplicity in NH<sub>2</sub>-GQD-NO<sub>2</sub> Systems. *The Journal of Physical Chemistry C* **115**, 16282-16286 (2011).
141. Nagabhushana, A. et al. Regulation of endocytic trafficking of transferrin receptor by optineurin and its impairment by a glaucoma-associated mutant. *BMC cell biology* **11**, 4 (2010).
142. Yang, X. et al. Multi-functionalized graphene oxide based anticancer drug-carrier with dual-targeting function and pH-sensitivity. *Journal of Material Chemistry* **21**, 3448-3454 (2011).
143. Wang, X.-y. et al. The permeability and transport mechanism of graphene quantum dots (GQDs) across the biological barrier. *Nanoscale* **7**, 2034-2041 (2015).
144. Yuan, X. et al. Cellular distribution and cytotoxicity of graphene quantum dots with different functional groups. *Nanoscale Research Letters* **9**, 1-9 (2014).
145. Wang, X. et al. Multifunctional graphene quantum dots for simultaneous targeted cellular imaging and drug delivery. *Colloids and Surfaces B: Biointerfaces* **122**, 638-644 (2014).
146. Jeon, I.-Y. et al. Edge-Selectively Sulfurized Graphene Nanoplatelets as Efficient Metal-Free Electrocatalysts for Oxygen Reduction Reaction: The Electron Spin Effect. *Advanced Materials* **25**, 6138-6145 (2013).

147. Jeon, I.-Y. et al. Direct nitrogen fixation at the edges of graphene nanoplatelets as efficient electrocatalysts for energy conversion. *Scientific Reports* **3**, (2013).
148. Jeon, I.-Y. et al. Edge-carboxylated graphene nanosheets via ball milling. *Proceedings of the National Academy of Sciences* **109**, 5588-5593 (2012).
149. Fan, L. et al. Fluorescence resonance energy transfer quenching at the surface of graphene quantum dots for ultrasensitive detection of TNT. *Talanta* **101**, 192-197 (2012).
150. Ofori-Kwakye, K. & Fell, J.T. Biphasic drug release: the permeability of films containing pectin, chitosan and HPMC. *International Journal of Pharmaceutics* **226**, 139-145 (2001).
151. Li, L. et al. Focusing on luminescent graphene quantum dots: current status and future perspectives. *Nanoscale* **5**, 4015-4039 (2013).
152. Liu, R., Wu, D., Feng, X. & Mullen, K. Bottom-Up Fabrication of Photoluminescent Graphene Quantum Dots with Uniform Morphology. *Journal of the American Chemical Society* **133**, 15221-15223 (2011).
153. Dong, Y. et al. One-step and high yield simultaneous preparation of single- and multi-layer graphene quantum dots from CX-72 carbon black. *Journal of Material Chemistry* **22**, 8764-8766 (2012).
154. Ananthanarayanan, A. et al. Facile Synthesis of Graphene Quantum Dots from 3D Graphene and their Application for Fe<sup>3+</sup> Sensing. *Adv. Funct. Mater.* **24**, 3021-3026 (2014).
155. Frisch, M.J. et al. *Gaussian 09, Revision B.01*, Gaussian, Inc., Wallingford CT, 2010.
156. Koch, W. & Holthausen, M.C. A Chemist's Guide to Density Functional Theory. (Wiley-VCH, 2000).
157. Parr, R.G. & Yang, W. Density-Functional Theory of Atoms and Molecules. (Oxford University Press, New York; 1989).
158. Becke, A.D. Density-functional thermochemistry. III. The role of exact exchange. *J. Chem. Phys.* **98**, 5648-5652 (1993).
159. Lee, C., Yang, W. & Parr, R.G. Development of the Colle-Salvetti correlation-energy formula into a functional of the electron density. *Phys. Rev. B* **37**, 785-789 (1988).
160. Schwarz, F.P. & Wasik, S.P. Fluorescence Measurements of Benzene, Naphthalene, Anthracene, Pyrene, Fluoranthene, and Benzo[e]pyrene in Water. *Analytical Chemistry* **48**, 524-528 (1976).

161. Waris, R., Rembert, M.A., Sellers, D.M., William E. Acree, J. & Kenneth W. Street, J. Polycyclic Aromatic Hydrocarbon Solute Probes Part II.\* Effect of Solvent Polarity on the Fluorescence Emission Fine Structures of Coronene Derivatives. *Analyst* **114**, 195-199 (1989).
162. Tucker, S.A., William E. Acree, J., Kenneth W. Street, J. & Fetzer, J.C. Polycyclic Aromatic Hydrocarbon Solute Probes. Part III: Fluorescence Emission Spectra of Pyrene, Ovalene, Benzo[ghi]perylene, and Coronene Dissolved in Liquid Tetrabutylammonium Sulfonate Salts. *Applied Spectroscopy* **43**, 162-164 (1989).
163. Zhang, L. et al. Origin of Visible Photoluminescence of ZnO Quantum Dots: Defect-Dependent and Size-Dependent. *J. Phys. Chem. C* **114**, 9651-9658 (2010).
164. Cheng, H.-M., Lin, K.-F., Hsu, H.-C. & Hsieh, W.-F. Size dependence of photoluminescence and resonant Raman scattering from ZnO quantum dots. *Applied Physics Letters* **88**, 261909 (2006).
165. Bailey, R.E. & Nie, S. Alloyed Semiconductor Quantum Dots: Tuning the Optical Properties without Changing the Particle Size. *Journal of the American Chemical Society* **125**, 7100-7106 (2003).
166. Efros, A.L. et al. Band-edge exciton in quantum dots of semiconductors with a degenerate valence band: Dark and bright exciton states. *Physical Reviews B* **54**, 4843-4856 (1996).
167. Pedrueza, E. et al. The effect of quantum size confinement on the optical properties of PbSe nanocrystals as a function of temperature and hydrostatic pressure. *Nanotech* **24**, 205701 (2013).
168. Ritter, K.A. & Lyding, J. The influence of edge structure on the electronic properties of graphene quantum dots and nanoribbons. *Nature Materials* **8**, 235-242 (2009).
169. Nakada, K., Fujita, M., Dresselhaus, G. & Dresselhaus, M.S. Edge state in graphene ribbons: Nanometer size effect and edge shape dependence. *Physical Review B* **54**, 17954-17961 (1996).
170. Zheng, X.T., Than, A., Ananthanaraya, A., Kim, D.-H. & Chen, P. Graphene quantum dots as universal fluorophores and their use in revealing regulated trafficking of insulin receptors in adipocytes. *ACS Nano* **7**, 6278-6286 (2013).
171. Loh, K.P., Bao, Q., Eda, G. & Chhowalla, M. Graphene oxide as a chemically tunable platform for optical applications. *Nature Chemistry* **2**, 1015-1024 (2010).

172. Chien, C.-T. et al. Tunable Photoluminescence from Graphene Oxide. *Angewandte Chemistry International Edition* **51**, 6662-6666 (2012).
173. Eda, G. et al. Blue photoluminescence from chemically derived graphene oxide. *Advanced Materials* **22**, 505-509 (2010).
174. Bassem El Hamaoui, Laquai, F.e.e., Balushev, S., Wu, J. & Müllen, K. A phosphorescent hexa-peri-hexabenzocoronene platinum complex and its time-resolved spectroscopy. *Synthetic Metals* **156**, 1182-1186 (2006).
175. Gokus, T. et al. Making Graphene Luminescent by Oxygen Plasma Treatment. *ACS Nano* **3**, 3963-3968 (2009).
176. Gupta, V. et al. Luminescent Graphene Quantum Dots for Organic Photovoltaic Devices. *Journal of the American Chemical Society* **133**, 9960-9963 (2011).
177. Shen, J., Zhu, Y., Chen, C., Yang, X. & Li, C. Facile preparation and upconversion luminescence of graphene quantum dots. *Chemical Communications* **47**, 2580-2582 (2011).
178. Li, Y. et al. An Electrochemical Avenue to Green-Luminescent Graphene Quantum Dots as Potential Electron-Acceptors for Photovoltaics. *Advanced Materials* **23**, 776-780 (2011).